Measurement of Particulate Emissions from Gasoline Direct Injection Engines

Submitted by

Longfei Chen

St Cross College

Department of Engineering Science
University of Oxford

A thesis submitted in partial fulfilment of the requirements for the degree of Doctor of Philosophy

Department of Engineering Science
University of Oxford
2010

Measurement of Particulate Emissions from Gasoline Direct Injection Engines

Longfei Chen
St Cross College, Oxford

Doctor of Philosophy
Department of Engineering Science

A thesis submitted in partial fulfilment of the requirements for the degree of Doctor of Philosophy at the University of Oxford, Trinity Term 2010

ABSTRACT

Gasoline Direct Injection (GDI) engines have been considered to be the key enabler for reducing the CO_2 emission from gasoline-powered vehicles. Compared to Port Fuel Injection (PFI) engines, GDI engines realize a higher compression ratio, a lower intake temperature and the absence of throttling which will deliver higher volumetric efficiency and lower fuel consumption. However, due to the reduced time for fuel atomization and the possibility of fuel impingement, GDI engines will inherently generate more Particulate Matter (PM) emissions than PFI engines. Previous research demonstrated that GDI engines typically emit one order of magnitude more PM than PFIs. Therefore, the number-based measurement of PM emissions from GDI engines is essential, for engine researchers and manufacturers to meet the number-based PM regulations in the near future.

This thesis undertakes to investigate: a) the effects of the after-treatment (Three-Way Catalyst) and various engine operational parameters, such as injection and ignition timing, injection strategy and valve timing on the PM emissions; b) the characteristics of GDI PM emissions using a range of gasoline/ethanol blends; c) The compositional information for GDI-generated PM emissions, i.e. the PM mass fractions in different volatility ranges. The first objective was achieved by using a Cambustion Ltd Differential Mobility Spectrometer 500 (DMS500) to simultaneously derive the PM size-resolved number concentrations and mass concentrations in the range of 5-1000 nm. The second objective was addressed by using the DMS500 together with other instruments such as a Photron

high-speed camera, a Cambustion Ltd fast Flame Ionization Detector (FID). The third objective was realized by using Thermo-Gravimetric Analysis (TGA). These experiments are amongst the first of their kind and may well provide vehicle manufacturers and the fuel industry with useful data for PM control and abatement.

Data acquisition (DAQ) systems for two test engines, namely, a V8 GDI engine and a single-cylinder optical access engine, have been developed in LabVIEW to facilitate recording various experimental data at different sampling rates (1Hz to 300 kHz). The DAQ system in the single-cylinder engine is also capable for communicating with the engine controlling system to enable automatic data logging. A controlled automatic dilution system has been developed for taking filter samples in a way that is consistent with emissions legislation.

CONTENTS

ACKNOWLEDGMENTS

I would like to express my sincere gratitude to my supervisor Professor Richard Stone for offering me the D.Phil. post, without which my research would not have been possible. I am also in debt to Professor Stone for his professional technical advice, strategic direction and patience in reading and correcting my thesis. His kindness and generous support has always eased my discomfort and unease, which is also crucial to the completion of this project.

I want to send my special appreciation for the Dorothy Hodgkin Postgraduate Awards (DHPA) and their financial support for my D.Phil. study and Jaguar Land Rover for contributing to laboratory expenses. Dave Richardson from Jaguar cars is gratefully acknowledged for his guidance and inspiration throughout the project. Thanks also to Roger Cracknell of Shell for the provision of the fuels.

Over the course of my doctorate I have made many friends, in particular in the Internal Combustion Engine Group (Ben Twiney, Mike Braisher, Martin Davy, Xiaowei Wang, Huayong Zhao, Fan Xu, Mengchen Hu and Ben Williams). It is their help and friendship that keeps my sanity and makes my life comfortable. I would also like to thank all the staff in the Electronic and Mechanical Workshops who have ever helped me build up test facilities.

Last but most importantly I would like to express my gratitude to my parents and my former supervisors Professor Jianxin Wang and Professor Shijin Shuai at Tsinghua University for their long-term consistent support and encouragement toward my research. Had it not been their help, I would not make progress this far.

Nomenclature

S.I. units and standard notations for chemical elements, formulae, and abbreviations are used in this thesis. Other abbreviations are listed below.

Acronyms

aBDC	After Bottom Dead Centre
ACH	Analogue CHannel
ADC	Analogue-to-Digital Converter
AFR	Air Fuel Ratio
AI	Analogue Input
AIGND	Analogue Input GrouND
AISENSE	Analogue Input SENSE
ASTM	American Society of Testing and Materials
AO	Analogue Output
aTDC	After Top Dead Centre
BF	Blank Filter
BMEP	Brake Mean Effective Pressure
BNC	Bayonet Neill-Concelman Connector
BSFC	Break Specific Fuel Consumption
bTDC	Before Top Dead Centre
C	Carbon
CA	Crank Angle
CAD	Crank Angle Degree
CAI	Controlled Auto Ignition
CCD	Charge-Coupled Device
CF	Charged Filter
CFD	Computational Fluid Dynamics
CI	Compression Ignition
CMD	Count (number) Mean Diameter
CO	Carbon Monoxide
CoBRA	Combustion Burn Rate Analysis
CoV	Coefficient of Variance
CPC	Condensation Particle Counter
CPMA	Centrifugal Particle Mass Analyser
CPS	Cam Profile Switching
CTA	Cam Torque Actuated
DAQ	Data Acquisition
DI	Direct Injection
DIFF	Differential (input)
DIO	Digital Output
DISI	Direct Injection Spark Ignition
DMS	Differential Mobility Spectrometer
DPF	Diesel Particle Filter
DR	Dilution Ratio
ECU	Engine Control Unit

EGR	Exhaust Gas Recirculation
ELPI	Electrical Low Pressure Impactor
EM	Electron Microscopy
ETCS	Engine Timing Control System
EVC	Exhaust Valve Closing
EVO	Exhaust Valve Opening
fFID	Fast Flame Ionization Detector
FIFO	First-In-First-Out (Buffer)
GCMS	Gas Chromatography and Mass Spectrometry
GDI	Gasoline Direct Injection
GFA	Grade GFA glass microfiber filter
GFC	Grade GFC glass microfiber filter
GSD	Geometric Standard Deviation
HC	Hydrocarbon
HCCI	Homogeneous Charge Compression Ignition
HEPA	High Efficiency Particulate Air (filter)
HT	High Tension
IIR	Infinite Impulse Response
IMEP	Indicated Mean Effective Pressure
IVC	Intake Valve Closing
IVO	Intake Valve Opening
LabVIEW	Laboratory Virtual Instrument Engineering Workbench
LED	Light-Emitting Diode
MAP	Manifold Absolute Pressure
MATLAB	Matrix Laboratory
MBT	Minimum ignition advance for Best Torque
MFB	Mass Fraction Burned
MFM	Mass Flow Meter
MFR	Mass Fraction of Residuals
MOP	Maximum Open Position
MUX	Multiplexer
NEDC	New European Drive Cycle
NI	National Instruments™
NMEP	Net Indicated Mean Effective Pressure
NO	Nitric Oxide
NO_2	Nitrogen Dioxide
NO_x	Mixture of Nitric Oxide and Nitrogen Dioxide
NRSE	Non-Referenced Single-Ended
NVO	Negative Valve Overlap
OEM	Original Equipment Manufacturer
PAH	Polycyclic Aromatic Hydrocarbon
PASS	Photo Acoustic Soot Sensor
PDF	Probability Density Function
PFI	Port Fuel Injection
PGA	Programmable-Gain Amplifier
PGIA	Programmable Gain Instrumentation Amplifier
PID	Proportional-Integral-Derivative
PM	Particulate Matter
PMP	Particle Measurement Program

Pm	Particle mass
Pn	Particle number
PURA	Shell PURA (gasoline)
RH	Relative Humidity
RON	Research Octane Number
RPM	Revolutions Per Minute
RSE	Reference Single-Ended
RVP	Reid Vapour Pressure
SEM	Scanning Electron Microscopy
SGDI	Spray Guided Direct Injection
SI	Spark Ignition
SMPS	Scanning Mobility Particle Sizer
SOI	Start of (fuel) Injection
SOF	Soluble Organic Fraction
SSP	Sampling Spark Plug
TAGS	Thermal Analysis Gas Station
TBD	To Be Determined
TDC	Top Dead Centre
TEM	Transmission Electron Microscopy
TGA	Thermo-Gravimetric Analysis
THC	Total Hydrocarbon
TTL	Transistor-Transistor Logic
TWC	Three Way Catalyst
ULG	Unleaded Gasoline
VCT	Variable Cam Timing
VDAQ	Very High Data Acquistion
VI	Virtual Instruments
VOF	Volatile Organic Fraction
VPR	Volatile Particle Remover
VVT	Variable Valve Timing
WF	Water Fraction
WOT	Wide Open Throttle

Symbols

A	DMS500 transfer function matrix
A_{pipe}	Inner area of the sampling pipe of the dilution system (m^2)
D_{p}	Particle size (nm)
e	DMS500 error term
i	Measured DMS500 electrometer ring current vector
j	Set of DMS500 electrometer current$I(\mu, \sigma_{\mathrm{g}})$ A lognormal function of the DMS500 spectrum; where μ is CMD, σ_g is GSD
K_{c}	PID controller gain
$\dot{m}_{\mathrm{air}}$	Mass flow rate of air ($g\ s^{-1}$)
$\dot{m}_{\mathrm{dil}}$	Mass flow rate of diluted gas ($g\ s^{-1}$)
$\dot{m}_{\mathrm{DMS}}$	Mass flow rate of post-VPR aerosol caused by the DMS500 ($g\ s^{-1}$)
$\dot{m}_{\mathrm{DIL}}$	Mass flow rate of post-VPR aerosol caused by the dilution system ($g\ s^{-1}$)

$\dot{m}_{\mathrm{exh}}$	Mass flow rate of exhaust gas (g s^{-1})
M_{exh}	Molar mass of exhaust gas (kg $kmol^{-1}$)
mu	Mean value
p_{dil}	Pressure of diluted gas (Pa)
P(D|w)	Probability of the measured DMS500 electrometer currents given a set of parameters D
PV	Process variable
P(w|D)	Posterior probability of the DMS500
ρ_{dil}	Density of diluted gas (kg/m^3)
R_{air}	Specific gas constant of air ($Jkg^{-1}K^{-1}$)
R_{exh}	Specific gas constant of exhaust gas ($Jkg^{-1}K^{-1}$)
s	Discrete or non-lognormal spectrum vector
S_1	Area of a whole filter (m^2)
S_2	PM-laden area of a filter (m^2)
S_3	Area of PM-laden filter piece for TGA test (m^2)
$sigma$	Standard deviation
SP	Set point
T_{d}	Derivative time of a PID controller (min)
T_{exh}	Temperature of exhaust gas (ºC)
T_{i}	Integral time of a PID controller (min)
T_{pre}	Temperature of Pre-VPR aerosol (ºC)
T_{post}	Temperature of Post-VPR aerosol (ºC)
t_{vpr}	Residence time in the VPR (s)
u_{D}	Derivative component of a PID controller
u_{I}	Proportional component of a PID controller
u_{P}	Proportional component of a PID controller
$\dot{V}_{\mathrm{dil}}$	Volumetric flow rate of diluted gas (m^3/s)
V_{filter}	Filter face velocity (m/s)
V_{vpr}	Volume of the VPR (L)
$\dot{V}_{\mathrm{vpr}}$	Volumetric flow rate in the VPR (m^3/s)
w	Lognormal parameters of nucleation or accumulation mode PM

Greek letters

Δ	Difference
λ	Relative air fuel ratio
η	Dynamic viscosity
θ	Crank angle
μ	Count (number) Mean Diameter
σ_g	Geometric standard deviation
ν	Kinematic viscosity
ρ	Density

LIST OF FIGURES

LIST OF TABLES

1. Background

1.1 Introduction

Gasoline Direct Injection (GDI) engines have gained a surge of interest in the last decade or so because of the improvement in fuel injection systems. As one way to combine the positive aspects from both Spark Ignition (SI) engines and Compression Ignition (CI) engines, GDI engines have been seen as a promising option in the vehicle industry for increasing the power output and reducing the specific fuel consumption. This thesis is concerned with studying the characteristics of Particulate Matter (PM) emissions from these engines.

Particulate emissions from vehicles is now stringently regulated in most countries, and the mass of particulate emitted from both light-duty and heavy-duty vehicles has decreased by more than two orders of magnitude since 1970, when the first particulate regulation was issued in the USA (Eastwood, 2007). Today's regulations are exclusively based upon total particle mass. However, much research has suggested that number-based particulate regulations be issued in the light of evidence that nano-particles, despite their negligible contribution to total mass, may also impose a great hazard to both the environment and human beings. Compared to DPF-equipped (Diesel Particle Filter) diesels, a bigger contribution to airborne nano-particle emissions emitted by gasoline engines especially GDI engines has been recognized. Therefore, the number-based PM regulations will be enforced in the near future and they are likely to apply to all types of vehicles, regardless of whether they burn diesel or gasoline.

However, measuring the number of particles is far more complicated than measuring the mass, since particles may be involved in mechanisms such as deposition, mutation, particle-to-gas conversion and thermophoresis during the exhaust process, which could then lead to a dramatic change in their total number. Various number-based particulate measurement instruments are commercially available as research tools. A Cambustion Ltd Differential Mobility Spectrometer 500 (DMS500) has been used for the majority of the experimental tests. Previous research showed that the DMS500 exhibits good agreement with the other more established instruments such as the Scanning Mobility Particle Sizer (SMPS) and the Electrical Low Pressure Impactor (ELPI), meanwhile, it features a faster time response and finer resolution in particle size (Price, 2009). The GDI engine-out PM emissions normally exhibit bi-lognormal distribution characteristics on number spectra with number concentrations ranging from 10^5 to 10^8 particles/cm^3.

Apart from the PM measurement, the temporal behaviour of fuel spray development and the in-cylinder pre-flame mixture homogeneity have been investigated in-depth in order to find out the causes for the difference in PM emissions when engine operational parameters or fuel composition are changed. It is also desirable to resolve the composition and the morphology of the particulate emissions, which could enable researchers to model the formation of particulate matter and to understand the impact on health.

The motion of a GDI engine piston connected to a crank through a connecting rod can be illustrated by Fig. 1.1, which includes mathematical equations for the crankshaft geometry.

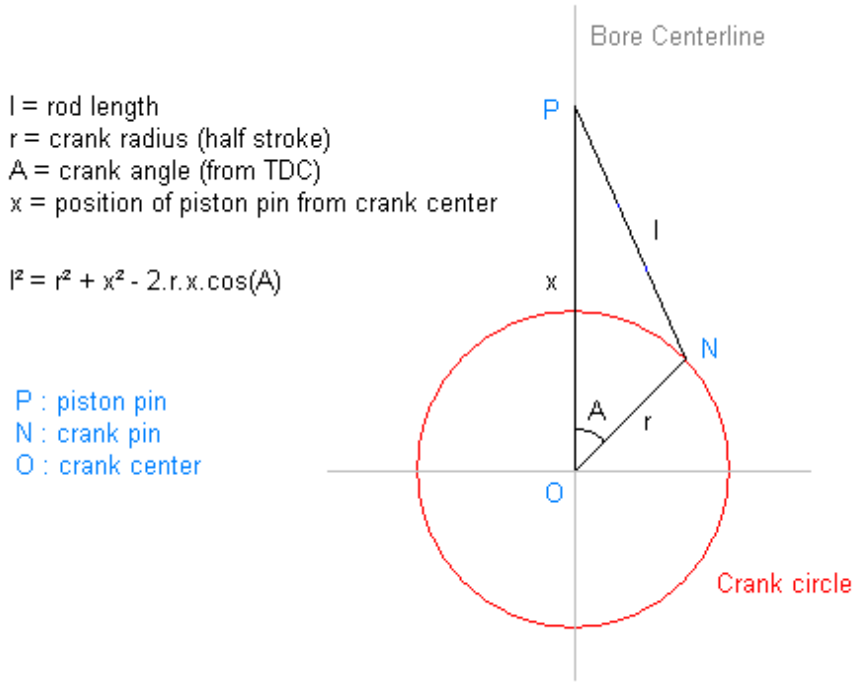

Fig. 1.1 Crankshaft geometry (http://en.wikipedia.org)

The rod length is the distance between piston pin and crank pin and the crank radius is the distance between crank pin and crank center, i.e. half stroke. Crank Angle Degree (CAD) is a unit used to measure the piston position with respect to a specific position e.g. the intake Top Dead Center (TDC). When the piston is at its highest point, known as the TDC, the crank angle is 0 CAD after TDC (aTDC).

This introductory chapter is followed by chapter 2, which describes the experimental arrangements, including test engines and their periphery facilities and the DAQ systems, together with a brief introduction to data processing. Chapter 3 details the development and application of an automatic dilution system which was used for collecting particles on glass fibre filters for further characterizing PM properties, such

as composition information and morphology. Chapters 4 and 5 are accounts of how engine operational parameters (such as injection and ignition timing, coolant temperature and valve timing) affect the PM emissions. Chapter 6 will explore the effects of ethanol blends on PM emissions, spray vaporization behaviour and mixture homogeneity. Chapter 7 summarizes the results from all the tests conducted in this work and puts forwards a number of suggestions for future work.

1.2 Legislation Review

1.2.1 PM-related Legislation

The particulate emission control era began in the early 1970s. Smoke from heavy-duty diesels was first legislated as opacity in the USA. Despite the complication of the development of particulate-control legislation, the first particulate standards in the world were established in 1980 and related to passenger cars and light-duty trucks; heavy-duty engines and trucks were subsequently covered in 1985. In Europe, particulate emissions from engines were first controlled in 1989, via EC Directives 88/436, 91/441 and 91/542 (Hall *et al.*, 1998).

Particulate matter (PM) is now strictly regulated in most countries, and the mass emitted by both light-duty (g/km) and heavy-duty (g/kWh) diesels has decreased since the 1970s by more than two orders of magnitude. According to Regulation (EC) No 715/2007, the new emission limit values will be enforced as shown in Table 1.1.

Table 1.1 EU light duty tailpipe emissions requirements for gasoline passenger cars (Official Journal of the European Union, 2007)

Effective timing	CO (mg/km)	THC (mg/km)	NO_x (mg/km)	PM (mg/km)	PN (1/km)
EU3: 01/2000	2.3	200	150	n/a	n/a
EU4: 01/2005	1.0	100	80	n/a	n/a
EU5: 09/2009	1.0	100	60	5.0	n/a
EU6: 09/2014	1.0	100	60	5.0	TBD

Current particulate air quality regulations and diesel PM regulations from the US Environmental Protection Agency (EPA) and the EU are typically based on a gravimetric method. However, it is well documented that gravimetric filter measurements can be affected by a variety of artefacts (Symonds *et al.*, 2007). These artefacts include adsorption of vapour onto the filter, volatilization of semi-volatile compounds from filtered particles, and an array of chemical reactions between filtered particles, the gas, and filter substrate (Hinds, 1999; Patashnick *et al.*, 2001). Another problem with filter measurements is that long sampling times are required for adequate measurement resolution and as future emission standards tighten, filter methods may not be feasible for such small amounts of accumulated mass (Symonds *et al*., 2007).

Compared with particulate mass, the number concentration may pose a greater threat to human health and the environment in the light of the results of previous researches on the impact of particulates. Based on Stokes' law, the rate at which particles settle increases with the square of their diameter, hence the rate at which fine particles settle is fairly low and they usually remain airborne for days (Hinds, 1999). In addition, they can easily pass through the human respiratory filtering system and deposit deep in the lungs. The ultrafine particles (< 100 nm in mean diameter) and the nano-sized particles (< 50 nm diameter) are considered to be potentially dangerous due to their

capability to enter deep into the respiratory tract (Luders *et al.*, 1998), which is consistent with what Kittelson (1998) has found in his research shown in Fig. 1.2.

The figure originally located here has been removed from this version of the thesis for copyright reasons.

Fig. 1.2 Engine particle size distributions and lung deposition efficiency (Kittelson, 1998)

Table 1.1 shows that the PM limit only applies to vehicles powered by DI (direct injection) gasoline engines. Although the PN limit for EU6 has not been determined for gasoline vehicles, the intention that particle number will be regulated in the future is clear.

1.2.2 Bio-fuel Legislation

The EU transport sector is primarily dependent on fossil fuels, with the crude oil feedstock being largely imported and thus extremely vulnerable to any market disturbance. The European Union promotes bio-fuel use proactively by defining ambitious targets of 5.75% by 2010 and 10% by 2020.

Ethanol, as one of the more promising gasoline additives (due to its octane enhancement effect), has been widely used around the world with strong government involvement. For instance, Portland became the first city in the United States to require all gasoline sold within the city limits to contain at least 10% ethanol in 2007 (http://postcarboncities.net/node/192); all unleaded gasoline (ULG) sold in New Zealand will contain 3.4% of ethanol by 2012 (http:// transport.govt.nz/assets).

Based on a recent briefing of the European Environmental Agency, Table 1.2 gives an estimate of biomass potential in the EU25 from 2010 to 2030.

Table 1.2 *EU25 biomass production potential (figures illustrate only the energy content of the primary resource). Sources: 2003 data from EUROSTAT; projections for 2010, 2020 and 2030 from European Environmental Agency, "How much biomass can Europe use without harming the environment", briefing 2/2005. (Mtoe: Million tons of oil equivalent)*

Mtoe	Biomass consumption, 2003	Potential, 2010	Potential, 2020	Potential, 2030
Wood direct from forest (increment and residues)	67	43	39-45	39-72
Organic wastes, wood industry residues, agricultural and food processing residues, manure		100	100	102
Energy crops from agriculture	2	43-46	76-94	102-142
TOTAL	69	186-189	215-239	243-316

Compared to Bio-fuel consumption in 2003, the bio-fuel production in 2030 is forecast to increase by a factor or 3.5 – 4.5. Most of it will be used for transportation.

1.3 Classification of Motor Vehicle Particulate Matter

1.3.1 Size-wise Classification

Aerosol particles cover a size range from a few nanometres to several tens of microns. Size is often expressed by a derived diameter which refers to the way particles behave under certain forces. Two commonly derived diameters are based on aerodynamic and electrical mobility forces. Typical particles can be sorted into three distinct types based on their size, and these are labelled: nucleation mode (nuclei mode) (<100nm), accumulation mode (100-900nm) and coarse mode (>900nm), as shown in Fig. 1.2. Coarse mode particles are not often emitted directly by engines, but formed from the other two modes. In addition, the comparative rarity of coarse modes results in little study of them.

Most research on nucleation mode particles suggests that the nucleation mode particles consist of volatile material, however, other researchers suggest some nucleation mode particles are solid or possess solid kernels.

Accumulation mode particles have been investigated with the greatest attention. The obvious feature is that they consist of a collection of much smaller primary particles with a solid carbonaceous core, “spherules”, whose size ranges from 20 to 50 nm. The size of accumulation mode particles varies with the number of spherules, which can range from a handful to several thousand with the form of both clusters and chains. An outer layer of volatile compounds is attached to these agglomerates.

Fig. 1.3 gives a general view of the size of these three modes.

The figure originally located here has been removed from this version of the thesis for copyright reasons.

Fig. 1.3 *Some typical particles depicted schematically: coarse mode, nucleation mode, accumulation mode (Eastwood, 2007)*

Generally speaking, the nucleation mode particle emissions depend on the dilution process, i.e. the way the exhaust gas is handled. In this sense, the accumulation mode is more likely to represent the actual emission from an engine.

1.3.2 Composition-wise Classification

Introduction of Different PM Fractions

Composition-wise, there are five distinct fractions: organic, sulphate, nitrate, ash and carbonaceous. The first three are volatile and the last two are non-volatile. The organic fraction contains thousands of compounds such as esters, aromatics, alcohols, etc. The sulphate fraction is sulphuric acid and the water associated with it. The nitrate fraction denotes nitric acid. The ash fraction consists of metals and also a few non-metals, which are incombustible. The carbonaceous fraction is mainly carbon. The detailed particulate composition for these five fractions is illustrated in Fig. 1.4.

The figure originally located here has been removed from this version of the thesis for copyright reasons.

Fig. 1.4 *Conceptual model of five distinct particulate fractions: sulphates, nitrates, organics, carbonaceous and ash (Eastwood, 2007)*

Of the aforementioned five fractions, two of them (ash and carbonaceous) are generated within the engine; the others form later in the exhaust system, or when the exhaust plume enters the surrounding air or the dilution system, although important precursor reactions take place within the engine.

Particulate matter emerging from the engine arises from four distinct sources: fuel, lubricant, air and material breakdown. The carbonaceous fraction forms within the engine, which means this formation is complete by the time the exhaust valve opens. The ash fraction is probably formed within the engine as well, however, some gas-to-particle conversion within the exhaust system could also occur to form ash (Eastwood, 2007). The sulphate and organic fractions are the most volatile compounds and form at the end of the exhaust system such as in the exhaust plume or dilution tunnel.

Formation Mechanisms of Different PM Fractions

When there is insufficient oxygen for complete oxidation, the carbonaceous fraction forms in the engine by pyrolysis of fuel, by which fuel molecules, containing a mere handful of carbon atoms, are converted into soot particles, containing tens of thousands of carbon atoms. However, the greatest sooting tendency is seen not in the complete absence, but in the presence of a certain amount of oxygen, which is attributed to a 'sensitizing' role in the pyrolytic reactions (Griffiths and Barnard, 1995). The nuclei formed in this process are of one or two nanometres in size and contain as few as fifty carbon atoms, upon which spherules are created by surface growth into a size range of 20-50 nm (Richter and Howard, 2000). Spherules then continue growing by physical collision and adherence to one another. This process is described as agglomeration, by which the number of particles decreases but the mass of soot keeps constant. Due to the lower temperature of the wall than that of the bulk gas, soot can deposit onto the wall without oxidation. Once temperatures have fallen, re-entrainment of deposited soot could happen. Thermophoresis is well known as the chief deposition mechanism in fostering particle transport in a thermal boundary layer. This will be discussed in the next section.

The organic fraction arises from fuel in two ways: the direct path is when fuel escapes combustion and passes through the engine; the indirect path is when pyrolytic reactions are interrupted in their conversion of fuel to soot: for example, if they are quenched by continued mixing, and molecules of fuel partly undergo modification with carbonaceous fraction formation being interrupted (Fujiwara *et al*., 1993; Foster *et al*., 2002).

In fact, the organic fraction is the feedstock for the carbonaceous fraction, which can explain a widely observed trend in the particulate emission from diesel engines: the composition is organic at low load, and carbonaceous at high load. At low load, temperatures are too low to initiate pyrolytic reactions to form a carbonaceous fraction, instead, the organic fraction will be emitted from engines. After the exhaust gas leaves the engine, Polycyclic Aromatic Hydrocarbons (PAH) in the exhaust will play a significant role in chemical reactions within the organic fractions. Ongoing chemical reactions are thought to underpin the conversion of PAH to more mutagenic Nitrated Polycyclic Aromatic Hydrocarbon (NPAH), although genuine reactions are poorly distinguished (Barale *et al*., 1992). Organic fractions are also subject to the gas to particle conversion during the late stages in the emission process, i.e. in the exhaust plume or the dilution tunnel. Adsorption and desorption of organic fractions in the exhaust system could change the number of particles markedly (Eastwood, 2007).

Ash compounds in the fuel give rise to the ash fraction. These inorganic components are sometimes deliberately added to the fuel to improve various aspects of the combustion; at other times they are introduced through contamination in the fuel distribution network (Akinlua *et al*., 2007). The exact chemical reaction pathways in combustion are poorly understood.

The sulphur component of both fuel and oil gives rise to sulphate fraction emissions in the exhaust. Initially, SO_2 is emitted from the engine with only a few percent of SO_3 attached. Oxidation catalysts and existing oxidative particles start the conversion

reaction from SO_2 into SO_3, which promptly undergoes hydrolysis to sulphuric acid, H_2SO_4. This acid undergoes gas to particle conversion by absorbing additional water.

1.4 Sampling of Particulate Emissions

1.4.1 Mechanisms of PM Transport and Transformation

Transport and Deposition

Particle transport does not necessarily follow the passage streamlines of the sample aerosol. Some transport mechanisms that could make particles divert from the streamlines include: interception, thermophoresis, diffusion, sedimentation, electrostatic attraction and inertia.

The simplest type of transport mechanism is interception. When a gas is in motion, the particles suspended within it will follow the streamlines and pass sufficiently close to a surface to be captured. However, interception is not normally a significant deposition mechanism due to the fortuitous nature of the geometry of particles (Eastwood, 2007).

When a particle is situated in a temperature gradient, so that one side is hotter than the other, the particles will move from the hotter side towards the colder side due to the imbalance of pressure (collision kinetics). This transport mechanism is called thermophoresis. For particles of a few hundred nanometres, thermophoresis is often the only significant deposition mechanism.

Particles are often electrically charged by ions in the atmosphere courtesy of natural ionizing radiation (Hinds, 1982). Charged particles migrate towards oppositely

charged surfaces or away from similarly charged surfaces. For this reason, materials susceptible to charge build-up (such as Teflon) should be avoided in the construction of sampling lines.

The transport mechanism of diffusion is characterized by the stochastic action of particles, especially of particles smaller than 50nm. Brownian motion arises from random buffeting by gas molecules; a similar motion was observed for smoke particles and the connection between this motion and that predicted for gas molecules by the kinetic theory of gases was made. Rather than rebounding when colliding with a surface, as with gas molecules, aerosol particles can adhere to it. This means that the aerosol concentration at the surface is zero and that a gradient is established in the vicinity of the surface, which leads to a gradual decay in concentration (Hinds, 1999). This Brownian motion drives particle diffusion, with the smallest particles being caught easily because of the great rapidity of their diffusion towards surfaces (Eastwood, 2007).

As all particles possess a mass, they experience forces of inertia and gravity. Consequently, whenever streamlines change direction abruptly, only the lighter particles remain along them, the heavier ones retain their original velocity vector. Inertia is behind the concept of isokinetic sampling, which describes the procedure to ensure that a representative sample of aerosol enters the inlet of a sampling tube when sampling from a moving aerosol stream (Hinds, 1999). The ratio of flow rates and the ratio of cross-sectional areas between the sampling probe and the conduit must be equal; otherwise, the streamlines are locally distorted, and the particle size distribution of the sample is not representative of the aerosol prior to sampling.

Therefore, sharp bends and long horizontal tubing should be avoided for sample lines, to diminish inertial and gravitational deposition.

Transformation and Mutation

Mutation leads to continual modification in terms of particle size, shape, form and composition according to the prevailing conditions. The volatile species are primary contributors to this mutability, since these species are readily subject to gas-to-particle and particle-to-gas conversion. The gas-to-particle conversion is governed by saturation, which denotes the maximum amount of any volatile species that is able to exist in the gaseous phase. The saturation can be mathematically expressed by the ratio of partial pressure to saturation vapour pressure (Hinds, 1982), which is termed the saturation ratio. Condensation into the particle phase occurs when the saturation ratio is above a certain value; in contrast, adsorption for gas-to-particle conversion occurs when the saturation ratio is below the threshold. For lower values of saturation ratio (<1.0), the increasing saturation ratio causes an increase in the organic adsorption to available surface area (of carbonaceous particles). As the saturation ratio approaches 1.0, condensation of organic matter starts. If it is sufficiently high (3 to 4), which is likely if there is insufficient particle surface available in the exhaust for extensive adsorption, new particles may form by homogeneous nucleation from the gaseous phase.

Nucleation is one type of condensation which contributes to the generation of new particles: it takes place on pre-existing kernels which are too tiny to be commonly thought of as particles. The greater the availability of condensable material, or the

higher the saturation ratio, the smaller the kernel needed to commence nucleation. Depending on whether the particle formation is mediated by the nucleating substance itself or foreign material, two types of nucleation are possible: homogeneous nucleation and heterogeneous nucleation. Heterogeneous nucleation is the more usual type because it requires less super-saturation. For instance, the value of the saturation ratio is normally found to be less than 1.0 for the hydrocarbons associated with SOF of diesel PM, and thus heterogeneous nuclei in the form of sulphuric acid and possibly metallic ash are the likely precursors to the formation of hydrocarbon containing nano-particles. It is also reported that sulphuric acid may nucleate in mini-dilution systems at dilution ratios ranging from 10 to 50 (Kittelson *et al*., 1999).

With the right conditions, a substantial increase occurs in particle formation. Nucleation is boosted by a high volatile/non-volatile ratio, while if it is low, condensation and adsorption are more likely to occur. The adsorption of volatile materials onto carbonaceous particles (when the exhaust is cooled) depends on the particle surface area available as well as the value of the saturation ratio. Thus an engine producing a large amount of volatile material with a high level of carbonaceous particles (in the case of older engines) is likely to have less particle nucleation and growth compared to an engine producing an equal amount of volatile matter but a low amount of carbonaceous matter (as in the case of newer engines) (Kittelson, 1998).

1.4.2 Effects of Sampling Conditions on PM Measurements

It is also important to understand the effects of testing conditions on the nature of the exhaust PM being investigated. The identified key environmental or test parameters include (Kittelson *et al*., 1999):

- The dilution ratio (DR) and the resulting saturation ratio
- The time the particles spend at varying dilution ratios or sampling conditions (residence time)
- The humidity and temperature
- The background particle and gas concentrations

Dilution parameters have a strong influence on particle number and size distributions. The dilution ratio, residence time, dilution temperature and humidity in the dilution system affect particle measurements significantly. Much research work has been documented to investigate such effects on PM measurements (a major focus on fine or nucleation mode particle size distribution) such as Luders *et al*. (1998); Abdul-Khalek *et al*. (1999); Shi and Harrison, (1999); Lapuerta *et al.* (1999); Andersson *et al.* (2000); Mathis *et al.* (2004); Lipsky and Robinson, (2006). Based on the cited references the following can be summarized:

- Conditions of high dilution ratio and high relative humidity (RH) and low temperature tend to favour the production of nano-size particles as a result of a higher nucleation rate (Shi and Harrison, 1999).
- Longer residence time favours further nucleation and thus tends to increase total particle number concentration; at low dilution ratio and low temperature,

the influence of residence time is the strongest and causes the highest concentration in nano-size particles (Shi and Harrison, 1999; Abdul-Khalek *et al*., 1999).

- Total particle number concentration decreases as the dilution ratio increases for the same dilution temperature and residence time. For a constant DR, a temperature increase can cause a decrease in number concentration. However, a shorter residence time (such as 100ms) makes DR and dilution temperature have insignificant effects on PM number concentration (see Fig. 1.5).
- Dilution conditions markedly change the size distribution of the nuclei mode particles, but not of the accumulation mode particles. Since the nuclei mode particles normally dominate the number concentration rather than the mass or volume concentration, dilution effects are only significant for nucleation mode particle measurements. It also indicates that the soluble organic fraction (SOF) in PM is mainly affected by the dilution conditions.
- Most of the nuclei mode particles may be formed during dilution apparently from volatile particle precursors as have been observed by Wei *et al*. (2001) in their research work.
- Dilution conditions such as DR and filter temperature had minor effects on specific PM mass emissions for dilution ratios of about 20 and above. Below this point increasing DR decreased the specific PM mass emission. However, increasing the RH in the filter conditioning chamber can increase the insoluble fraction of PM with a minor effect on the SOF (Lapuerta *et al*., 1999). Lipsky and Robinson (2006) found a significant decrease in PM mass emissions for increased dilution ratios when the engine was operated at low loads but insignificant effects at medium loads.

- According to SEM analysis, the mean size of the particles was reduced with increasing DR (Lapuerta *et al.*, 1999).
- Test conditions that favour the formation and measurement of increased diesel particle number concentrations are: low dilution ratio, long residence time, high RH (Relative Humidity), and high fuel sulphur content (Abdul-Khalek *et al*., 1999).

The figure originally located here has been removed from this version of the thesis for copyright reasons.

Fig. 1.5 *Influence of Residence Time, Dilution Temperature, and Dilution Ratio on Particle Concentrations. PDR, PRT, and PDT denote primary dilution ratio, primary residence time, and primary dilution temperature, respectively (Abdul-Khalek et al., 1998)*

1.5 Engine-out Particulate Emissions

1.5.1 Comparison of Particulate Emissions among Different Types Engines

Because of increasingly stringent statutory regulations, the particulate mass in diesel engine exhaust has declined by over two orders of magnitude, with the difference in particulate emissions between gasoline and diesel engines dwindling to a few tens of percent (Andrews *et al*., 1998). A number of researchers have shown that gasoline engines produce much smaller particles (nanoparticles) than diesel engines. Hence,

should particle size be a more relevant toxicological metric than the total mass of particulate matter, then gasoline vehicles may pose a greater hazard in public health terms than diesels (Mohr *et al*., 2006).

During steady-state driving, cruise or light loads, port-injection engines emit little particulate matter, however, they become great emitters during other driving conditions requiring fuel enrichment, such as cold starts, hard acceleration and full load (Kayes *et al*., 1999; Andrews *et al.*, 1998). Even when they are operating on globally stoichiometric air-fuel ratios, fuel droplets could enter the cylinder due to inadequate fuel vaporization, which can favour soot formation. The greater volatility of gasoline, compared with diesel, implies a lesser contribution to the organic fraction. In fact, this fraction is suspected to consist predominantly of unburned lubricant oil. Analysis of the particulates from SI engines showed that the bulk of the mass was ash and the second largest fraction was unburnt lubricating oil. Soot emissions were only significant at high power WOT (Wide Open Throttle) with fuel enrichment, and at other conditions soot was less than 10% of the total mass (Andrews *et al.*, 1998).

Accumulation mode particles emitted from port-injection engines are agglomerates of approximately mono-dispersed spherules. At rich air-fuel ratios, port-injection engines tend to produce more carbonaceous fraction with the filter in the dilution tunnel being black, whereas at lean air-fuel ratios, they are likely to emit more organic fraction with the filter being yellow. On statutory driving cycles, vehicles emit particulate mass at 1-2 mg/km, and 10^{12}-10^{13}/km in number. Instantaneous

measurements show that PM emissions increase during the acceleration mode, but then fall back when the cruise condition has been reached (Mohr *et al*., 2000).

Studies on particulate emissions from Direct Injection Spark Ignition (DISI) gasoline engines have revealed that they are significantly higher than port fuel injected engines due to the reduced time available for mixture preparation and increased incidence of fuel impingement onto pistons and combustion chamber surfaces (Price *et al*., 2006). The current project is with DISI engines, therefore the literature on DISI engines regarding particulate emissions has been reviewed, the results of which are summarized in the next section.

1.5.2 Particulate Formation in GDI Engines

Mechanisms of Particulate Formation in DISI Engines

At a first level, the explanation for soot emission is that stratification of the charge inevitably confers some local regions of rich mixture, for instance, the vicinity of the spark plug, where the formation of soot is likely to take place (Yang and Kenney, 2002). There is also less time available for fuel evaporation and hence fuel droplets would survive at the start of combustion. Combustion proceeds in two stages within the engine: firstly, a soot-forming flame front propagates through the charge; secondly, a soot-oxidizing flame front propagates through the gases left by the first flame front (Kuwahara *et al*., 1998).

On a second level, soot arises in direct injection engines through the impingement of fuel onto the piston or other surfaces. Droplets accumulate on the piston surface to form liquid pools, which burn belatedly via diffusion flames with highly sooting

effects (Alger *et al*., 2001). Injection timing determines not only the time available for pool evaporation, but also the distance traversed by the spray. Therefore, an early injection (300º CA bTDC), i.e. 300 crank angle degrees before combustion top dead centre, could produce no pool fires. This pool evaporation may be subject to the Leidenfrost effect (Matthews *et al*., 2001): should the temperature of a surface significantly exceed the boiling point of a liquid impinging onto that surface, then an intervening layer of vapour is generated. This is why when water is poured onto a hot metal surface, the droplets can hover on cushions of their own vapour. The intervening cushion of vapour has an insulating effect, due to the inhibition of heat transfer from the surface to the liquid. This insulating effect can slow evaporation by as much as two orders of magnitude. However, the Leidenfrost effect seems restricted to cases where the in-cylinder pressure is low, such as during the intake stroke or the early stage of the compression stroke. This is because the cushion of insulating vapour underneath the fuel is compressed at high pressure and hence the heat transfer increases.

As for DISI engines, catalysts are the undoubted trigger for sulphuric acid, which is strongly dependent on the fuel sulphur content. Research has shown that 30-40% of the fuel sulphur was being converted to sulphuric acid, whereas on vehicles without catalysts, the figure was less than 2% (Beltzer *et al*., 1974). Originally, the sulphur was emitted from the engine as SO_2. In the exhaust, it converts to SO_3, and the SO_3 swiftly converts to H_2SO_4, which readily undergoes gas to particle conversion. The bottleneck in this reaction chain is conversion from SO_2 to SO_3, which is kinetically negligible in a vehicle without a catalyst. Contrarily, a high conversion is predicted above the catalyst light-off temperature. In addition, gasoline oxidation catalysts, like

diesel oxidation catalysts, exhibit remarkable propensities for sulphur storage. This acid could be discharged in sudden bursts during transient operation (Smallwood *et al*., 2001). The presence of three-way catalysts in gasoline vehicles makes the air-fuel ratio stoichiometric or nearly so, hence the exhaust can no longer be oxidizing overall and acid formation is fortuitously inhibited.

Comparison of the Two Generations of DISI Engines regarding PM Emissions

Stratified direct fuel injection combustion systems have been developed by different OEM's for several years. First generation systems used side mounted injectors with wall guided or air guided mixture formation. Further improvements, especially in fuel economy, can be achieved by second generation engines with spray guided direct injection (SGDI), which accomplishes a major increase in the stratified operational window, as well as an improved efficiency from the stratified combustion process. Especially the combination of downsizing, spray guided direct injection and turbo-charging (SGDI TC) offers a significant fuel economy improvement potential without any compromises regarding driveability (Wirth *et al*., 2004).

First generation DISI engines are known to emit high levels of PM emissions: Maricq *et al.* (1999) reported PM number concentrations as high as $5x10^7$ particles/cm^3 and an increase between a factor of 10 to 40 going from homogeneous to stratified mode. Graskow *et al.* (1999) used a Scanning Mobility Particle Sizer to measure the PM emitted by a PFI-SI engine and found a stable baseline of about 10^5 particles/cm^3 with occasional spikes. This suggests an increase of about one to two orders of magnitude

between PFI and DISI engines. Wirth *et al.* (2004) present smoke-meter measurements for different Brake Mean Effective Pressures (BMEPs) in a prototype SGDI engine, and cite the reduction of smoke emissions as one of the main drivers for developing SGDI.

A comparison of PM emissions between single-cylinder SGDI and DISI engines was conducted using different types of fuel. In addition to a reduction of the emitted PM mass, it was found that the PM emitted by the SGDI engine was dominated by nucleation mode PM, like a conventional Port Fuel Injection Spark Ignition (PFI-SI) engine, and the accumulation mode normally associated with DISI engines was not detected (Price *et al*., 2006); this result is shown in Fig. 1.6.

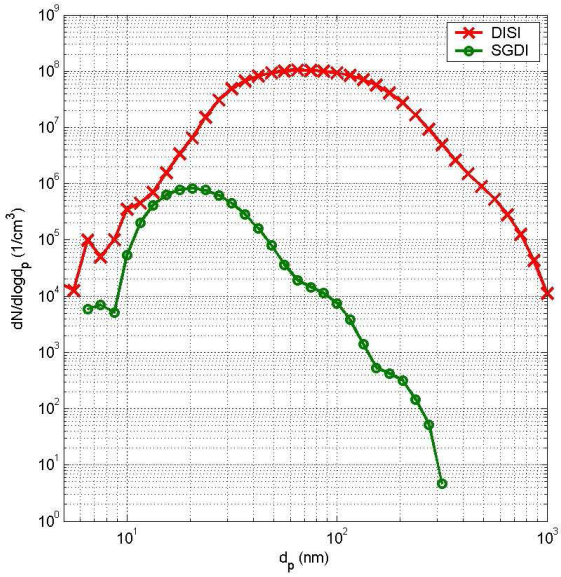

Fig. 1.6 *Representative PM size distribution for the DISI engine and the SGDI engine (Price et al., 2006)*

Fig. 1.6 shows the significantly larger accumulation mode PM emissions from the DISI engine under a part load condition. On average, the total number concentration is about an order of magnitude smaller for SGDI than wall guided DISI, with the

mean particle size also found to be smaller. There is less than an order of magnitude difference between SGDI and PFI. This is small compared to the DISI case where the difference is closer to two orders of magnitude. In both the SGDI and DISI case, the time for mixture preparation is reduced. It follows that there will be more liquid fuel in the cylinder, which could then form PM (Kayes *et al*., 1999).

The reduction in PM emissions for SGDI as compared to DISI can be attributed to the higher injection pressure, relatively better mixture preparation and reduced impingement of fuel on the combustion chamber surfaces. A set of parameters which could influence PM number concentration and size spectra were investigated with the descending order of importance being as follows: fuel type, air fuel ratio, SOI and ignition timing (Price *et al*., 2006). Other research demonstrates that particulate emissions exhibit a strong sensitivity to injection timing; generally particle number concentrations increase steeply as the injection timing is retarded. Increasing speed and load both cause higher particulate emissions; however, for stratified charge operation these general trends are strongly influenced by injection timing (Maricq *et al*., 1999).

1.6 Techniques for PM Measurement

Particulate emissions can be measured on-line on a number basis using the Differential Mobility Spectrometer 500 (DMS500) and there is also a range of analytical techniques available to determine the composition and morphology of the PM, such as Thermo-Gravimetric Analysis (TGA), X-ray Photoelectron Spectroscopy (XPS), Raman Spectroscopy (RS) and EM (Electron Microscopy). The techniques deployed in this project are now described in more detail.

1.6.1 Differential Mobility Spectrometer 500 (DMS500)

The Differential Mobility Spectrometer 500 (DMS500), which is manufactured by Cambustion Ltd., is a real-time instrument for measuring size distribution and number concentration of the PM. Electrical mobility can be measured by a charged particle being deflected in an electric field, and is a function of both the charge on the particle and its aerodynamic drag. Both of these parameters are in turn functions of particle diameter, therefore by measuring the electrical mobility of particles, their size can be calculated.

Particles enter the DMS500 via a cyclone which removes particles bigger than the maximum measurable particle size of the instrument (1000 or 2500nm). They are then electrically charged by collision with air ions, in a process known as diffusion charging. As shown in Fig. 1.7, the charged particles enter the classification column and are carried along it by a sheath of clean air. Within the column they are subjected to a radial electric field from a central high voltage electrode which either repels or attracts the particles towards the outside of the column. Particles which are of low electrical mobility will be repelled to the outside slower than highly mobile particles, and hence will travel further down the column before impinging upon one of a series of electrometer rings along the length of the column. These measure the electrical current from the arrival of charged particles, and thus their concentration. A computer-modelled transfer function in the DMS 500 is used to calculate the size distribution of particles from the electrometer currents. This transfer function will be discussed in-depth in Section 2.4.

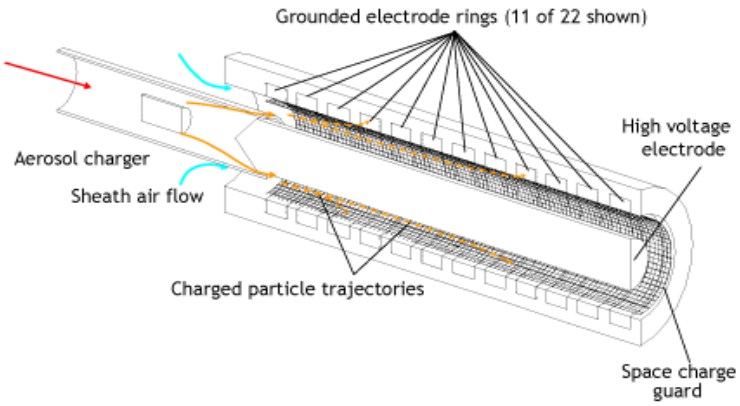

Fig. 1.7 Internal construction and operating principle of the Cambustion Ltd DMS500 (http://www.cambustion.com)

Since the instrument detects particles which collide with the electrometer rings, these rings will slowly accumulate particle deposits. In addition, the space charge guard, which shields the electrometers from noise, also accumulates dirt. Therefore, the classifier and the central HT rod must be cleaned periodically (normally once per 6 months) to reduce the instrument noise level. The cleaning procedure can be found in the DMS500 User Manual.

1.6.2 Thermo-Gravimetric Analysis (TGA)

In the automotive industry, the most established method of thermal fractionation is thermo-gravimetric analysis (TGA), where a PM sample is collected on a glass fibre filter which is then placed in a chamber and weighed as a function of increasing temperature.

The principle of this technique is straightforward: different fractions of particulate emissions are lost at different temperatures, showing the weight of particulates remaining on or escaping the filter as a function of time. Two pivotal operating parameters associated with this technology are the ramp rate of temperature change

and the temperature of demarcation at which the chamber atmosphere changes from an inert one to an oxidising one. Both operating parameters are not, as yet, subject to any standardization. Therefore, the agreement of results between different laboratories should not be expected (Eastwood, 2007). A Perkin Elmer Pyris TGA facility (see Fig. 1.8) is available for use, which is located in the Department of Materials at the Begbroke Nano-Materials Characterisation Facility. The TGA is used in conjunction with a Thermal Analysis Gas Station (TASS) to provide programmable control of all gases used in the TGA test. It will be further discussed in Section 5.2.

Fig. 1.8 Perkin Elmer Pyris TGA instrument (http://las.perkinelmer.co.uk)

There are two operational parameters which could affect the results significantly: the rate of temperature rise and the demarcation temperature. If the ramp rate is too high, evaporation is impeded because of insufficient time for volatile compounds to diffuse away from the vicinity of the surface. The impeded volatile fractions are now released at a higher temperature, which will obviously confound the results (Cuthbertson *et al*., 1979). If the ramp rate is too low, the measurement is protracted, and the penetration of oxygen into the chamber becomes significant (Cuthbertson *et al*., 1987). The second vital operating parameter is the demarcation temperature at which the oxidizing atmosphere replaces the inert one. If it is too high, the carbonaceous

fractions undergo artefactual transformation during the first phase in the inert atmosphere. If it is too low, volatile compounds are misclassified as non-volatile compounds.

1.6.3 Fast Flame Ionization Detector (fFID)

In-cylinder hydrocarbon (HC) measurements using fast flame ionization detector (fFID) probes have been used in engine research groups to provide a semi-quantitative information on mixture preparation and charge stratification. A gas sample is taken from the cylinder and the HC molecules within it are burned in an electric field. The combustion of HC molecules produces a current flow corresponding to the number of carbon atoms burned so that the output of the instrument is proportional to the mass flow rate of hydrocarbons in the sample being examined. While the instrument actually measures HC concentration at a point, at the spark plug in this work, its results can be indicative of global mixture behaviour (Crawford and Wallace, 1996).

Sleightholme (1990) used a fFID to study charge homogeneity in a single-cylinder research engine. Gas samples were taken from the combustion chamber via an auxiliary spark plug port (Sleightholme, 1990). Meyer and Thring (1995) used two fFID probes mounted in a specially adapted spark plug to determine the degree of stratification and vaporization existing in the vicinity of the spark plug. Similarly, Queenan *et al*. (1996) used a simultaneous two-probe technique to estimate the degree of charge stratification achieved by means of a novel injection strategy.

There are a number of practical problems associated with direct in-cylinder sampling using the fFID. One of the major difficulties is establishing the transit time of the

instrument. The transit time is a function of engine pressure and it is therefore variable throughout the engine cycle. Validated steady state and quasi-steady state flow models exist, however, considerable care is required to match the probe geometry and flow model (Summers and Collings, 1995). In addition, it should be noted that the instrument responds to both the mass flow rate and HC concentration, therefore, in order to obtain valid HC measurements a constant sample mass flow rate must be maintained. Accordingly, a constant pressure differential between the flame ionization chamber and sample line is required. In practice, it is very difficult to maintain the pressure differential constant due to the fluctuations in the cylinder pressure. However, Crawford and Wallace (1996) found the fFID is relatively insensitive to the sample pressure.

Unfortunately the FID does not respond equally to all carbon atoms, and in particular it has a significantly reduced sensitivity to carbon atoms in oxygenated compounds. Cheng *et al.* (1998) found that when the sample flow contains oxygen, there are changes in the flame temperature, in the geometry of the flame, in the geometry of the ion generation region, and in the competition between formation of flame ions and oxidation of the hydrocarbon fragments; as a result, the FID signal is sensitive to the sample flow oxygen content, which usually leads to a decrease of the response function. (This effect is often termed oxygen synergism.)

1.7 Implications of Gasoline/Alcohols Blend Fuels

The motivation for blending ethanol with gasoline is to reduce the net emissions of carbon dioxide, but it is also important to know the impact on local and regional air quality that arise from gasoline-powered vehicles (Graham *et al*., 2008). Ethanol was

used as an automotive fuel in the USA in the 1920s and the Model T Ford could be modified to run on either gasoline or pure ethanol (DiPardo, 2000). However, ethanol was not widely used until after 1970 (Poulopoulos *et al*., 2001). Nowadays, ethanol blends have gained a reasonable amount of attention as ethanol is seen as one of the most promising renewable fuel sources for vehicles to tackle issues of global warming and fossil fuel depletion.

A great deal of research has focused on the measurement of PM emissions from diesel engines using different fuels of different compositions (Kim and Choi, 2008). This generally suggests that the reduction in PM emissions is attributed to the 'leaning effect' of oxygen in the fuel molecule (Hsieh *et al*., 2002). In other words, the reduction in PM mass emissions is correlated with the amount of oxygen in the fuel molecule. However, gasoline applications would not necessarily have the same response to the addition of ethanol because of the great difference in operational principles and compositions of PM between diesel and GDI engines. On one hand, soot in gasoline PM is normally lower than that in diesel PM which means gasoline PM would be less affected by oxygen atoms in the fuel (assuming that oxygen atoms only affect soot by curbing soot precursors). On the other hand, a gasoline fuel spray seems to break-up and evaporate more than an ethanol spray (Serras-Pereira and Aleiferis, 2008) which may well increase PM emissions when ethanol is used due to its poorer relative evaporation. The absence of experimental data means that there is a clear need to investigate the effect of oxygenate additions on GDI PM emissions. Chapter 6 will address this question based on the engine tests with a range of gasoline/ethanol blends. It concludes that adding ethanol produced higher Pn (Particulate number) and Pm (Particulate mass) than base fuels under the same steady-

state stoichiometric operating conditions. This is due to the fact that the higher enthalpy of vaporization and lower calorific value of ethanol led to greater in-homogeneity in the mixture within the cylinder at the time of ignition.

It is also found in this work that adding ethanol produced a larger spray projected area and protracted the vaporization process under both cold and warm conditions. Similar results were found as follows. Serras-Pereira et al. (2008) found that a ULG fuel spray seemed to break-up and evaporate to a larger extent than an ethanol spray. Aleiferis et al. (2010) investigated the spray characteristics in an optical chamber and an engine with gasoline and its E85 blend. The main findings included: the E85 spray on the swirl plane was observed to collapse to a lesser extent than gasoline; droplet sizes were larger for E85 than for gasoline at all conditions. Su Han Park *et al*. (2009) also pointed out that ethanol has a lower Reynolds number ($\mathrm{Re} = \rho VD/\mu$) which indicates a smaller turbulence intensity which will affect the break-up of fuel droplets. In addition, ethanol blends have a low Weber number ($\mathrm{We} = \rho V^2 D/\sigma$) determined by the high surface tension and fuel density, which leads to a slow break-up process.

In addition to ethanol, butanol is also being developed as a possible gasoline extender. This may be advantageous from a fuel blending, handling and storage perspective. Butanol is less polar than the lighter alcohols and so is less likely to separate from (non-polar) gasoline. The volumetric energy density is also closer to conventional gasoline, which is good from a commercial stand-point. It is worth noting that the high enthalpy of vaporization and good anti-knock properties of methanol and ethanol are considered positively as they help enable engine downsizing which is a method of reducing the CO_2 emissions from vehicles with spark ignition engines. This synergy

would be somewhat reduced if the 'oxygenate fraction' were to come from butanol rather than ethanol or methanol (Price, 2009). The enthalpy of vaporization of butanol is roughly half of that of ethanol, therefore butanol would produce more homogeneous mixtures and lower PM emissions than ethanol.

1.8 Summary

Gasoline Direct Injection Engines have been of great interest to automotive researchers and manufacturers because of the compelling potential for reducing fuel consumption. However, the literature showed that GDI engines can emit one order of magnitude more particulate matter number emissions than conventional PFI engines. The absence of open literature on GDI particle number emissions and the upcoming number-based PM regulation make it essential to measure the GDI PM emissions using a number basis.

This chapter has presented a review of different aspects of engine-out PM emissions. It began with a brief introduction of both PM and bio-fuel legislation, which was followed by the classification of vehicle particulates (size-wise and composition-wise). The influence of sampling conditions on PM measurements has been discussed in detail as they play a significant role on the PM number concentrations. Comparison of PM emissions from different types of engine has also been reviewed and it was found that GDI engines typically produce one order of magnitude more particle number than PFIs. Finally, a review of the working principles of the measurement instruments deployed in this work has been presented, which was followed by an introduction to the implications of gasoline/alcohol blends as alternative automotive fuels.

2. Experimental Instrumentation and Data Interpretation

2.1 Introduction

Much of the experimental work described in the subsequent chapters was conducted using two test engines: a V8 AJ133 GDI engine and a single-cylinder optical access engine. Both engines were provided by Jaguar Cars and have essentially the same combustion system. This chapter is dedicated to providing the details of the test engine facilities.

Emphasis will be placed on the descriptions of the data acquisition systems for both engines, which have been designed in LabVIEW by the author. These DAQ systems facilitate extracting various experimental data at different sampling rates ranging from 1Hz to 300 kHz, and also communicating with the ETCS (Engine Timing Control System) to enable automatic data logging. An automatic dilution system for filter sampling is covered separately in Chapter 3.

The DMS500 has been extensively used in this study to obtain PM size distributions and derive PM mass distributions. Therefore the third part of this chapter discusses the DMS500 data processing in terms of conversion from the raw current matrix to size distributions, calculation of mass distributions and bi-normal fitting algorithms. A brief description of the combustion analysis of experimental data and its calculation algorithm is given.

2.2 Test Engines

2.2.1 V8 AJ133 GDI Engine

One test engine for this project is a V8 5L naturally aspirated GDI engine from Jaguar. It has four continuously variable cam torque actuated cam phasing actuators for VVT operation (Sandford *et al.*, 2009). The engine specifications are in Table 2.1.

Table 2.1 Specifications of the Jaguar AJ133 V8 SGDI engine

Bore × Stroke	92.5 × 93.0 mm
Displacement	4999 cm3
Valves per Cylinder	2 intake, 2 exhaust
Compression Ratio	11.5
Fuel Pressure	150 bar max
Injector	Multi-hole Nozzle
Emissions	ULEV2/EU4
Nominal Power	283 kW
- at Speed	6500 rpm
Max Torque	515 Nm
- at Speed	3500 rpm

The V8 engine is equipped with a production Three Way Catalyst (TWC) for reducing gaseous emissions. The two exhaust banks of the engine are joined together approximately 3-4 meters downstream of the catalysts. All the experiments carried out in this engine included PM measurements for both pre- and post-catalyst samples. The switching between the two samples is enabled by a pneumatic switching valve installed alongside the TWC. After switching, either pre- or post-catalyst exhaust will flow through the sampling pipe into different instruments, such as the DMS500, the dilution system and the AVL GmbH soot sensor. Fig. 2.1 shows the V8 engine test cell layout. The exhaust spray rotameters are used to measure the flow rate of water spraying, which is used to cool down the exhaust aerosol downstream of the TWC.

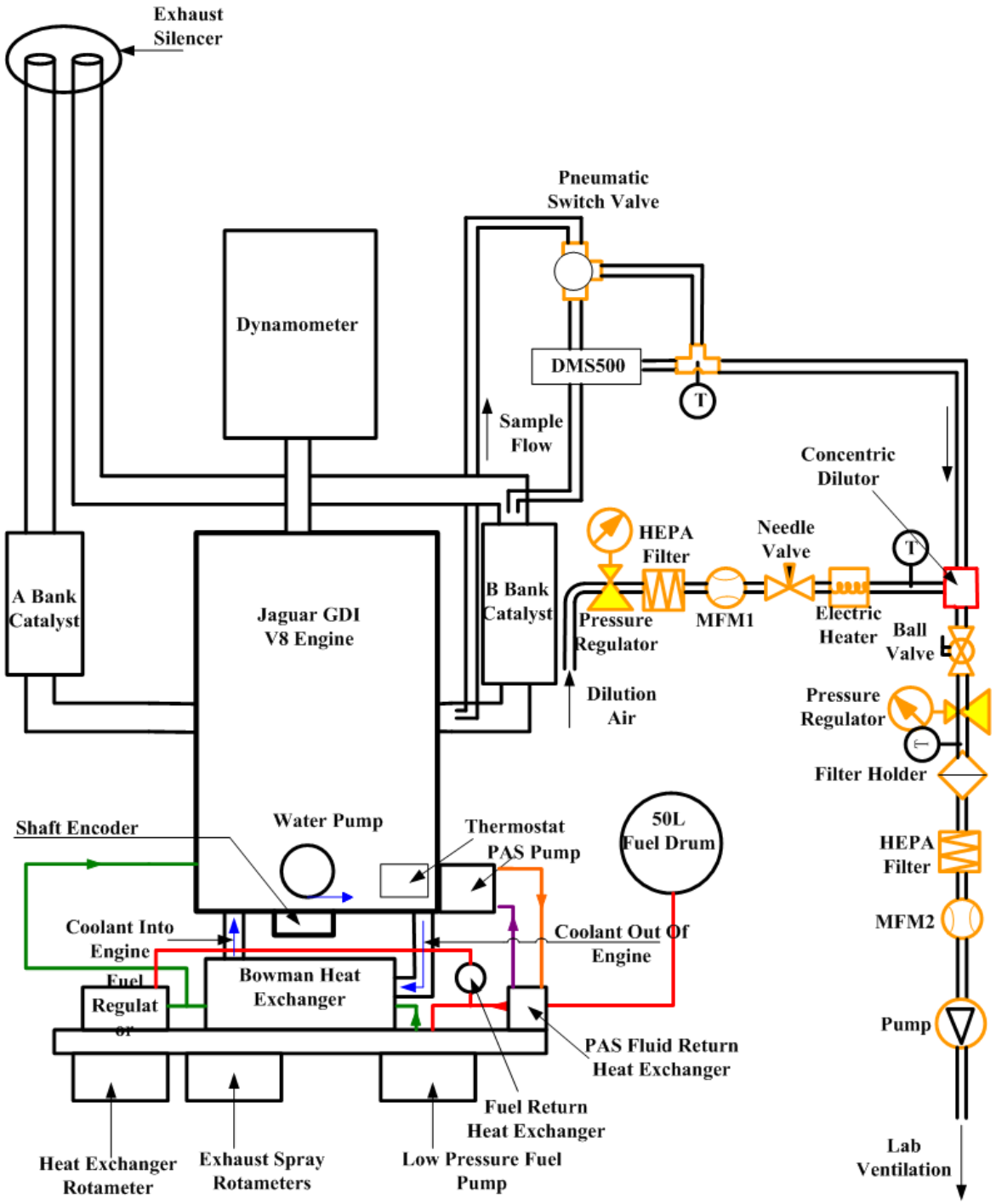

Fig. 2.1 V8 Engine Test Cell Layout

The V8 engine employs a spray guided, homogeneous direct injection combustion system. Fig. 2.2 illustrates the layout of the combustion chamber.

The figure originally located here has been removed from this version of the thesis for copyright reasons.

Fig. 2.2 Combustion system layout (Sandford et al., 2009)

The six-hole solenoid operated, fuel injector is vertically mounted in the centre of the cylinder whilst a 12mm spark plug is packaged beside the injector and is installed at an angle of 18 degrees to the longitudinal axis of the cylinder (Sandford *et al.*, 2009). The multi-hole injector produced six spray plumes which direct fuel to different regions of the combustion chamber with 2 plumes directing fuel towards the spark plug.

The V8 engine is fitted with four cam torque actuated (CTA) VCT phasers and cam profile switching (CPS) technology. The inlet and exhaust camshaft VCT phasers are designed to provide 62 and 50 degrees of variable camshaft timing respectively. A detailed description of the VVT system will be given in Chapter 5.

2.2.2 Single-cylinder Optical Access Engine

The other test engine is a Jaguar single-cylinder optical access engine. Compared to the V8 engine, it is preferred for research activity due to the absence of cylinder-to-

cylinder variations, low fuel consumption, ease of accessibility for instrumentation and availability of various optical diagnostics. However, the mass of the Bowditch piston limits the maximum engine speed to about 2000 rpm and the absence of lubricating oil in the combustion chamber means that conventional piston rings cannot be used. Instead, plastic or glass-fibre rings have to be used and these tend to require frequent replacement before gas blow-by becomes unacceptable (Price, 2009).

The single-cylinder optical access engine has essentially the same combustion system as the V8 engine shown in Fig. 2.2. Apart from the GDI injection system, there is an additional fuel injector mounted in the intake plenum, which has a large volume for mixing the fuel and air. Both the direct injector and the plenum injector are seamlessly inter-changeable with independent control of injection timing and duration. Therefore it is possible to operate the engine under two injection modes: direct injection and plenum injection. The plenum injector can also use gaseous fuelling (such as hydrogen) if required. Table 2.2 summarizes the specifications of the single-cylinder engine.

Table 2.2 Specification of the single-cylinder optical engine

Combustion System	SGDI, PFI (Plenum Fuel Injection)
Bore×Stroke	89×90.3 mm
Displacement	562 cm^3
Valves per Cylinder	4
Compression Ratio	11.1
Fuel Pressure	150 bar
Injector	Multi-hole Nozzle
IVO	33 CA aTDC
IVC	243 CA aTDC
EVO	211 CA bTDC
EVC	39 CA aTDC

The valve timings given in Table 2.2 are with respect to crank angles before or after the intake TDC. These timings can be changed manually. The combination of early EVC and late IVO mean that there is only 6º CA valve overlap around the intake TDC. A smaller valve overlap normally leads to a smaller mass fraction of residuals, and hence a lower in-cylinder gas temperature on compression. A lower gas temperature on compression will worsen the spray atomization and consequent PM emissions. On the other side, it will improve the combustion stability and fuel economy. The effects of valve timings on PM emissions and combustion performance will be discussed in-depth in Chapter 6.

2.3 Data Acquisition Systems

A data acquisition system consists of various sensors, amplifiers, analogue to digital convertors, the data acquisition card and the LabVIEW (Laboratory Virtual Instrument Engineering Workbench) software on a PC. The National Instruments^{TM} LabVIEW is a development environment based on a graphical programming language to control and communicate with the data acquisition card. This section will focus on the description of the DAQ software for both the V8 and the single-cylinder engine. Their main functions are twofold: real time calculation and display, and data logging.

2.3.1 Data Acquisition System for V8 Engine

There are 4 NI DAQ cards for acquiring a variety of experimental data on the V8 engine rig. They are operated with different triggering and clocking settings. The clock determines the speed at which the data is logged and the trigger source determines the start point of the data acquisition.

Two of these 4 DAQ cards are low speed with a sampling rate of once per cycle. These low speed data include: Manifold Absolute Pressure (MAP), exhaust pressure, high pressure fuel, low pressure fuel, coolant pressure and various temperatures such as air temperatures, exhaust temperatures, coolant and oil temperatures.

Another high speed NI DAQ card is used for logging crank angle resolved data such as in-cylinder pressures for the four B bank cylinders, crank and cam flag. A shaft encoder rotating at the engine speed provides the trigger and clock signals for the high speed DAQ card at the sampling rate of once per degree crank angle, because the shaft encoder can output both once per cycle and once per crank angle TTL pulses simultaneously. A crank flag occurring at a known angle (e.g. compression TDC) must also be logged as this is required for positioning the pressure trace with correct crank angle in order to calculate combustion performance data such as IMEP and Mass Fraction Burned (MFB) traces.

The V8 engine has a single spark plug in each cylinder and each spark plug is controlled by an individual coil-on-plug, which is connected to the engine control unit (ECU), so that each plug can be fired at any crank angle as determined by the ECU. In order to measure this HT voltage and current, a very high speed data acquisition card (VDAQ) has been integrated into the DAQ system. The ignition is dependent on the engine speed, the load and the mixture preparation, and it varies greatly during the very short ignition period, consequently the HT voltage of the spark plug can vary dramatically fast. Therefore, the VDAQ system is used to acquire data for a certain crank window every cycle at an even higher sampling rate than the aforementioned

normal high DAQ one. The default sampling rate and crank window for the VDAQ is 300 kHz and 3900 points every cycle.

Fig. 2.3 illustrates the data acquisition system for the V8 engine.

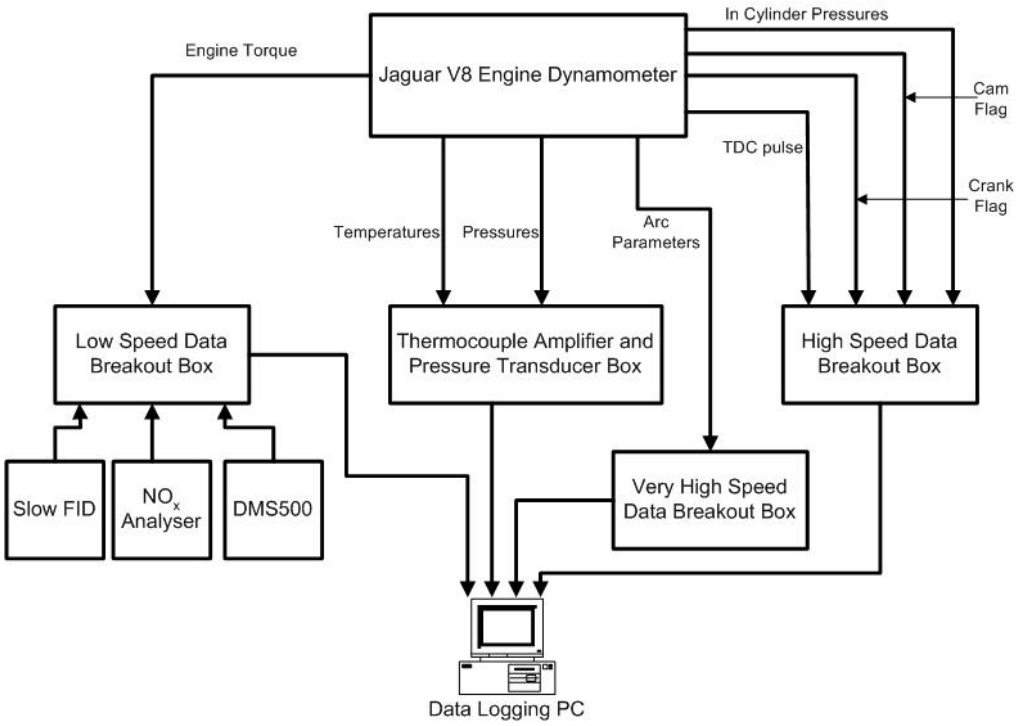

Fig. 2.3 V8 data acquisition system

The front panel of the LabVIEW software has been created for choosing data logging options (channels, clock and trigger signals) and monitoring key engine parameters as shown in Fig. 2.4.

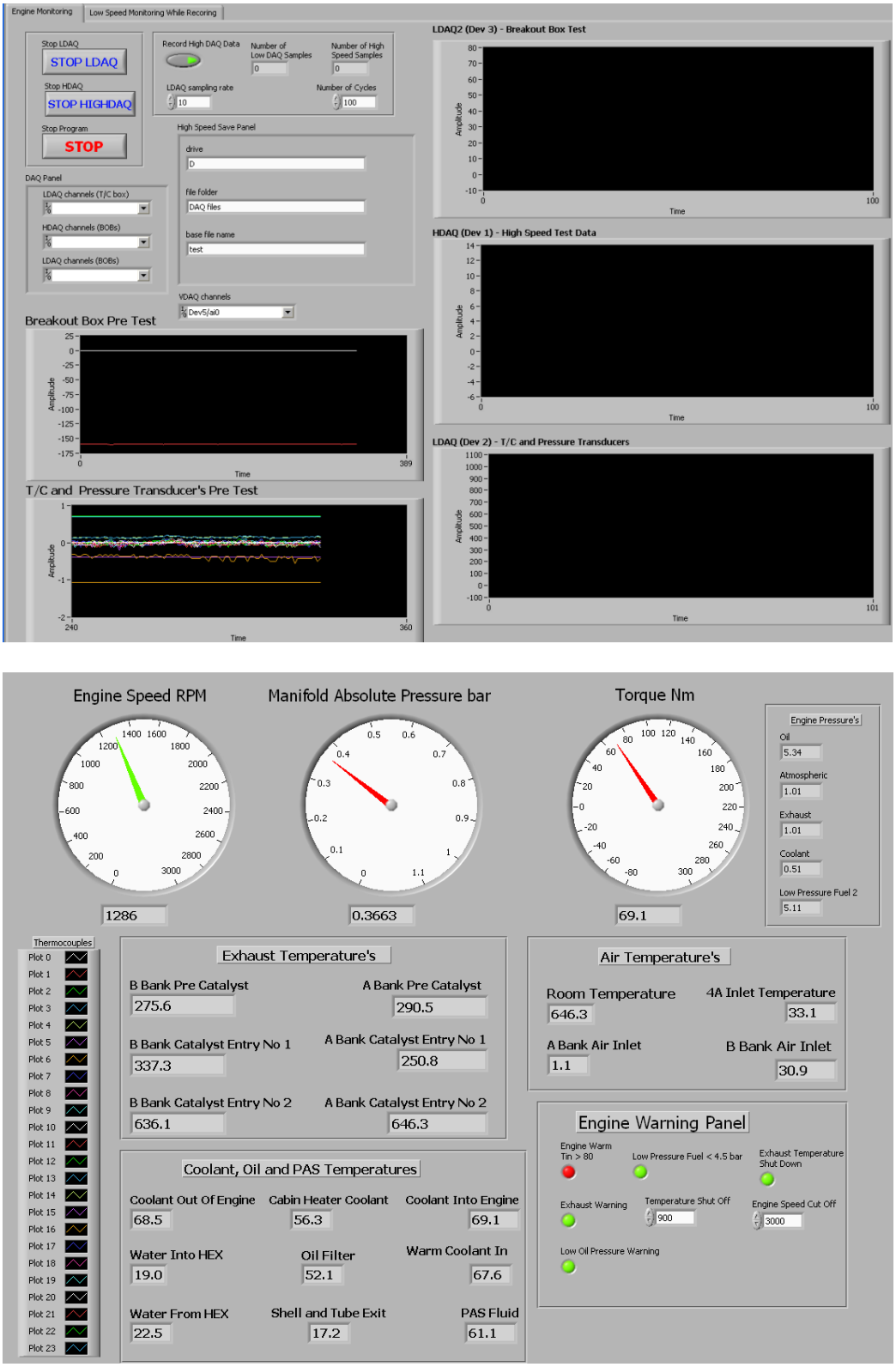

Fig. 2.4 Front panel of V8 DAQ software

The default settings for 4 DAQ cards in terms of the channels to be sampled, clocking and triggering sources are listed in Table 2.3. In case there is a change of hardware,

the LabVIEW software provides input interfaces for overwriting the default data logging options.

This system has analogue displays for the key engine temperatures, the speed, manifold absolute pressure and the engine torque. The coolant pressure and exhaust pressure are also displayed. Alarms have been installed to give a notification if the exhaust temperature goes above a given temperature or the low pressure fuel system goes below a given pressure. The system can shut down the engine once the exhaust temperature reaches 900°C. The load cell on the dynamometer has an output voltage which is proportional to the torque. It is then fed into the PC, via the 10x amplifier and is scaled so as to produce an accurate torque display.

Table 2.3 Default data logging options for the 4 DAQ cards

DAQ cards	Type (NI)	Sampling rate	Clock source	Trigger source
LDAQ 1	PCI-6224	1/Cycle	Dev2/PFI0	Dev2/PFI1
LDAQ 2	PCI-6224	1/Cycle	Dev3/PFI0	Dev2/PFI3
HDAQ	PCI-6250	1/CA	Dev1/PFI1	Dev1/PFI2
VDAQ	USB-6251	300 kHz	Internal clock	Dev6/PFI0

It is worth mentioning that apart from the VDAQ, the LDAQ and HDAQ use global channels created in the NI 'Measurement & Automation' for sampling data. Global channels do not contain any timing information, but they incorporate customized calibration data for converting raw voltage signals to values in physical units such as ºC, Nm, bar, etc. Test Panels in 'Measurement & Automation' also provide an easy way to test and troubleshoot the actual signals being acquired or generated by a device without programming in LabVIEW.

2.3.2 Data Acquisition System for the Single-cylinder Engine

A National Instruments™ PCI-MIO-16E-1 data acquisition card with 12-bit resolution is used for recording high frequency signals e.g. cylinder pressure, barrel pressure, inlet and exhaust pressures, triggering flags, fast FID and AFR. The sampling frequency is one sample per degree crank angle, which equals 9 kHz for a 1500 rpm engine speed. These high frequency signals are connected to a National Instruments™ BNC-2090 breakout box, which is then connected to the DAQ card.

A National Instruments™ PCI-6024E DAQ card with 12-bit resolution is used for low-speed data acquisition with a sampling rate of 100 Hz. An interface box was designed for the low-speed DAQ system for low-frequency signals comprising eight thermocouple amplifiers (for barrel, coolant, exhaust and inlet temperatures, etc.), three voltage amplifiers for torque, throttle position and RPM measurements and a frequency-to-voltage converter for the positive displacement air flow meter. Digital IIR Butterworth low pass filters were applied to all the LDAQ channels to mitigate noise associated with the actual signals. The cut-off frequency of these digital low pass filters was set to 46 Hz, which is lower than half of the sampling rate. This relationship is dictated by the Nyquist criterion, which specifies that the sampling frequency must be more than twice that of the highest frequency component of an analogue signal in order to reconstruct the actual analogue signal. 10 sample points are used for the digital filtering, and only 1 filtered value is displayed on the front panel of the LabVIEW software. Therefore, the display refreshing frequency is 10 Hz at the sampling rate of 100 Hz.

The inlet manifold pressure transducer output was amplified and sent to the High Speed Data Acquisition (HDAQ) system, the output was also sent through analogue filters with a long time constant (> 1 s, so that steady readings were obtained) before being displayed on a panel meter and being logged by the Low Speed Data Acquisition (LDAQ) system.

The 6024E features 16 channels of analogue input, two channels of analogue output, a 68-pin connector and eight lines of digital I/O, and it has three different input modes — non-referenced single-ended (NRSE), referenced single-ended (RSE), and differential (DIFF) input. In single-ended configurations, more electrostatic and magnetic noise couples into the signal connections than in DIFF configurations. Therefore, DIFF input connections should be selected in order to obtain a greater signal integrity. However, for this application, single-ended mode was adopted as it could provide sufficiently accurate values by shortening the signal leads hence reducing the risk of picking up noise. Another advantage of RSE mode over DIFF mode is that RSE provides twice the number of analogue input channels than the DIFF mode as single-ended input configurations provide up to 16 channels whilst the DIFF input configuration provides only eight channels. A channel configured in DIFF mode uses two analogue input lines: one line connects to the positive input of the programmable gain instrumentation amplifier (PGIA) of the device, and the other connects to the negative input of the PGIA. Two cards would have been used if DIFF mode had been selected.

Fig. 2.5 summarizes how to connect a floating signal source to a channel configured for RSE mode. ACH, AISENSE and AIGND represent analogue channel, analogue input sense and analogue input ground.

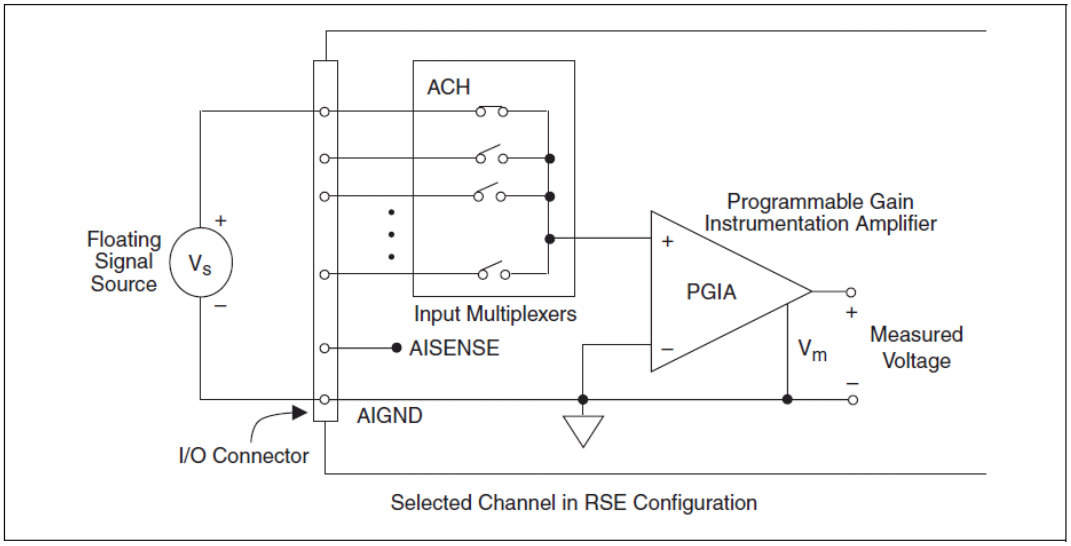

Fig. 2.5 Circuitry of single-ended input connections (http://www.ni.com)

With numerous inputs and outputs, connections would be difficult if they are directly hooked up to the card. The BNC-2090 Rack Mount acts as an interface between the DAQ card and the measuring devices. It has signal–labelled BNC connectors for the analogue inputs and outputs, and spring loaded terminal blocks for the digital and timer I/Os. Fig. 2.6 shows a photograph of the interface box.

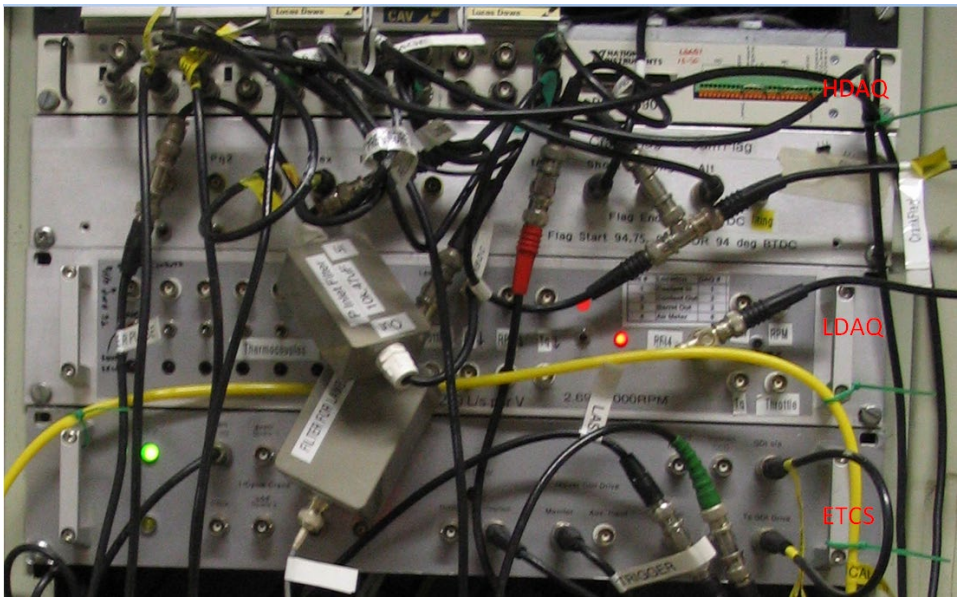

Fig. 2.6 Interface box for single-cylinder engine DAQ system

The engine is controlled by the ETCS (Engine Timing Control System) which can also communicate with the high-speed and low-speed DAQ systems via an RS-232 serial cable. These two DAQ systems used to be based in two computers, hence two serial cables were needed to communicate with the ETCS. Due to the inconvenience of synchronizing the DAQ cards, a new data acquisition program has been developed, with which the two DAQ cards can be triggered simultaneously on one computer. The CCD (Charge-Coupled Device) camera is used to capture the spray and combustion images in the cylinder. The signal routing of the current engine control and data acquisition system is depicted in Fig. 2.7.

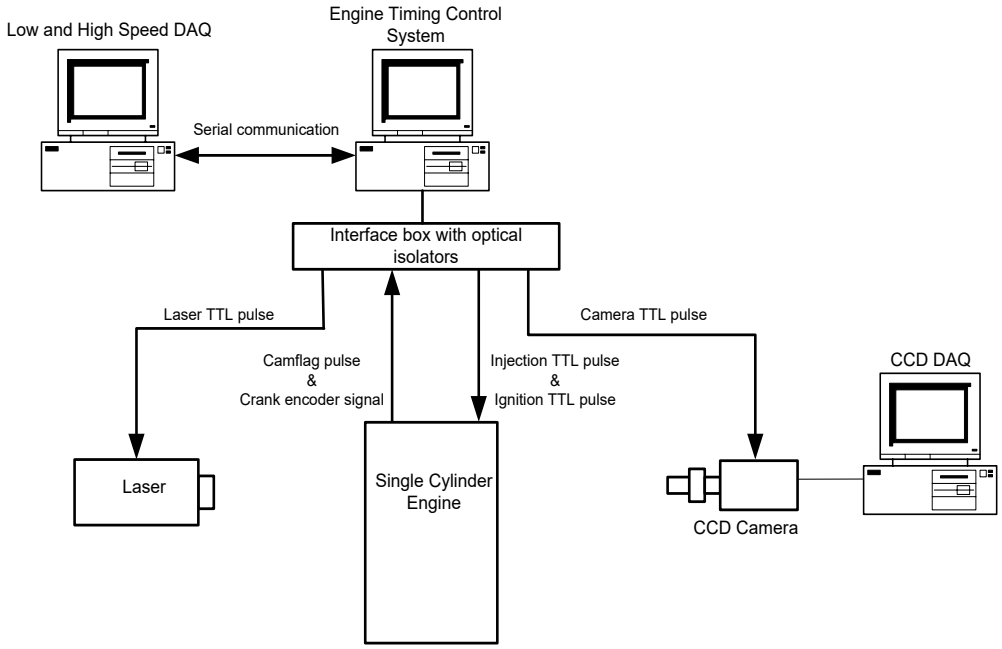

Fig. 2.7 Data acquisition system of the single-cylinder engine

The data acquisition program is similar to that for the V8 engine. However, unlike the V8, the sampling process is triggered by the ETCS and the number of sampling points and the file path under which the data will be stored are also specified on the front panel of ETCS program. During the data acquisition process, several signals from the DAQ system will also be sent back to ETCS to notify the user at which point the DAQ system is working. All these communications are realized via the RS232 serial cable. The specific communication path is shown in Fig. 2.8.

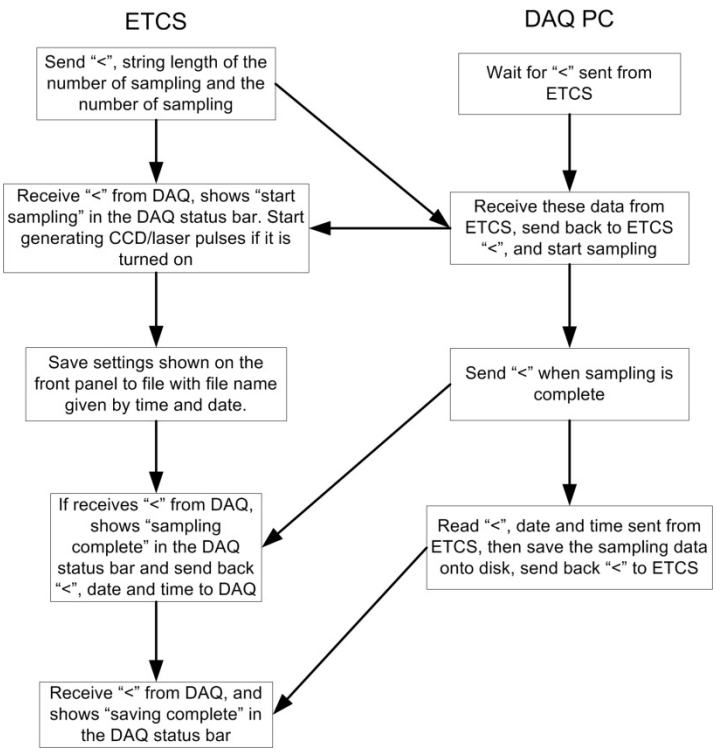

Fig. 2.8 The communication diagram for the links between ETCS and DAQ PCs

The tab structure of LabVIEW software was adopted to make the front panel look neat, as shown in Fig. 2.9. It offers the capability of choosing data logging options (channels, clock and trigger signals) for both LDAQ and HDAQ and monitoring key engine parameters just like the V8 DAQ software. In addition, the fast updated PV diagram and the instantaneous IMEP value are calculated and displayed on the front panel when the data acquisition is not triggered by the ETCS; hence it offers the possibility of monitoring the in-cylinder pressure and the PV diagram without logging any data.

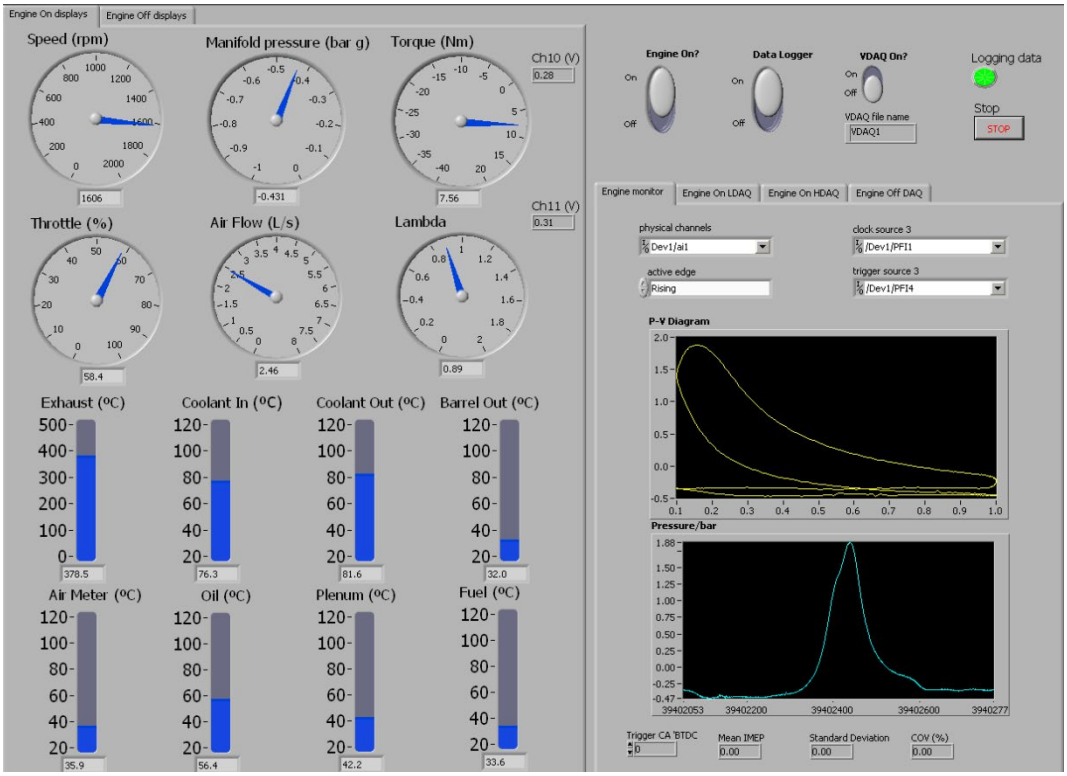

Fig. 2.9 The front panel of DAQ system for the single-cylinder engine

The DAQ software facilitates data logging without running the engine. In other words, the data is sampled using an internal clock rather than an external clock which would come from the shaft encoder. The 'Engine On displays' tab and the 'Engine Off displays' tab correspond to the external and internal clock sources respectively.

When the internal clock is selected, the 'Engine Off displays' tab is automatically switched on to display various parameters. When the ETCS sends a data logging signal, the data will be logged into the file, whose name and path has been determined by the ETCS. In this mode, the default sampling rates for LDAQ and HDAQ are 10 Hz and 1000 Hz, and the default sampling time for both cards is 10s. These parameters can be overwritten by changing the corresponding values on the 'Engine Off DAQ' tab on the right of the front panel.

When the external clock is selected, the 'Engine On displays' and 'Engine monitor' tabs are automatically switched on to display the LDAQ data, the in-cylinder pressure trace, the calculated PV diagram and IMEP. In this mode, the clock and trigger sources for the data logging are generated by the shaft encoder with the LDAQ data being sampled at once per cycle and the HDAQ data at once per crank angle degree. The default setting for the clock and trigger sources are embedded in the back diagram of the software (the code behind the graphical front panel). But they can be overwritten on the 'Engine on LDAQ' and 'Engine on HDAQ' tabs in case there is any change of pin connection.

A very high data acquisition (VDAQ) card can also be incorporated with the DAQ system for acquiring arc parameters during the very short window in which ignition occurs. The default sampling rate and crank window for the VDAQ is the same as the V8 VDAQ, namely, 300 kHz and 3900 points every cycle.

Like the V8 DAQ system, the LDAQ and HDAQ data for the single-cylinder engine were also encapsulated in global channels together with their calibration data. Therefore, the logged data are all of physical units rather than raw voltages. Both filtered and original data were logged with different postfixes in their file names.

2.4 Data Interpretation

2.4.1 DMS500 Data Processing

Most of the engine tests were conducted with the DMS500, which measures the size resolved PM number concentration and mass concentration. Its working principle was

introduced in Chapter 1. This section outlines different methodologies for processing the DMS500 number spectra and introduces a PM density model used for mass weighted calculations based on the number spectra.

Based on the raw electrometer currents, two methods have been developed by Cambustion Ltd to generate discrete number spectra and multi-lognormal spectra using different rules and with their own disadvantages and scope for error. Both spectra can be applied to the raw currents in parallel to display real time spectra. Fig. 2.10 shows the overall data processing for these two methods together with an example display of the DMS500 data.

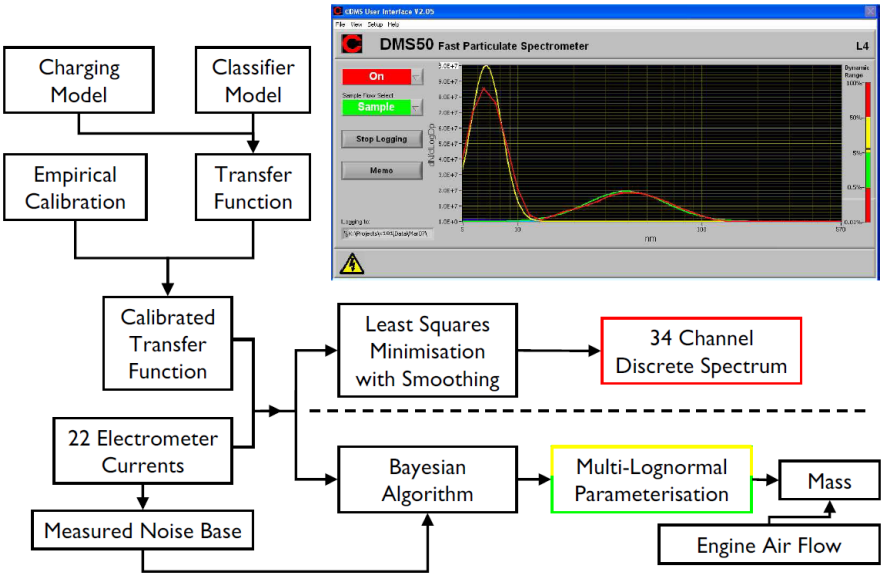

Fig. 2.10 DMS500 size spectrum processing

Cambustion Ltd bi-lognormal Fitting using a Bayesian Statistical Algorithm

Aerosol size spectra tend to consist of certain modes, each arising from separate mechanisms. As far as GDI engines are concerned, aerosol spectra tend to have two modes: a nucleation and an accumulation mode. In general, nucleation mode PM

consists of sulphate, hydrocarbon and/or water at small sizes, and accumulation mode PM at larger sizes consists of soot.

A Bayesian statistical data processing algorithm for the DMS500 has been developed, which automatically discriminates between nucleation and accumulation modes by replacing discrete number spectra with multi-mode lognormal fitting. The use of a lognormal fit has several advantages over the raw spectra, especially for the GDI engine-out aerosol which is suspected to be lognormal in nature. Firstly, it can separate the nucleation mode and accumulation mode with no sharp cut-off between these modes. As a result, even partly overlapping modes in the real aerosol can be detected and treated separately. Secondly, the lognormal fitting avoids huge overestimation of mass for large sized particles, because the mass is very sensitive to large particles and hence noise at the upper size end of a spectrum can amplify the noise on mass calculation to a large extent. By using the lognormal function, the high end noise in a spectrum will be suppressed, hence the accuracy of the mass calculation will be improved. Symonds *et al.* (2007) found that the lognormal function reduced the noise on the mass calculations by a factor of nine. Thirdly, it reduces the volume of data because the size spectrum is described by only the count median diameter (CMD), geometric standard deviation (GSD) and the number concentration for each mode. This would be useful for storing large quantities of data.

The algorithm for converting the measured DMS500 eletrometer currents to bi-lognormal spectra is briefly introduced as follows (Symonds *et al*., 2007).

The discrete or non-lognormal spectrum vector $\boldsymbol{s}$, from the measured DMS500 electrometer ring current vector $\boldsymbol{i}$, is obtained by minimizing the error term $\boldsymbol{e}$ in the following relationship:

$$\boldsymbol{i} = \boldsymbol{A}\boldsymbol{s} + \boldsymbol{e} \tag{2.1}$$

where $\boldsymbol{A}$ is a matrix representing the instrument transfer function. This is achieved by least squares minimisation as shown in Fig. 2.10 with linear regularisation and a non-negative constraint.

Replacing the spectrum with a lognormal function $\boldsymbol{I}(\mu, \sigma_{\mathrm{g}})$:

$$\boldsymbol{i} = n\boldsymbol{A}\boldsymbol{I}(\mu, \sigma_{\mathrm{g}}) + \boldsymbol{e} \tag{2.2}$$

Where μ is CMD, σ_{g} is GSD and n is the particle number concentration in the mode. A solution for μ, σ_{g} and n can be found by minimizing $\boldsymbol{e}$. For a bi-lognormal fit, Eq. (2.2) becomes:

$$i = n_1\boldsymbol{A_1}\boldsymbol{I}(\mu_1, \sigma_{\mathrm{g1}}) + n_2\boldsymbol{A_2}\boldsymbol{I}(\mu_2, \sigma_{\mathrm{g2}}) + \boldsymbol{e} \tag{2.3}$$

This allows the use of different instrument transfer functions for separate aerosol components. For example, differing aerosol charging models or calibrations can be applied to the accumulation mode than to the nucleation mode.

In practice, this optimization is performed by maximizing the posterior probability of the lognormal parameters within a Bayesian statistical framework. Bayes' theorem (Sivia, 1994) states for a set of data *D* described by parameters $\boldsymbol{w}$

$$P(\boldsymbol{w}|D) = \frac{P(\boldsymbol{w})P(D|\boldsymbol{w})}{P(D)} \tag{2.4}$$

In this case, $\boldsymbol{w}$ are the lognormal parameters n_{m}, μ_{m} and σ_{gm} (m = 1, 2) and the data are the measured electrometer currents *i*. P($\boldsymbol{w}$|*D*) is the posterior probability to be maximized. P(*D*|$\boldsymbol{w}$) is known as the likelihood and represents the probability of the measured electrometer currents given a set of parameters. P(*D*) is a normalisation constant that can be ignored. A set of electrometer currents $\boldsymbol{j}$ can be obtained from a set of parameters $\boldsymbol{w}$ by means of

$$\boldsymbol{j}(\boldsymbol{w}) = \boldsymbol{A}\boldsymbol{s}(\boldsymbol{w}) \tag{2.5}$$

For each electrometer, the probability of the measured electrometer current *i*, given the guessed electrometer current *j* are correct, is assumed to be normally distributed with a standard deviation equal to the instrument noise on that electrometer, σ:

$$P(i|j,\sigma) = \frac{1}{\sigma\sqrt{2\pi}}\exp\left(-\frac{(i-j)^2}{2\sigma^2}\right) \tag{2.6}$$

As the noise on each electrometer can be assumed to be independent, the total likelihood is given as

$$P(D|\boldsymbol{w}) = \prod_{k=1}^{22} \frac{1}{\sigma_k\sqrt{2\pi}} \exp\left(-\frac{(i_k - j_k(\mathbf{w}))^2}{2{\sigma_k}^2}\right) \quad (2.7)$$

The term P($\boldsymbol{w}$) in Eq. (2.4) is known as the prior probability. It represents the prior knowledge about a system before the data is examined. For a GDI aerosol, this is used to constrain and separate the nucleation and accumulation modes. Fig. 2.11 shows an example probability map for a diesel combustion aerosol.

The figure originally located here has been removed from this version of the thesis for copyright reasons.

Fig. 2.11 *Example prior probability map for diesel aerosol (Symonds et al., 2007)*

Such a map is contained within a configuration file specific to a type of aerosol and a particular instrument's calibration. In this project, an inversion matrix file labelled 'Diesel_M16_m2cq70.dmd' has been used to give a good approximation for both PM modes of a GDI aerosol.

Bi-lognormal fitting using Matlab least squares error algorithm

It is worth noting that both the lognormal and discrete inversions are best fits to the currents, just using different rules to best represent the instrument's raw response to the aerosol. Occasionally, the lognormal spectra are rather different from the discrete spectra. For example, there are clear bi-normal characteristics on the discrete spectra but the lognormal functions do not exhibit the nucleation mode as expected. Therefore, the author used the multi-variable optimization function in Matlab to fit a mixture of two log-normal distributions to the discrete spectra based on the least error square algorithm.

The discrete spectrum is fitted by a combined probability density function (PDF) which is a weighted sum of the PDFs of two log-normal distributions. The function takes 6 inputs: a vector of data at which to evaluate the PDF, in this case, the DMS500 discrete spectrum, and the distributions' five parameters. Each normal distribution has parameters for its mean and standard deviation; the combination probability makes a total of five. The combined PDF can be expressed as:

$$PDF = p \cdot pdf(X, mu_1, sigma_1) + (1 - p) \cdot pdf(X, mu_2, sigma_2) \qquad (2.8)$$

Where p is the combination probability for the 1st component, in this case, nucleation mode; X is the vector of data at which the fitting is based on, in this case, the DMS discrete spectrum; mu_1 and $sigma_1$ are the mean size and standard deviation for the nucleation mode fitting whilst mu_2 and $sigma_2$ are for the accumulation mode fitting.

A multi-variable optimization is then conducted in Matlab to best represent the discrete spectrum *X* using the combined PDF function based on the least squares error algorithm. Because it has 6 input parameters, the optimization process can be quite sensitive to the initial guess. In order to obtain the final solution within reasonable iteration times, i.e. computing time and to avoid divergence, a trial and error method has been used to determine a satisfactory initial guess for the optimization process. It turns out that it will converge to a global optimization solution for most cases when the initial inputs are p = 0.5, mu_1 = 25 (nm), $sigma_1$ = 5 (nm), mu_2 = 80 (nm), $sigma_2$ = 5 (nm).

Fig. 2.12 shows a comparison between this least squares error fitting and the Cambustion Ltd bi-lognormal fitting on a same PM sample.

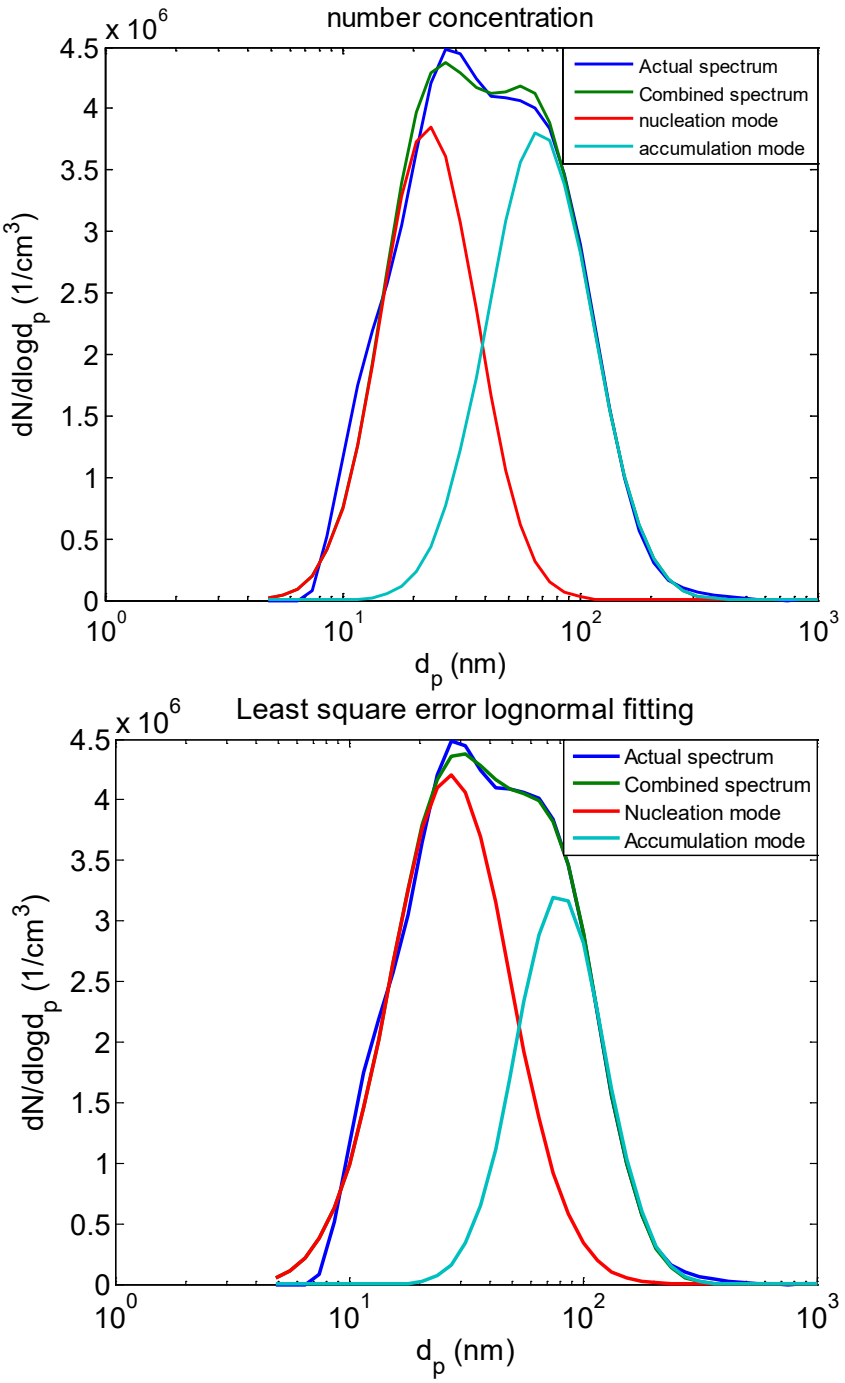

Fig. 2.12 *Comparison between the Cambustion Ltd Bayesian lognormal fitting (above) and the Matlab least squares error fitting (below) on an identical PM sample*

From Fig. 2.12, it can be seen that the Matlab least squares error fitting produces an even better approximation to the discrete spectrum than the log-normal fitting using the Bayesian statistical algorithm. The main advantage of the Cambustion Ltd

lognormal fitting on the raw currents is that it allows consideration of the base electrical noise of the instrument in determining if a mode is statistically significant or not. The Cambustion Ltd lognormal fitting also allows real time display of the two modes, which is good enough for most cases. However, the Matlab least squares error fitting code offers the capability of discriminating between the nucleation and accumulation modes when the Cambustion Ltd lognormal fitting produces unexpected results.

The DMS500 spectra can exhibit spikes in the region of around 5-20 nm occasionally, which may well obscure the ensemble average results. If the spikes occur, the sub-23 nm data need to be truncated to avoid over-estimation of particle number. This method works as a 'digital' volatile particle remover, which is consistent with the test procedure proposed by the EU PMP program (European Union Particle Measurement Programme).

Conversion from PM number to PM mass

Both the lognormal and discrete spectra are prone to artefacts, and occasional spikes can be produced on the spectra which easily obscure the ensemble-averaged results. This is particularly true in the region of sub-23 nm where singly charged particles may become doubly charged. In addition, the DMS500 instrument noise base in this region is always higher than at large sizes. Therefore, sub-23 nm data were deliberately truncated from the discrete spectra when the spike level becomes unacceptable. This is also in agreement of test procedure proposed by EU PMP program, which specifies that a volatile particle remover is used as shown in Fig. 2.13.

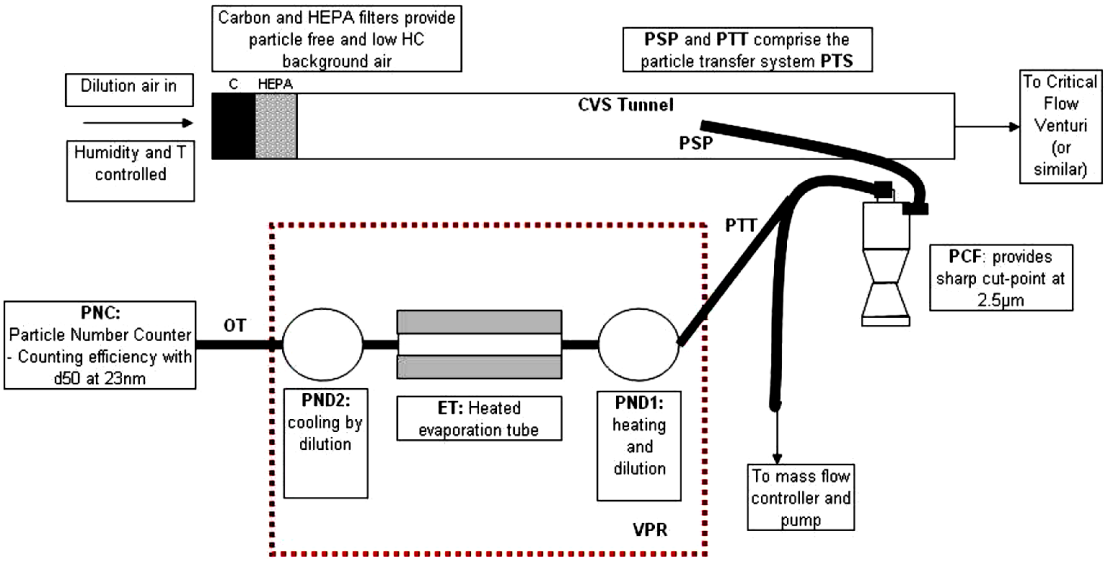

Fig. 2.13 *Schematic of recommended particle sampling system (E/ECE/324 E/ECE/TRANS/505 Regulation No. 83,Ford internal report, 2009)*

Data above 700 nm particle size were also truncated from the discrete spectra due to the fact that the number concentration in this region is low and comparable to the noise level in the instrument.

In order to convert number concentrations to mass concentrations, a PM density model was used:

$$\mathrm{M\ (kg)} = 1.72 \times 10^{-24} \times {D_\mathrm{p}}^{2.65}\mathrm{(nm)} \tag{2.9}$$

This equation had been experimentally determined using the Couette CPMA (Centrifugal Particle Mass Analyser) on the same V8 engine (Symonds *et al.,* 2008). The Couette CMPA had previously been used to measure the density of diesel engine particles (Olfert *et al*., 2007).

The fractal dimension, D_f, such that mass is proportional to diameter^{Df}, for diesel PM was determined to be 2.20–2.48 for regular loads. The increased fractal dimension observed in the V8 SGDI engine compared with diesel engines is possibly related to the difference in the ratio of organic to elemental carbon. This equation was determined at a certain engine condition. In other words, this PM density model may not be universally applicable and hence the mass data should be used with caution. It is thus important to know the characteristics of PM emissions from SGDI engines on a number basis.

The total Particle number (Pn) and total Particle mass (Pm) can be calculated by numerically integrating the PM size distributions and the derived mass distributions respectively.

2.4.2 Analysis of Combustion Performance

Combustion performance data such as IMEP and MFB (Mass Fraction Burned) are derived from in-cylinder pressure data. For both the V8 and the single-cylinder engine, water-cooled Kistler pressure transducers mounted in the cylinder head are used together with their charge amplifiers to measure in-cylinder pressure.

The pressure transducers are normally subject to thermal drift and drift can also be introduced by the charge amplifier. Therefore, it is necessary to reference the in-cylinder pressure to a known absolute pressure. This reference pressure can be selected in different ways. For instance, it can be the inlet manifold pressure at the inlet bottom dead centre (IBDC), which is the case for the 4 pressure transducers in the V8 engine; or the atmospheric pressure at the exhaust top dead centre (ETDC)

assuming that the in-cylinder pressure and the exhaust manifold pressure have equalised by the end of the exhaust stroke. These two methods could introduce errors due to the pulsation of the inlet manifold pressure or the exhaust manifold pressure.

To avoid these errors in the optical engine, the reference pressure for correcting the in-cylinder pressure was obtained from a barrel pressure transducer. The barrel pressure transducer is mounted in the bottom of the barrel so that it can measure in-cylinder pressure when the piston is near BDC whilst the atmospheric pressure when the piston is near TDC. Therefore, the atmospheric pressure can be used to correct the barrel transducer around TDC which then provides an identical pressure with the in-cylinder pressure transducer around BDC.

Already developed in-house Matlab software CoBRA enables the aforementioned correction to the in-cylinder pressure data. The detailed description of CoBRA can be found elsewhere in the literature (Ma, 2006). It can also calculate the following combustion data based on the corrected in-cylinder pressure:

- Peak pressure and the crank angle at which peak pressure occurs
- Rate of pressure rise
- Net and gross IMEP
- Mass fraction burned (MFB)

Fig. 2.14 shows typical in-cylinder pressure traces and MFB traces for 70 cycles of data.

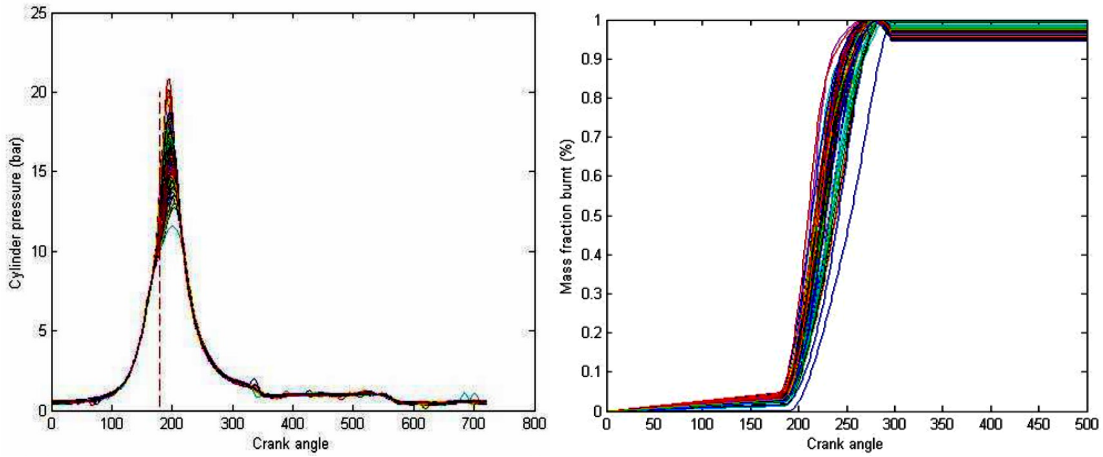

Fig. 2.14 *Cylinder pressure trace and mass fraction burnt curves for 70 cycles (Operating condition: 1500 rpm, 0.5 bar MAP and ignition time of 35° CA BTDC)*

CoBRA requires a data file with at least two columns of data, i.e. the in-cylinder pressure and the flag data. Barrel pressure data is also useful for providing an absolute datum for the transducer. The raw pressure data are then split into cyclic columns in order to analyze the data on a cycle-by-cycle basis. This is done by synchronizing the pressure data and the flag pulse, which has a known crank angle, e.g. BDC. Finally, the combustion performance data can be obtained from the in-cylinder pressure data.

The method used to calculate the mass fraction burned (MFB) was first developed by Rassweiler and Withrow (Rassweiler and Withrow, 1938). In this method, the combustion process was approximated by considering a series of small crank angle intervals ($\Delta\theta$), during each of which the change in pressure (Δp) is the sum of two parts: the pressure rise due to piston motion (Δp_v), and the pressure rise due to combustion (Δp_c).

$$\Delta p = \Delta p_v + \Delta p_c \tag{2.10}$$

The concept is shown graphically in Fig. 2.15.

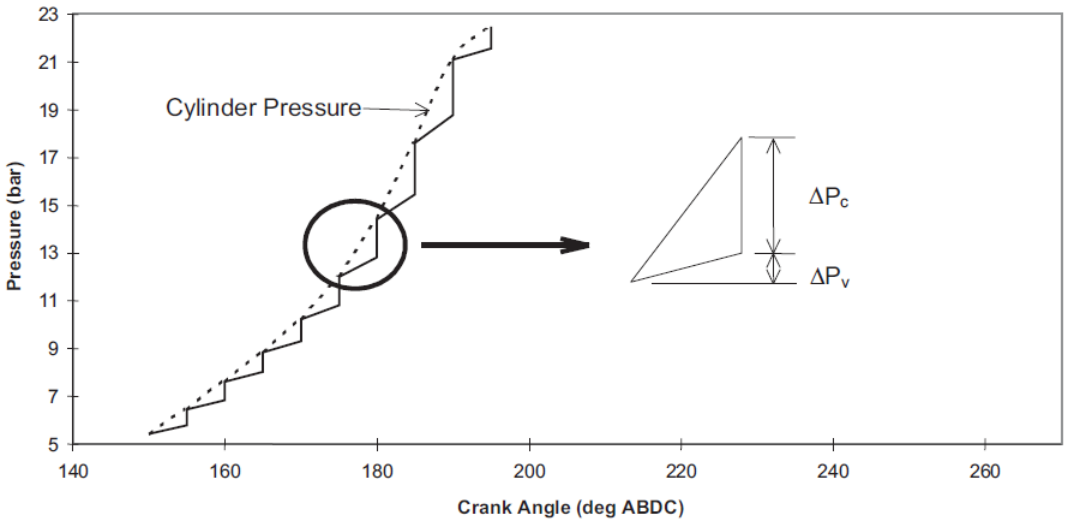

Fig. 2.15 *Measured pressure change as a sum of piston motion and combustion (Stone, 1999)*

The charge is compressed polytropically by the piston, then a small amount of charge burns causing a pressure rise. In the next crank angle interval, the pressure again changes polytropically and another bit of charge burns, and this continues throughout the combustion period.

At the ith step, assume the pressure p_i and the volume V_i is known, the pressure at the next step $p_{\mathrm{v,i+1}}$ can be calculated by assuming an polytropic process with an index n:

$$p_{\mathrm{v,i+1}} \cdot {V_{\mathrm{i+1}}}^n = p_\mathrm{i} \cdot {V_\mathrm{i}}^n \tag{2.11}$$

So the pressure rise due to compression can be calculated by

$$\Delta p_{\mathrm{v,i}} = p_{\mathrm{v,i+1}} - p_\mathrm{i} = p_\mathrm{i}\left[\left(\frac{V_\mathrm{i}}{V_{\mathrm{i+1}}}\right)^n - 1\right] \tag{2.12}$$

By using equation 2.10 and 2.11, the pressure rise due to combustion is:

$$\Delta p_{c,i} = p_{i+1} - p_i(\frac{V_i}{V_{i+1}})^n \tag{2.13}$$

Since combustion is not taking place at constant volume, equation 2.4 must be normalized to some reference volume, e.g. the cylinder volume at TDC. The assumption of this normalisation is that the pressure rise is inversely proportional to the volume.

The normalized pressure change is denoted by Δp_c^*:

$$\Delta p_c^* = \Delta p_c \frac{V_i}{V_{TDC}} \tag{2.14}$$

The end of combustion occurs when the pressure rise due to combustion becomes zero. Assuming that the normalised pressure rise is proportional to the MFB *x*, then for *N* total increments:

$$x = \frac{\sum_0^i \Delta p_c^*}{\sum_0^N \Delta p_c^*} \tag{2.15}$$

Although the heat transfer and change in composition are not taken into account, the MFB results calculated using this method showed a remarkably close agreement with the results obtained from other more complex thermodynamic models (Brunt and Emtage, 1997).

2.5 Summary

Two engines have been used for this research: a Jaguar V8 AJ133 engine and a Jaguar single-cylinder optical access engine. Details of the engine specifications and the experimental arrangement in the engine test cell have been presented.

Two LabVIEW-based data acquisition programs have been developed for recording various engine parameters at low sampling rate (1/cycle), high sampling rate (1/ºCA) and very high sampling rate (300 kHz). The DAQ system for the single-cylinder engine also facilitates the communication with the ETCS system, i.e. the engine timing control system via a RS232 serial cable to enable synchronization between data logging and camera or laser triggering.

Data interpretation of the DMS500 data has been discussed with a brief description of algorithms behind the conversion from the raw electrometer currents to the discrete spectra and bi-lognormal fitting for number spectra. A Matlab code has been developed by the author for bi-lognormal fitting based on the discrete spectrum, and it has been proven to be a useful alternative way for discriminating the nucleation mode and the accumulation mode. A PM density model is used to convert PM number to PM mass.

An in-house developed Matlab software CoBRA can calculate various combustion performance data (e.g. IMEP, MFB) based on the corrected in-cylinder pressure. The method used to calculate the MFB in CoBRA has been briefly discussed.

3. Automatic Dilution System

3.1 Introduction

Apart from size distributions, composition and surface area of PM are also of particular importance in the light of recently published studies on the environmental and health effects of ultra-fine particulate matter. In order for these parameters to be obtained in a compliant way, an automatic PID-controlled dilution system is designed to provide control over critical dilution profiles, such as dilution ratio, dilution temperature and filter face velocity for filter sampling. As far as PM number-based measurement is concerned, the dilution ratio and dilution air conditions can also have a great influence on PM measurement results (Kittelson *et al.* 1999, Luders *et al.* 1998, Mathis *et al.* 2004, Lipsky and Robinson 2006), therefore, the system can also be used in conjunction with other instruments such as the DMS500 to achieve higher reliability and repeatability of PM measurements.

Once an exhaust sample is extracted, dilution is required for the following reasons:

- Dilution can be used to prevent water condensation inside instruments which could cause measurement errors or even damage to instruments like mass flow meters;
- PM measuring instruments (e.g. DMS500) might suffer concentration saturation or severe contamination when a highly sooty source is measured such as a burner. Dilution can reduce the concentration into the measurable range;

- Dilution reduces the PM concentration. Consequently, the rate of coagulation is reduced. With sufficient dilution, the PM number concentration and size distribution may be considered frozen, and so the effect of sample residence time is reduced (Price, 2009).

There is substantial evidence to support the viewpoint that the dilution ratio and the sampling temperature can have dramatic effects on particle size and number concentration measurements. Luders et al. published a measured size distribution with no nucleation mode when the dilution air temperature was 35 ºC. However, a nucleation mode was seen in the same experiment when the dilution air temperature was reduced to 20 ºC. Luders *et al.* (1998) even suggested that inadequately adjusted dilution parameters (especially dilution ratio and dilution air temperature) can actually provoke the formation of ultra-fine particles by condensation.

This chapter is devoted to a detailed description of the dilution system in terms of the graphical user interface, the control algorithm and hardware configuration. An interface box was made in the Department of Engineering Science at Oxford which facilitates the communication of various sensors and a NI USB-6008 data acquisition card, followed by an example of its application in V8 engine experiments.

3.2 Dilution System Overview

The Dilution system has been successfully implemented to undertake various engine experiments. It consists of a National Instruments^{TM} USB-6008 card, 2 thermocouples, 2 mass flow meters, an electric heater and an interface box. A typical application of the dilution system together with the DMS500 is illustrated in Fig. 3.1.

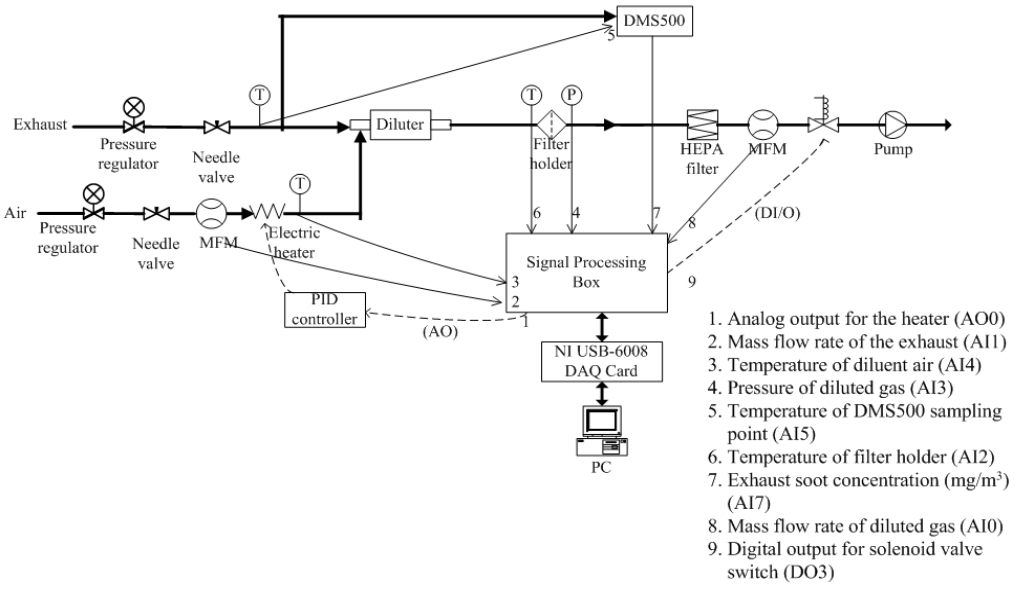

Fig. 3.1 The layout of the automatic dilution system used in conjunction with the DMS500

As shown in Fig. 3.1, engine-out exhaust or any PM-containing aerosol (e.g. aerosol from a burner) is diluted by heated diluent air in a concentric dilutor. The diluted gas then flows through a Whatman^{TM} 47mm GF/A glass fibre filter held in a stainless steel filter holder where the majority of the particulate emissions in the diluted aerosol are captured. The remaining gas will go through a HEPA filter and be measured by a Honeywell AWM720 mass flow meter with a capability of 200 L/min before eventually being expelled out through laboratory ventilation. Both exhaust and diluent air flow are enabled by the suction of a pump of around 60 L/min in capacity.

There are 7 analogue inputs with this dilution system, namely, the mass flow rate of the diluent air, the temperature of the heated air, the temperature of the DMS500 sampling point, the temperature of the filter holder, the pressure of the diluted gas, DMS500 soot concentration and the mass flow rate of the diluted gas. The temperature of the DMS500 sampling point is monitored and logged into the DMS data files via one of its analogue input channels because it is more relevant to

DMS500 measurement than to the dilution control system. All the other 6 signals are logged into the NI USB-6008 card after being converted to a readable 0-10V voltage signal by the signal processing box, or the interface box. The LabVIEW software on the PC applies IIR Butterwoth low pass filter virtual instruments to all these analogue inputs to eliminate glitches associated with the actual signals. There is one analogue output for controlling the electric heater and one digital output for controlling a solenoid valve that acts as a switch for the flow as shown in the above Fig. 3.1.

The EPA (Environmental Protection Agency) in the U.S. and the EU counterpart used to define the diluted gas temperature within 20 cm upstream or downstream of the filter face for PM mass measurements to be less or equal to 52 ºC. Having recognized the significant influence of the filter temperature on PM emissions results, EPA adjusted the definition of the filter temperature by narrowing it from below 52 ºC to a region of 47 °C ± 5 °C which aims to improve the repeatability of PM mass measurements (Khalek, 2006). Therefore, a LabVIEW PID control toolkit has been employed to maintain the target value of 47 ºC for the filter face temperature by adjusting the heater actuating voltage, hence the temperature of the heated diluent air. The actual temperature of filter is registered by a thermocouple and logged into the NI USB-6008 card. If this actual temperature is below 47 ºC, the PID controller will detect the difference and calculate a desired voltage based on this difference and the rising rate of the actual temperature. This desired voltage is then sent into a solid state power regulator to pull up the power to actuate the heater. A detailed description of this PID control algorithm is given in Section 3.5.

Another stringently regulated parameter in terms of filter-based sampling system is the filter face velocity, i.e. the velocity of aerosol passing the filter. Under the E/ECE/324 Regulation No 83, the filter face velocity should be set to a single value within the range of 20 to 80 cm/s whilst the value is within 0-100 cm/s under EPA regulation. Narrowing the filter face velocity window may lead to better lab-to-lab variability, hence the 20 - 80 cm/s is used in this system as a limitation. The system will generate a warning signal whenever the calculated face velocity is outside this range. Previous work indicated that the filtration efficiency of particles remains higher than 96 percent across the filter face for velocities likely to be used in engine tests of up to 130 cm/s (Khalek, 2006), therefore a higher filter face velocity would be preferable for the sake of saving sampling time. The filter face velocity can be estimated by the following equation assuming the density of exhaust is the same as that of air under the same condition:

$$V_{\text{filter}} = \frac{\dot{V}_{\text{dil}}}{A_{\text{pipe}}} = \frac{\dot{m}_{\text{dil}}/\rho_{\text{dil}}}{A_{\text{pipe}}} = \frac{\dot{m}_{\text{dil}}}{\frac{\overline{p}_{\text{dil}}}{(R_{\text{exh}} \cdot T_{\text{exh}})}} \approx \frac{\dot{m}_{\text{dil}}}{\frac{\overline{p}_{\text{dil}}}{(R_{\text{air}} \cdot T_{\text{exh}})}} \quad (3.1)$$

Among others, the dilution ratio (*DR*) is another important dilution parameter that could significantly affect the PM emission results. The *DR* is calculated by measuring the mass flow rate of the diluent air and the diluted gas using the following formula:

$$DR = \frac{\dot{m}_{\text{air}}}{\dot{m}_{\text{exh}}} = \frac{\dot{m}_{\text{air}}}{\dot{m}_{\text{dil}} - \dot{m}_{\text{air}}} \quad (3.2)$$

$\dot{m}_{air}$, $\dot{m}_{exh}$ and $\dot{m}_{dil}$ represent the mass flow rate of the diluent air, exhaust and diluted gas respectively.

The dilution ratio is chosen to be 5 for most experiments as a balanced value due to the fact that a larger dilution ratio will lengthen the sample time for collecting enough particulate emissions on the filter for further analysis such as TGA, whilst a smaller dilution ratio could foster water condensation in the dilution system, which can spoil the mass flow meter. By adjusting the needle valves on both exhaust and diluent air side, the dilution ratio can be varied from 0 to +∞.

In order to get an estimation of the time needed to collect a given amount of particulate emissions on the filter, an analogue output of DMS500 representing the particulate concentration [P] in the exhaust (mg/m^3) is fed into the NI USB-6008 card. The particulate loading rate of the filter $\dot{m}_{\mathrm{P}}$ can then be estimated by the following equation assuming the density of exhaust is the same as that of air under the current condition:

$$\dot{m}_{\mathrm{P}} = [P] \times \dot{V}_{\mathrm{exh}} = [P] \times \frac{\dot{m}_{\mathrm{exh}}}{\rho_{\mathrm{exh}}} = [P] \times \frac{\dot{m}_{\mathrm{air}}/DR}{p_{\mathrm{dil}}/(R_{\mathrm{exh}} \cdot T_{\mathrm{exh}})} \approx [P] \times \frac{\dot{m}_{\mathrm{air}}/DR}{p_{\mathrm{dil}}/(R_{\mathrm{air}} \cdot T_{\mathrm{exh}})} \quad (3.3)$$

The particulate loading rate of the filter is calculated and displayed on the front panel of the LabVIEW software at a frequency of 1 Hz. The total time of collecting a given amount of PM can then be calculated accordingly. But in practice, the low particulate concentration of engine-out exhaust and the low suction of the pump could easily make the calculated sample time for collecting 1 mg PM more than a day. 1 mg is a desired value for TGA analysis. Instead, a sample time of 20 minutes was chosen for all runs so as to get visibly dark filters.

As mentioned already, the electric heater voltage is under real-time PID control to maintain the temperature of the filter holder around its target value, i.e. 47 ºC. Some safety issues have been taken into account in terms of controlling the heater voltage in the LabVIEW software. One is that the heater has to be turned off if the diluent air flow rate is lower than 0.02 g s^{-1}, as this will prevent heating stagnant gas. The second issue is that if the temperature of heated diluent air is above 350 ºC, the heater voltage will be forced to zero to protect the sampling pipe and the dilutor. Last but not least, the heater has to be turned off before terminating the LabVIEW software, otherwise the heater could work unattended and its lifetime could be compromised. All these safety constraints are set above the PID controller, in other words, the heater voltage will be forced to zero when those critical conditions are met independent of the actual output of the PID controller.

3.3 NI Data Acquisition Card and Interface Box

3.3.1 NI data acquisition card

The core part of the dilution system is the NI USB-6008 card which provides connection to eight analogue input (AI) channels, two analogue output (AO) channels, 12 digital input/output (DIO) channels, and a 32-bit counter with a 2.0 USB interface to a PC. The card is configurable to facilitate two analogue input modes: Differential mode and Reference Single-Ended (RSE) mode. The differential mode can measure ±20V signals and use the variable-gain amplifier. However it can only measure 4 AI signals because it requires signal pairs of positive and negative terminal for each signal. Therefore a RSE mode is used by connecting each positive voltage signal to a

desired AI terminal and all the ground signals to a common GND terminal, as illustrated in Fig. 3.2.

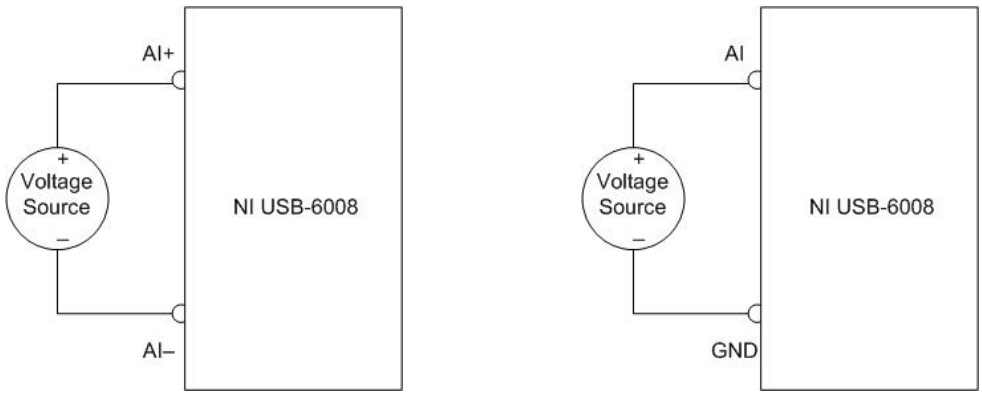

(a) Connection of Differential mode *(b) Connection of RSE mode*

Fig. 3.2 Signal connection of two analog input modes

The 8 single-ended analogue inputs have a resolution of 11 bits and a sampling rate of up to 10 kS/s. Fig. 3.3 illustrates the analogue input circuitry of the NI USB-6008 card.

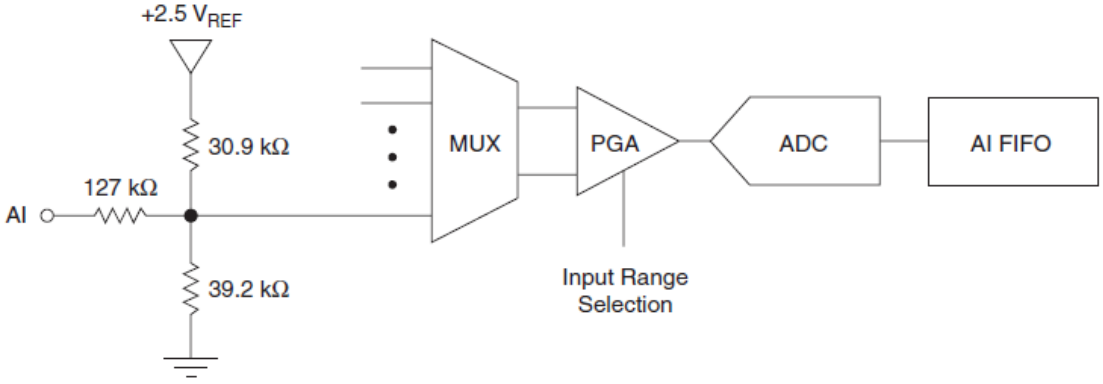

Fig. 3.3 Analogue input circuitry of USB-6008

MUX refers to multiplexer which routes one AI channel at a time to the PGA (Programmable-Gain Amplifier) that provides a unity gain when configured for reference single-ended measurements. The analogue-to-digital converter (ADC)

digitizes the AI signal by converting the analogue voltage into a digital code. A first-in-first-out (FIFO) buffer restores data temporarily during AI acquisition to ensure that no data is lost when a finite number of samples are recorded.

In practice, however, the LabVIEW software often encounters a buffer overflow error, especially when the data needs to be logged to a file that is selected from an Open File Dialog, because measurements will start filling up the buffer between the time that the LabVIEW 'DAQmx Start Task' VI (Virtual Instrument) executes and when the first 'DAQmx Read' executes. For continuous data acquisition mode, 'DAQmx Read' is normally placed in a while loop whilst the 'Open File' VI and the 'DAQmx Start' VI are normally placed outside the loop, which means that the first data reading occurs only after a file has been chosen. If the time in choosing a file is too long, then the buffer will be completely filled up and the initial data will be overwritten before the DAQmx Read VI takes it out of the buffer. Two commonly adopted solutions include increasing the buffer size and decreasing the sampling rate. Another remedy is to use error wires to force the execution sequence of different Vis, such that measurements will not begin filling up the buffer until after a file has been selected. This remedy is adopted in the LabVIEW software controlling this dilution system.

Another common problem causing the buffer error is the mis-match of data input and output rate of the buffer. Buffer overflow errors occur when data is written to the buffer faster than it is read. Buffer underflow errors occur when data is taken from the buffer faster than new data is added. In order to avoid either of these, a general rule of thumb is to acquire around 1/10th of a second of data. For example, for a sample rate of 100 Hz, set the number of samples to read to 10 within the while loop. This

dilution system has the sample rate of 100Hz and 10 samples per channel within each iteration of the while loop. The signal processing such as filtering and rolling averaging is done based on the 10 samples for each channel.

The NI USB-6008 card has two independent analogue output channels AO0, AO1 that can generate outputs from 0-5V. In the dilution system, AO0 is used to provide a 0-5V signal which represents the controlled heater voltage. This signal is amplified by a solid state power regulator to actuate the heater. The analogue output circuitry for the NI USB-6008 is shown in Fig. 3.4.

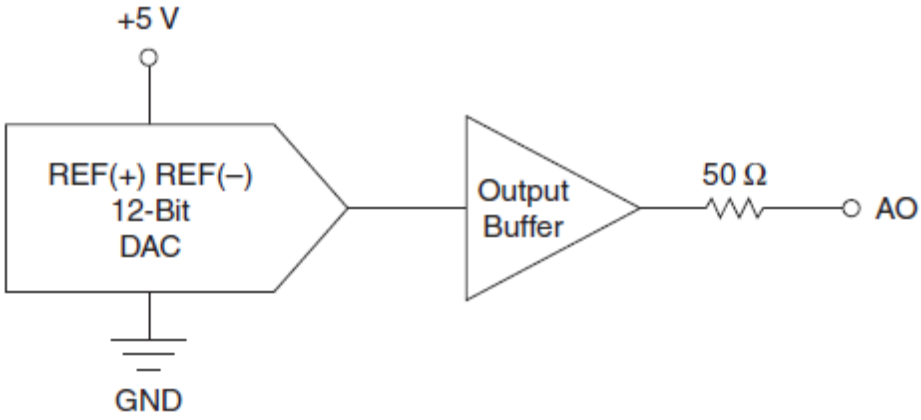

Fig. 3.4 Analogue output circuitry of USB-6008

Digital-to-analogue converts (DACs) convert digital codes to analogue voltages. The output buffer holds the data to ensure that no data is lost when a finite number of samples are sent out. The output buffer could experience both overflow and underflow errors just like the analogue input buffer. Another issue is that the DAC produces glitches from time to time due to released charge. This is frequently the case when the most significant bit of the DAC code changes. In this application, glitches

are rarely found because there is no abrupt change in heater voltage value as long as the PID controller is working properly.

The NI USB-6008 card has 12 digital lines, P0.<0..7> and P1.<0..3>, which comprise the DIO (Digital Output) port. GND is the ground-reference signal for the DIO port. In this dilution system, only one line is configured to drive the solenoid valve which controls the flow through the filter.

3.3.2 Interface Box

In order to read the signals from various sensors, such as thermocouples and pressure transducers, an interface box was devised as a signal conditioning unit to produce appropriate signals required by the NI USB-6008 card. It also integrates a solid state power regulator and an optical isolator to pull up the power of analogue output and digital output from the DAQ card to drive corresponding electric components, namely, the heater and the solenoid valve. The back panel of the interface box is shown in Fig. 3.5.

Fig. 3.5 Back panel of the interface box

It consists of assorted signal input interfaces for thermocouples, mass flow meters, pressure transducers and soot concentration. The signal from the thermocouples was amplified by an AD595 thermocouple amplifier, but because of the low impedance of the DAQ card a buffer amplifier (TL081CN) was also needed. The power socket sends out the amplified analogue output voltage to control the electric dilution air heater. A BNC connector adjacent to the socket allows an extra check of the actual heater voltage by using a voltmeter. The digital output sent out by the DAQ card goes through an optical isolator to get an appropriate signal to drive the solenoid valve controlling the dilution gas flow. Optical isolators used in this integrated circuit (ISQ74) aim to prevent any direct electrical transmission between the DAQ card and the solenoid valve. The 'optical isolator' is illustrated in Fig. 3.6.

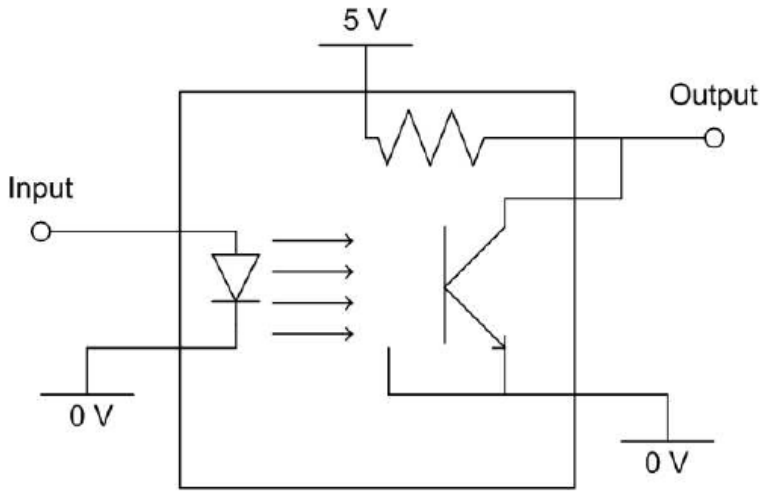

Fig. 3.6 The physical structure of an optical isolator

An optical isolator consists of an LED and a photo-transistor. The phototransistor will turn on if the LED is excited by an input current. The only connection between the LED and the phototransistor is through light, not electricity. Hence it could reduce the

risk of damaging the DAQ card. Table 3.1 summaries the signal connections between the DAQ card and the interface box and the signal conditioning.

Table 3.1 Signal connections between the DAQ card and the interface box

Signal name	DAQ Channel	DAQ pin	Labels on the interface box	Signal Conditioning?
Heater output	AO0	14	Heater 0-5V	Solid state voltage regulator
Mass flow rate of the exhaust	AI1	5	MFM DIL	No
Temperature of diluent air	AI 4	3	T_{heater} (T1)	On-board thermocouple amplifier
Pressure of diluted gas	AI 3	11	P_{dil}	Amplifier
Temperature of DMS500 sampling point	AI1*	-	-	External thermocouple amplifier
Temperature of filter holder	AI 2	8	T_{filter} (T2)	On-board thermocouple amplifier
Exhaust soot concentration	AI 7	12	mg/m^3	No
Mass flow rate of diluted gas	AI 0	2	MFM AIR	No
Digital output for solenoid valve	DO 3	20	SV_{ex}	Optical isolator
Ground	GND	1	-	No

**Analogue input 1 of DMS500*

3.4 Graphical User Interface of the Dilution System

Fig. 3.7 shows the graphical user interface of the dilution system under a typical test condition.

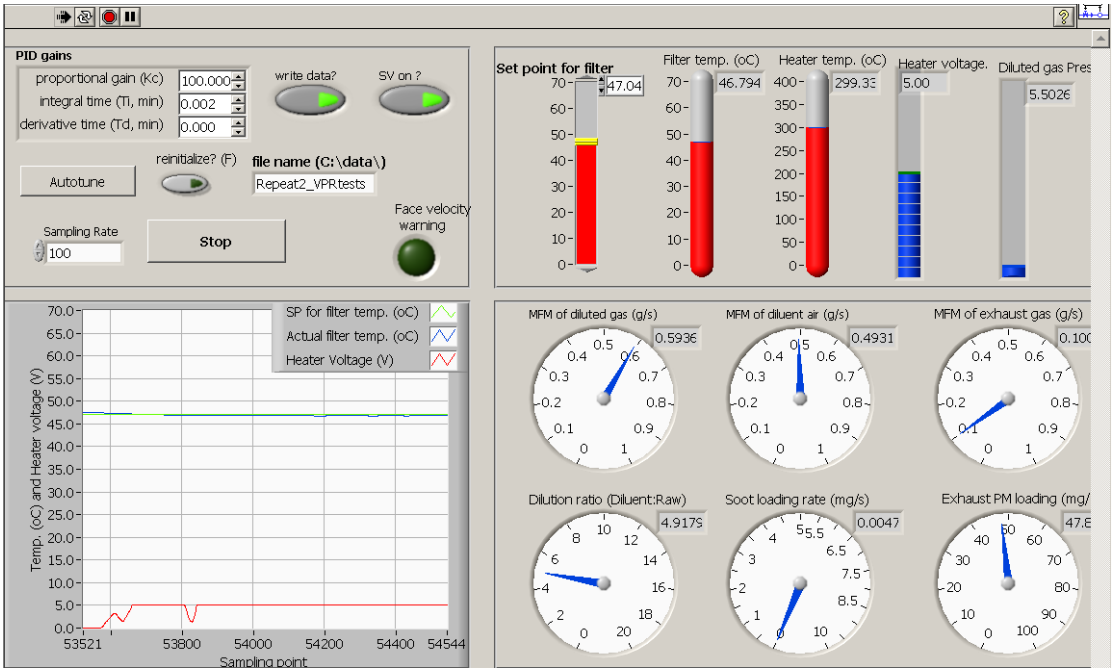

Fig. 3.7 Graphical user interface of the dilution system

The right part of the front panel consists of displays for various parameters such as MFMs, temperatures whilst the left part shows the performance of the PID controller which is committed to maintain the temperature of the filter holder.

On the left of the above front panel, the target value for the filter holder is set to be 47 ºC. Other parameters, such as mass flow rates of diluted gas and dilution air and the actual temperatures of the filter holder and the heater outlet, are monitored in real-time and are logged into the PC when the 'write data?' button is pressed. The definitions of these parameters have already been introduced in Section 3.2.

The default sampling rate of all these analogue inputs is 100 Hz and Butterworth IIR low-pass filters are applied to them to abate noise or glitches associated with the actual signals. In addition to these digital filters, rolling average values are calculated based on 10 sample points for individual signals to further smooth them. One of 10

averaged values is used and displayed on the front panel for each signal. Therefore, the refreshing rate for these displays is 10 Hz. Rolling average values can be calculated using the following equation:

$$Y_i = \begin{cases} \frac{\sum_1^i X_i}{i}, & i = 1,2,\cdots,9 \\ \frac{X_{i-9}+X_{i-8}+\cdots+X_i}{10} = \frac{10 \cdot Y_{i-1}+X_i-X_{i-10}}{10}, & i \geq 10 \end{cases} \quad (3.4)$$

As stated in the above formula, the first 9 values are arithmetically averaged and the rolling averaging starts after 0.1s execution time, in other words, after sampling the first 10 points.

On the top left of the GUI, the control parameters for the auto-tuned PID controller are listed, including the proportional gain, integral time and derivative time. A detailed description of the PID control algorithm is given in the next section. As discussed earlier, the PID controller is designed to maintain the temperature of the filter holder at its target value 47 ºC. For example, if the actual temperature of the filter holder falls below 47 ºC or the falling rate of the temperature is high, the heater voltage increases; if the actual temperature of the filter holder is above 47 ºC or the rising rate of the temperature is high, the heater voltage decreases. In practice, however, the controlled heater voltage is most often at its maximum value, i.e. 5V due to high thermal dissipation of the sample pipe. Apart from the PID control of the voltage output, the heater voltage output can be forced to zero regardless of what the PID control demands when several extreme conditions are met as follows:

- The diluent air flow rate is lower than 0.02 g s^{-1};

- The temperature of heated diluent air is above 350 ºC;
- The LabVIEW system stops for various reasons prior to turning off the heater.

The round LED on the front panel determines the compliance with the E/ECE/324 regulation No. 83 regarding filter face velocity. It will give a warning if the calculated filter face velocity falls outside the range of 20 – 80 cm/s as stated in the regulation. The digital output controlling the solenoid valve can be turned on by pressing the 'SV on?' button.

3.5 PID control Algorithms

3.5.1 Introduction of PID Control

Currently, the Proportional-Integral-Derivative (PID) algorithm is the most common control algorithm used in industry. PID controls processes that include heating and cooling systems, fluid level monitoring, flow control, and pressure control. In PID control, a process variable and a set point have to be specified. In this dilution system, the process variable is the temperature of the filter holder which needs to be controlled, and the set point is the desired value of 47 ºC. A PID controller determines an output value, i.e. the heater voltage and then applies this output value to the system, which in turn drives the process variable toward the set point value as illustrated in Fig. 3.8.

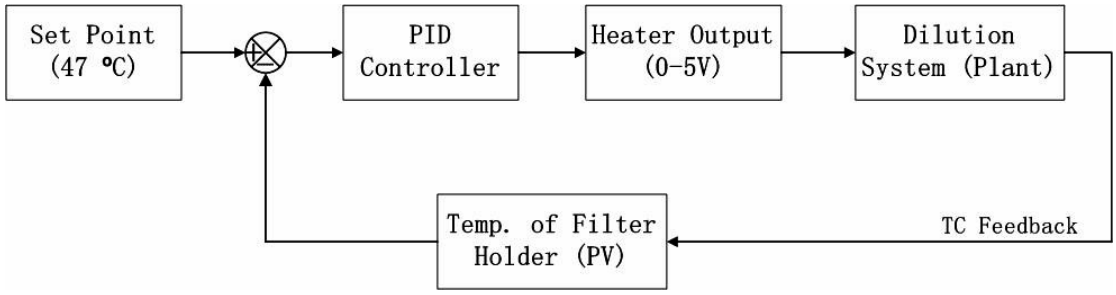

Fig. 3.8 Block diagram of the PID controller in the dilution system

The controller is designed in such a way that, at any given moment, the difference between the process variable and the set point is used by the control system algorithm (compensator) to determine the desired actuator output to drive the system (plant). In this case, the actuator output is the DC power supply for the electric heater ranging from 0-5V. Driving an actuator means turning on the heater which will lead to an increase in the temperature of the filter holder.

In many cases, the actuator output is not the only source that has an effect on the process variable. As far as this dilution system is concerned, there might be a number of sources disturbing the temperature of the filter holder such as ambient air turbulence, fluctuations of the exhaust temperature, flow rates etc. Such a term is referred to as disturbance in control textbooks. It is necessary to design the control system to minimize the effect of disturbances on the process variable. These disturbances are normally highly stochastic and unpredictable. Therefore, an Auto-tuning PID wizard in LabVIEW was adopted to overcome the effects of disturbances. More details can be found in next section.

3.5.2 PID Algorithms in LabVIEW Control Toolkit

The following schematic illustrates how the PID controller works in a closed-loop system. As the name suggests, PID algorithm consists of three basic coefficients: proportional, integral and derivative which are auto-tuned to give an optimal response. The current error used in calculating proportional, integral and derivative action is the difference between the process variable that needs to be controlled and its set point value. In this dilution system, the current error refers to the difference between 47 ºC and the current temperature of the filter holder.

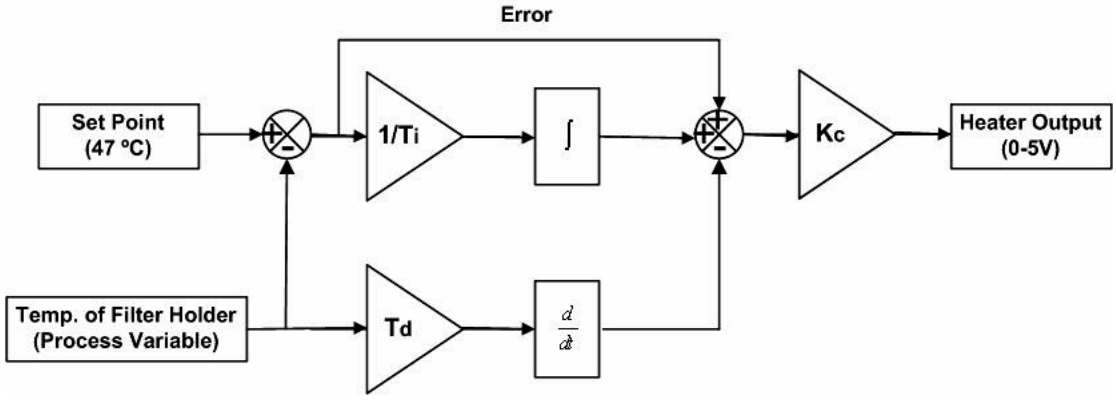

Fig. 3.9 Block diagram of a basic control algorithm

The proportional component is the controller gain K_c times the error, as shown in equation 3.5. For instance, if the current error is 0.1 degrees Celsius, a proportional gain of 50 would produce a proportional response of 5. In general, increasing the proportional gain will increase the speed of the control system response. However, if the proportional gain is too large, the process variable will begin to oscillate or even become unstable (PID and Fuzzy Logic Toolkit User Manual 2009).

$$u_{\mathrm{P}}(k) = K_{\mathrm{c}} \times e(k) \tag{3.5}$$

The integral component integrates the error over time. In LabVIEW PID Toolkits, trapezoidal integration, as shown in equation 3.6, is used to avoid sharp changes in integral action when there is a sudden change in process variable or set point. The integral response will continually increase over time until the error is zero, so the effect is to drive the steady-state error, which is the final difference between the process variable and set point, towards zero (PID and Fuzzy Logic Toolkit User Manual 2009).

$$u_{\mathrm{I}}(k) = \frac{K_{\mathrm{c}}}{T_{\mathrm{i}}} \sum_{i=0}^{k} \left[\frac{e(i)+e(i-1)}{2} \right] \Delta t \tag{3.6}$$

The derivative component causes the output to decrease if the process variable is increasing rapidly. In other words, the derivative response is proportional to the rate of change of the process variable. To avoid the derivative component saturating the output, the derivative action only applies to the process variable because changes in the set point are almost always abrupt. Equation 3.7 represents this partial derivative action. Increasing the derivative time (T_{d}) will cause the control system to react more strongly to changes in the error and hence increase the overall control system response speed. However, in this dilution control system, a very small derivative time (T_{d}) of 0.001 (min) was used because the derivative response is highly sensitive to noise in the process variable signal. A larger derivative time could make the control system unstable due to the fluctuation of the temperature of the filter holder. In addition, a Butterworth IIR low pass filter was used to mitigate the noise in the temperature measurement and hence to avoid the system becoming out of control.

$$u_{\mathrm{D}}(k) = -K_{\mathrm{c}} \frac{T_{\mathrm{d}}}{\Delta t} [PV_{\mathrm{f}}(k) - PV_{\mathrm{f}}(k-1)] \tag{3.7}$$

In practice, the PID controller output is the summation of the above three components as shown in equations 3.8 and 3.9.

$$u(k) = u_{\mathrm{P}}(k) + u_{\mathrm{I}}(k) + u_{\mathrm{D}}(k) \tag{3.8}$$

$$u(t) = K_{\mathrm{c}}\left[(SP - PV) + \frac{1}{T_{\mathrm{i}}}\int_0^t (SP - PV)dt - T_{\mathrm{d}}\frac{dPV_{\mathrm{f}}}{dt}\right] \tag{3.9}$$

As discussed earlier, gains in the PID controller can amplify the noise in the process variable signal and produce unnecessary fluctuations in the actuator output, especially when the USB 6008 card is used, as electrical interference could disturb the actual signal dramatically. A Butterworth IIR low pass filter was used with the cut-off frequency of 100Hz. The comparison of PID controller response with and without low pass filter is illustrated in Fig. 3.10.

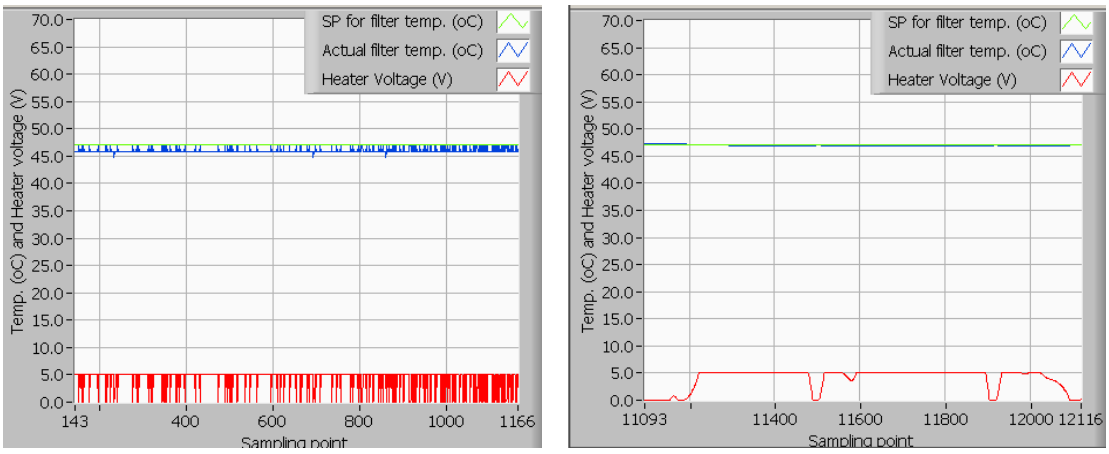

(a) PID control without digital filters *(b) PID control with digital filters*

Fig. 3.10 Effects of digital filters on PID control

Generally speaking, a proportional controller (K_{p}) will have the effect of reducing the rise time and will reduce but never eliminate the steady-state error. An integral control

(K_i) will have the effect of eliminating the steady-state error, but it may make the transient response worse. A derivative control (K_d) will have the effect of increasing the stability of the system, reducing the overshoot, and improving the transient response. Effects of each of controllers K_p, K_d, and K_i on a closed-loop system are summarized in Table 3.2.

Table 3.2 Effect of PID controllers on closed-loop system

Control parameter	**Rise time**	**Overshoot**	**Setting time**	**Steady-state error**
$\boldsymbol{K_p}$	Decrease	Increase	Small change	Decrease
$\boldsymbol{K_i}$	Decrease	Increase	Increase	Eliminate
$\boldsymbol{K_d}$	Small change	Decrease	Decrease	Small change

It is worth noting that these descriptions may not be exactly accurate, because K_p, K_i, and K_d are dependent on each other. In fact, changing one of these variables can change the effect of the other two. For this reason, the table should only be used as a reference when determining the values for K_i, K_p and K_d.

3.5.3 Auto-tuning PID Used in the Dilution System

The PID function used in this work is the auto-tuning PID VI which automatically tests the control system to determine new PID parameters that improve the controller performance. This method maintains closed-loop control during the tuning process. The reasons for adopting the Auto-tuning PID algorithm are threefold:

1) The disturbances such as ambient air turbulence and fluctuations of the exhaust temperature could cause the dynamics of the control system to vary over time;

2) The control parameters that produce a desired response at one operating point might not produce a satisfactory response at another operating point. For instance, the temperature of the filter holder will exhibit a much faster response to heater output when a short pipe is used than it will when a longer pipe is used. The dilution ratio could also change the response rate of the process variable;
3) This system exhibits a marked dead-time which is a delay between when a process variable changes and when that change can be observed. The change in the thermal inertia of the heater and pipes could lead to significant changes in the dead-time. Therefore, a universal set of control parameters cannot be optimal over time.

LabVIEW uses a trial and error method (Ziegler-Nichols Method) to automatically tune the parameters. Fig. 3.11 illustrates the auto-tuning process excited by the set point relay experiment, which connects a relay and an extra feedback signal with the set point.

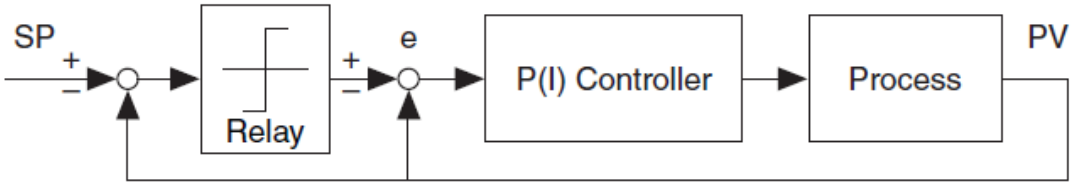

Fig. 3.11 Process under PID control with set point relay

Because auto-tuning is a refining process, an initial set of PID parameters that produce stable control of the system is required. After the auto-tuning, the optimal

gains for *P, I* and *D* to get an ideal response from the control system can be obtained as exemplified in Fig. 3.12.

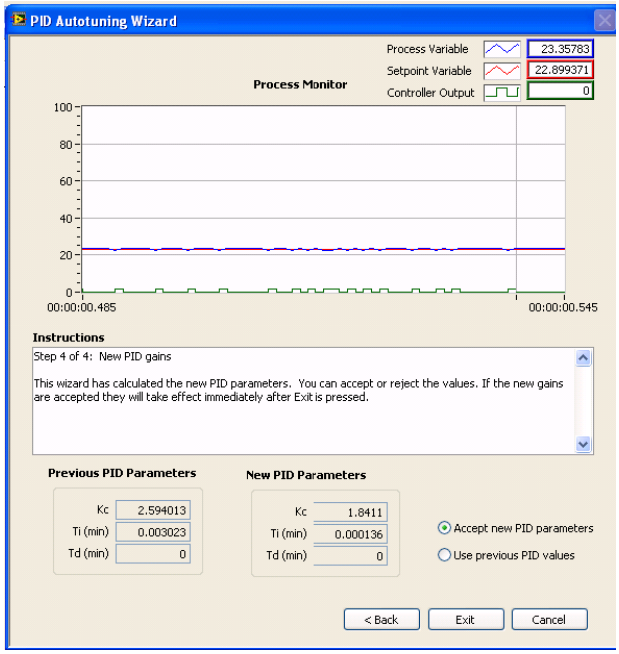

Fig. 3.12 An example of PID Auto-tuning process in LabVIEW

Fig. 3.12 shows an example of a manual auto-tuning process. The PID Auto-tuning Wizard in LabVIEW also facilitates automatic auto-tuning if all the relay parameters for auto-tuning are pre-determined. In this work, once the control system has reached its stable condition in which the temperature of the filter holder is 47 degrees Celsius, the PID parameters will produce satisfactory control without any changes in the control parameters. In other words, there is no need to refresh the PID parameters throughout the test once a stable condition has been reached.

3.6 Case Study

This dilution system has been used in both the single cylinder and V8 engines to undertake various experiments. The main function of the system is to facilitate filter

sampling with controlled dilution parameters including dilution ratio, filter temperature and filter face velocity. But the system can be equally useful in other applications where a controlled dilution system is required. This section illustrates the use of the system in a series of V8 engine experiments to investigate the effects of residence time in a VPR (Volatile Particle Remover) on PM emissions.

3.6.1 Experimental set-up and test procedure

The engine used for these tests was a Jaguar V8 GDI engine described in chapter 4. It was set up with a VPR for measuring the pre-catalyst PM sample. The dilution system was used to adjust the extraction flow rate of the raw exhaust flowing through the VPR, hence adjust the residence time in the VPR. The following schematic shows the configuration of the overall system.

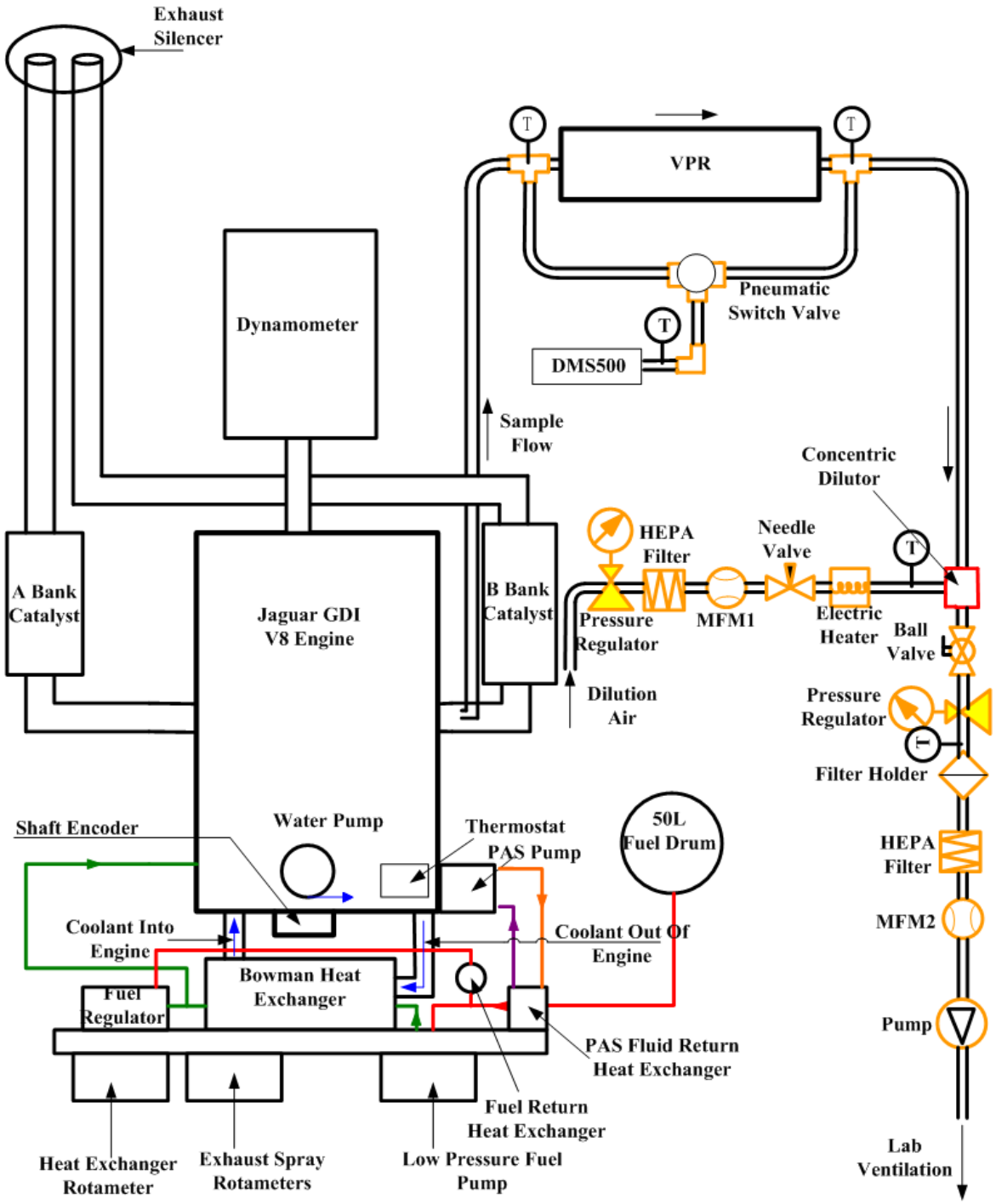

Fig. 3.13 Configuration of VPR experiments in the V8 GDI engine

The primary objective of the experiments is to examine the effect of the residence time in the VPR on pre-catalyst PM emissions. The total flow rate of the diluted gas was fixed by the suction pump, so that the flow rate of the post-VPR aerosol could be adjusted by changing the dilution ratio of the dilution system, hence the residence

time in the VPR could be adjusted. The dilution ratios selected in this work were 8, 6, 4, 2, and the corresponding mass flow rate of post-VPR aerosol caused by the dilution system were 0.070 g s^{-1}, 0.090 g s^{-1}, 0.121 g s^{-1}, 0.200 g s^{-1} respectively. The DMS500 provides a relatively constant suction for the post-VPR aerosol as well. Therefore, the total flow rate of the aerosol in the VPR was a combined result of suction from both the DMS500 and the dilution system. The volumetric flow rate of post-VPR aerosol can be calculated as follows:

$$\dot{V}_{\mathrm{vpr}} = \frac{(\dot{m}_{\mathrm{DMS}}+\dot{m}_{\mathrm{DIL}})\cdot R_{\mathrm{exh}}\cdot(T_{\mathrm{pre}}+T_{\mathrm{post}})/2}{p} \tag{3.10}$$

Where $\dot{m}_{\mathrm{DMS}}$ and $\dot{m}_{\mathrm{DIL}}$ refer to the mass flow rate of the post-VPR aerosol caused by the DMS500 and the dilution system respectively; T_{pre} and T_{post} refer to the pre-VPR and post-VPR temperature. Their average value, of 150 ºC and 200 ºC, was used to simplify the calculation; p refers to the average pressure in the VPR, in this case, the exhaust pressure of 1.01 bar was used instead to avoid the difficulty of measuring the pressure inside the VPR; R_{exh} is the specific gas constant for the exhaust, which can be calculated as follows:

$$R_{\mathrm{exh}} = \frac{R_0}{M_{\mathrm{exh}}} \tag{3.11}$$

In which, R_0 is the molar gas constant (8.3145 $JK^{-1}mol^{-1}$), and M_{ex} is the molar mass of exhaust gas, which is given by the sum of mole fraction weighted molar mass of the individual species.

Since the DMS500 has a nominal sample flow rate of 0.8 L/min, and this value is normalized under standard condition (p_0 = 1bar, T_0 = 273.15K). Therefore, the mass flow rate of the post-VPR aerosol caused by the DMS500 is:

$$\dot{m}_{\mathrm{DMS}} = \frac{0.8l}{min} \times \frac{\frac{1}{60}min}{s} \times \rho_{\mathrm{exh}} = \frac{\frac{2}{150}l}{s} \times \frac{p_0}{R_{\mathrm{exh}} \cdot T_0} \tag{3.12}$$

For most fuels used in the experimental work, especially for this particular test fuel, PURA, the fuel composition can be simplified by a good approximation of CH_2. The stoichiometric combustion can then be expressed as follows:

$$CH_2 + \frac{3}{2}\left(O_2 + \frac{79}{21}N_2\right) \rightarrow CO_2 + H_2O + \left(\frac{3}{2} \times \frac{79}{21}\right)N_2 \tag{3.13}$$

The percentages of the 3 products, i.e. CO_2, H_2O and N_2 are 13.1%, 13.1% and 73.8% respectively. Therefore, the molar mass of this exhaust gas is:

$$M_{\mathrm{exh}} = 13.1\% \times M_{\mathrm{CO_2}} + 13.1\% \times M_{\mathrm{H_2O}} + 73.8\% \times M_{\mathrm{N_2}} \approx 28.8\ (g/mol) \tag{3.14}$$

By integrating the above equations, the volumetric flow rates of the post-VPR sample can be obtained with different dilution ratios of the dilution system. Finally, the residence time is determined as follows:

$$t_{\mathrm{vpr}} = \frac{V_{\mathrm{vpr}}}{\dot{V}_{\mathrm{vpr}}} \tag{3.15}$$

Where V_{vpr} is the VPR volume (0.34L), which was estimated by multiplying the cross-sectional area of the inner pipe by its length.

3.6.2 Experiment Results

The engine was running under a warm condition with the engine speed being 1500 rpm and the MAP being 525 mbar. The pre-catalyst exhaust was extracted into a VPR. The PM emissions upstream and downstream of VPR were measured by the DMS500. The residence time of aerosol in the VPR was changed by adjusting dilution ratios as discussed in the previous section. 4 different mass flow rates of the post-VPR aerosol were chosen by sweeping the dilution ratio from 2 to 8 with an increment of 2. Table 3.3 summarizes the correlations of mass flow rates and residence times.

Table 3.3 Correlations between dilution ratios, mass flow rates and residence times

Test number	Dilution ratio	Mass flow rates of post-VPR sample (g s^{-1})	Residence time in the VPR (s)
MFM1	8	0.087	3.91
MFM2	6	0.107	3.18
MFM3	4	0.138	2.46
MFM4	2	0.217	1.57

PM measurements were taken for both pre- and post-VPR samples to assess the efficiency of the VPR removing the nucleation PM with different residence times. The size resolved number and mass concentrations of all cases are shown in Fig. 3.14. Solid lines represent pre-VPR results whilst broken lines represent post-VPR results. 1,2,3,4 refer to the test number of MFM1, MFM2, MFM3, MFM4.

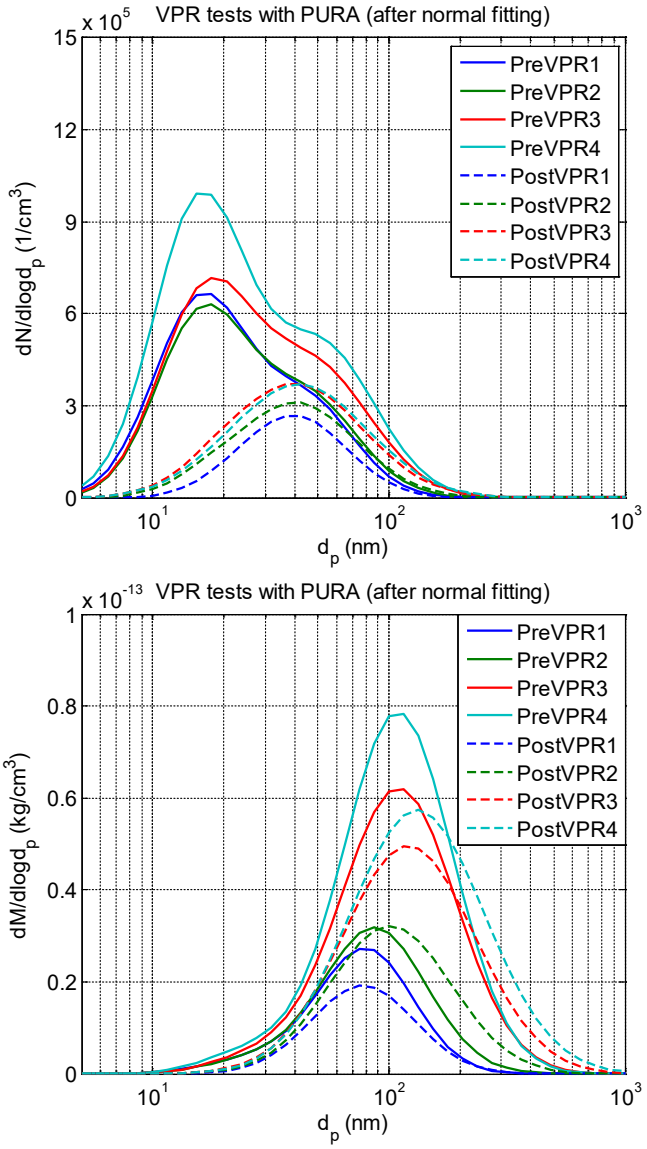

Fig. 3.14 *Size resolved number (top) and mass (bottom) concentrations of pre- and post-VPR PM emissions with different residence time using Equation 2.9*

Fig. 3.14 exhibits a few trends as follows:

- For the number spectra, pre-VPR samples showed clear bi-lognormal spectra characteristics whilst post-VPR samples had much more accumulation PM than nucleation PM, which implies that higher quantity of nucleation PM in pre-VPR samples was present than in post-VPR samples;

- For the mass spectra, the accumulation PM dominated in all cases. The contribution of nucleation mode PM was largely negligible.

Fig. 3.15 shows total Pn (Particulate number) and Pm (Particulate mass), which were calculated by numerically integrating the results on the corresponding spectra. Red boxes contain truncated data for particles with a size range of 23 – 700 nm. The purpose of truncating data into such a range is to deliberately eliminate noise at low and high sizes.

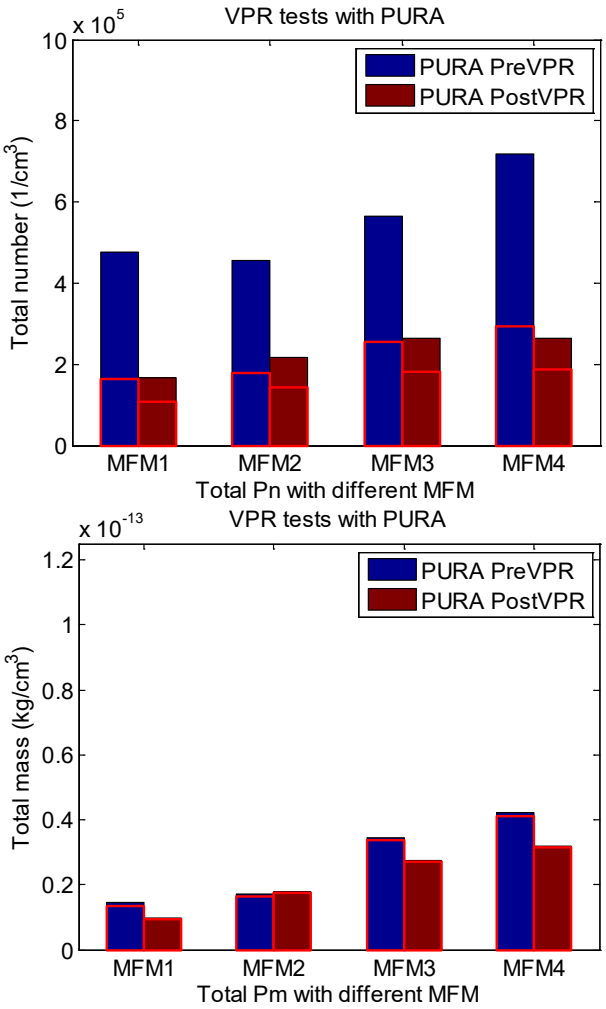

Fig. 3.15 Total Pn (top) and Pm (bottom) of pre- and post-VPR emissions with different residence time (the red boxes contain data for particles in the size range of 23 - 700 nm)

It can be seen that:

- Post-VPR samples had universally lower Pn and Pm than pre-VPR samples, independent of residence time, which implies that the VPR reduced PM emissions significantly;
- As the residence time in the VPR decreased, both the total Pn and Pm increased. One possible reason for this could have been that more PM emissions escaped from oxidation within the VPR when the residence time was insufficient.

To assess the effects of VPR on nucleation PM and accumulation PM separately, the ratio between post-VPR and pre-VPR in terms of total Pn and Pm was calculated and plotted on Fig. 3.16.

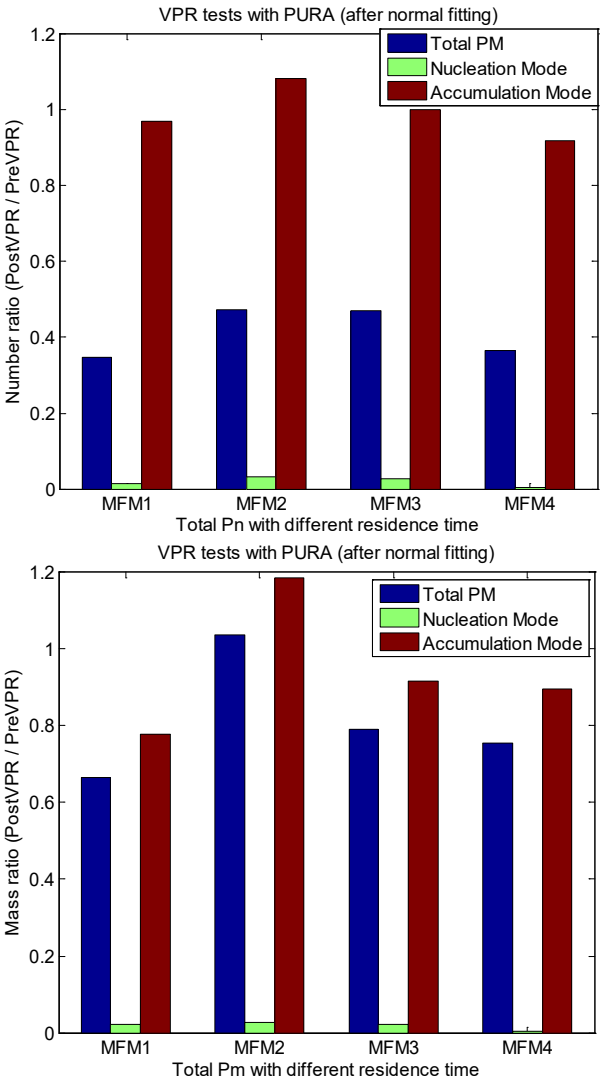

Fig. 3.16 The total Pn (top) and Pm (bottom) ratio between pre- and post-VPR in terms of different PM modes

From Fig. 3.16, it is safe to draw the following conclusions:

- Regardless of the residence time, the removing efficiency of VPR for nucleation PM was almost 100% whilst VPR had little influence on accumulation PM;
- The extent of the overall PM reduction after VPR was larger on number basis than that on mass basis because nucleation PM has much less contribution on the total mass than accumulation PM.

3.7 Summary

The automatic dilution system used for filter sampling has been described in detail in this chapter. It consists of an in-house developed LabVIEW based program, a National Instruments^{TM} USB-6008 data acquisition card and an interface box. The LabVIEW software is designed to not only acquire process parameters such as different temperatures and mass flow rates but also control the temperature of the filter by adopting the auto-tuning PID control function in LabVIEW. The fundamental theory of the PID algorithm deployed in LabVIEW control toolkit has been introduced in depth. A detailed description of the main components in the USB-6008 DAQ card which was used in this application is given followed by an explanation of common buffer errors during the data acquisition process. The dedicated interface box facilitates signal conditioning so as to produce appropriate signals for either driving external components or being logged by the DAQ card.

Apart from filter sampling, this dilution system can also be used in a wide range of applications in which a dilution system with controlled sampling temperature and dilution ratio is required. Section 3.6 exemplified the application of the dilution system in a series of engine experiments with a VPR in which the residence time of the VPR was swept by adjusting the dilution ratio. Another reason for adopting the dilution system in the tests is that it could prevent the water in the engine-out exhaust condensing in the mass flow meter by adding heated dilution air.

4. Effects of TWC, Split Injection, Ignition Timing and Injection Timing on PM Emissions from Oxygenate-Fuelled GDI Engines

4.1 Introduction

Injection mode, ignition timing and injection timing are all parameters that can be controlled or calibrated in engine control strategies. It is thus important to understand how they influence in-cylinder conditions, and their effects on PM emissions. A production TWC (Three Way Catalyst) was fitted to the V8 engine, and as the name suggests, it is used primarily to reduce three gaseous emissions i.e. NOx, HC and CO. However, there is little information available that addresses the impact of a TWC on PM emissions, especially on PM size distributions. Therefore, the effects of the TWC on PM emissions were also investigated by comparing the pre- and post-catalyst PM emissions data.

Tests have been conducted with fuels of known composition in both a single cylinder engine and V8 engine with a three-way catalyst. The V8 engine used an unleaded gasoline (Shell PURA) with known composition and distillation characteristics as a base fuel and with 10% by volume ethanol. The single cylinder engine used a 65% iso-octane - 35% toluene mixture as its base fuel. The engines had essentially the same combustion system, with a centrally mounted 6-hole spray-guided direct injection system.

Both engines were operated at 1500 rpm under part load. The tests with the single cylinder engine used relative AFRs of 0.9, 1.0 and 1.1 with an ignition timing sweep of 15-45° bTDC. The V8 tests were stoichiometric with injection timing sweeps

during induction (120 to 360° bTDC), with a reduction in both PM number and mass due to reactions in the catalyst.

The main focus of this work is the effect of fuel composition (including ethanol) on PM emissions. Various engine parameter sweep-tests were undertaken (ignition timing, injection timing and air fuel ratio) on the two SGDI engines. Particle size distributions were recorded using a Cambustion Ltd DMS500 (Differential Mobility Spectrometer) and these have also been converted to mass distributions based on a size-dependent PM density model.

4.2 Experimental Apparatus and Test Method

4.2.1 Engines

The two test engines were supplied by Jaguar: a 5L AJ133 V8 naturally aspirated engine and a single-cylinder optical access engine with essentially the same SGDI combustion system. The combustion system, as shown in Fig. 2.2, comprises a centrally mounted six-hole injector and a spark plug inclined to the longitudinal axis of the cylinder at 18 degrees. Details of both engine specifications can be found in Section 2.2.

4.2.2 Fuels

Two types of fuel served as base fuels for the present work: a toluene reference fuel and PURA. The toluene reference fuel consists of 65% iso-octane and 35% toluene by volume. The reason for using these components is that iso-octane and toluene are

representative of the alkane and aromatic fractions found in unleaded gasoline respectively.

PURA is a test fuel provided by Shell. It has about 22% aromatics which is lower than that present in some European ULG and it has 64% iso-paraffins which is higher than the European ULG. It also has a slightly lower final boiling point. The detailed information regarding the composition and distillation characteristics of PURA is shown in Table 4.1.

Table 4.1 PURA composition and distillation characteristics (analysis by Shell)

Density @ 15°C (kg/L)	0.7243
Reid Vapour Pressure (mbar)	574
Distillation 10% (°C)	53.4
Distillation 50% (°C)	101.8
Distillation 80% (°C)	126.9
Final boiling point (°C)	168.8
Research Octane Number	95.7
Motor Octane Number	87.6
C	6.77
H	13.48
Paraffins (%V)	7.58
Iso-Paraffins (%V)	63.53
I+N Paraffins (%V)	71.11
Olefins (%V)	4.41
Naphthenes	2.47
AROMATICS	21.87
OXYGENATES	0
TOTAL	99.86
Benzene	0.36
Stoichiometric Air Fuel Ratio	14.74
Enthalpy of Combustion (MJ/kg, Gas)	-43.903
Enthalpy of Combustion (MJ/kg, Liq.)	-43.546
thus, heat of Vap. (MJ/kg)	0.357
H/C ratio	1.99114
O/C ratio	0

The percentage of ethanol blended in both base fuels is 10% by volume (termed as E10). Some properties of pure ethanol are listed in Table 4.2.

Table 4.2 Properties for ethanol, iso-octane and toluene (Stone, 1999 and Heywood, 1988)

	Ethanol	Iso-octane	Toluene
Density @ 15°C (kg/L)	0.786	0.690	0.865
Research Octane Number	107	100	120
Boiling Point (°C)	78.3	99.2	110.6
Stoichiometric Air Fuel Ratio	9.00	15.13	13.50
Lower heating value (MJ/kg)	26.9	44.3	40.6
Heat of Vap. (kJ/kg, 25ºC)	840	308	412
H/C ratio	3	2.25	1.14
O/C ratio	0.5	0	0

Price *et al.* (2007) predicted the ASTM D86 distillation curves for blends of ULG95 and its ethanol blends. The distillation curve modelling showed that ethanol blended in ULG results in a big reduction in the front end volatility and rise in the mid range volatility.

Shell also predicted the ASTM distillation curves for PURA and PURA E10 as shown in Fig. 4.1. The curves are significantly different in shape. The plateau region associated with the ethanol is clearly visible on the E10 curve and is followed, at higher percentages evaporated, by the transition back to normal PURA behaviour once the ethanol has gone.

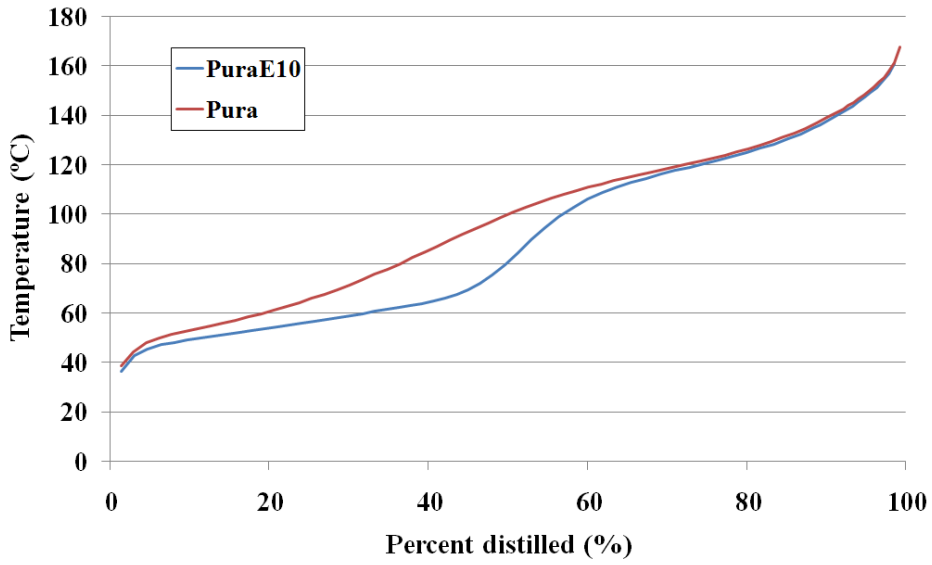

Fig. 4.1 *Distillation curves for PURA and PURA E10 (courtesy of Shell)*

Hsieh *et al*. (2002) examined the fuel properties of ethanol-gasoline blends using the standard ASTM methods. It was found that with increasing ethanol content, the heating value of the blended fuels decreased, while the octane number of the blended fuels increases. It was also found that with increasing ethanol content, the Reid Vapour Pressure (RVP) of the blended fuels initially increases to a maximum at 10% ethanol addition, and then decreased (Hsieh *et al*., 2002). Poulopolous *et al*. (2001) also reported that ethanol addition caused a rise in the RVP, which indicated indirectly increased evaporative emissions (Poulopoulos *et al*., 2001).

It is worth noting that, for a stoichiometric mixture, the latent heat of evaporation of ethanol is nearly 5 times higher than that of gasoline - this could make evaporation of ethanol-gasoline fuel more difficult and hence lead to higher heterogeneity of the mixture than that for pure gasoline. The lower stoichiometric air fuel ratio of ethanol relative to gasoline requires about 1.5 times more ethanol to achieve the same energy output (Hsieh *et al*., 2002).

4.2.3 Instrumentations and Sampling

PM number (Pn) concentrations and size distributions were measured with a Cambustion Ltd DMS500. The Cambustion Ltd sampling system was used, as it has a heated sample line with dilution air added at the entrance to its sample line.

Two sampling probes, upstream and downstream of a three-way catalyst, were connected to a pneumatic switching valve which enabled the sampling point to be switched from pre-catalyst to post-catalyst. The DMS500 was connected to the outlet of the switching valve in conjunction with its heated sample line to prevent water condensing.

Whatman^{TM} GF/C glass-fibre filters were used to sample the engine-out PM. An automated dilution system (as described in Chapter 3) was used to monitor and log various operational parameters such as the diluent gas flow rate; the diluted gas flow rate; the instantaneous dilution ratio (calculated); and the temperature before and after the filter holder. The sampling time for each engine operating point was 20 minutes and the average dilution ratio was around 5. This dilution ratio was selected to obtain a good balance between the amount of PM needed for subsequent analysis and the sampling time. The temperatures before and after the filter holder were within the range 42-52 ºC throughout the tests. The PM laden filters were stored in a controlled room (47±5 ºC; 45±8% RH) for one night before being analysed by TGA.

4.2.4 Test Matrices and Data Processing

Four sets of data are presented in this chapter. Table 4.3 summarizes the test matrices for both the V8 and single-cylinder engine tests.

Table 4.3 Test matrix

Test Sequence	1	2	3	4
Engine	Single-cylinder	V8	V8	Single-cylinder
Base Fuel	65% iso-octane+35% toluene	Pura	Pura	Pura
Speed (rpm)	1500	1500	1500	1500
Manifold Pressure (bar absolute)	0.479	0.525	0.525	~0.5
Air Flow Rate (L/s)	-	-	-	1.21
Fuel Pressure (bar)	150	150	150	150
Injection Timing	280° bTDC	360-120° bTDC in 30° decrements	280° bTDC	330-150° bTDC in 30º decrements
Ignition Timing	15-45° bTDC in 10° increments	35° bTDC	5-45° bTDC in 5° increments	15-45° bTDC in 5° increments
Relative AFR	0.9, 1.0, 1.1	1	1	1
Coolant Temperature (ºC)	80	90	90	90

Both the base fuel and its E10 blend were used and comparisons were made in terms of both PM number concentrations (Pn) and mass concentrations (Pm). The engines were running under steady conditions and the DMS500 recorded 2 minutes of data for each test point. In the first set of tests, filter samples were also taken in some cases for 20 minutes. In the last set of tests, the comparison between triple and single injection tests was also made with PURA and PURA E10. The SOI (Start of Injection) for triple injection was 300°, 290°, 280° bTDC whilst the SOI for single injection was 280° bTDC. A series of injection and combustion images was captured by a Photron PCI-1024 high speed video camera at up to 9,000 fps.

Number concentrations normalized with the differential interval of the logarithm of particle size were automatically inverted from the matrix of the DMS500 electrometer currents. The DMS500 software uses a specially written Bayesian statistical algorithm

to generate two lognormal distribution fitting spectra. Details of the bi-lognormal fitting were introduced in Section 2.4.

A PM density model introduced in Section 2.4 was adopted to convert PM number concentrations to mass concentrations. The size resolved number and mass concentrations can be plotted on either semi-log or double-log scales depending on how many orders of magnitude the data span.

4.3 Results and Discussion

4.3.1 Single-cylinder Engine Tests Results

Test Sequence 1 - Tests with the Toluene Reference Fuel and its E10 Blend

The ignition timing sweep tests were conducted with the toluene reference fuel as a base fuel (65% iso-octane - 35% toluene) and its E10 blend at relative AFRs of 0.9, 1.0 and 1.1. The size and mass distributions are shown in Fig. 4.2. The mass distributions were calculated from the size distributions using Equation 2.9.

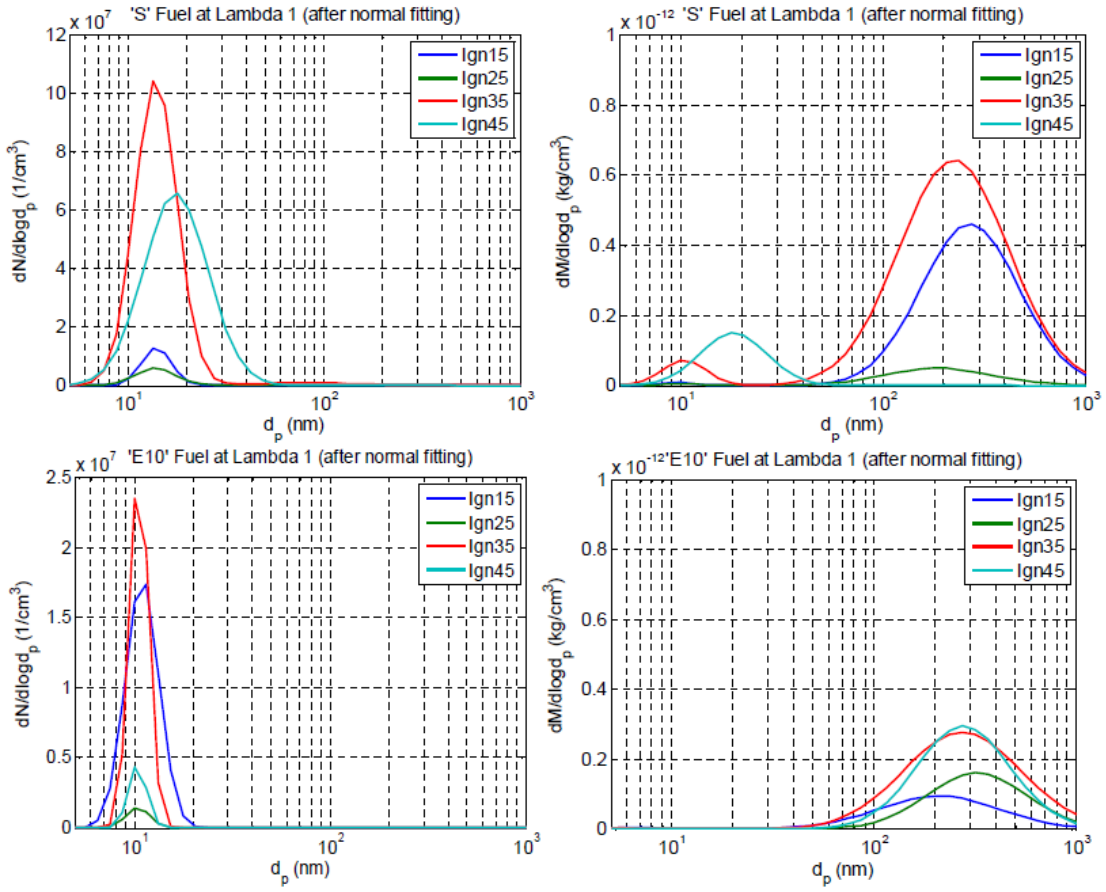

Fig. 4.2 *Size resolved number concentrations and mass concentrations of PM emissions at different ignition timings with stoichiometric air fuel ratio ('S': base fuel; 'E10': E10 blend fuel)*

The nucleation artefact at the ignition timing of 45° bTDC with the base fuel was not found in the E10 case. A possible reason would be that at the ignition timing of 45° bTDC there is least time for fuel evaporation and hence the poor heterogeneity of the mixture as a result of the higher latent heat of evaporation of ethanol. A poorly mixed mixture can lead to higher soot emissions in the accumulation mode (100-500nm). As a result, more surface area is available for absorbing the nucleation mode PM, and this could then cause a reduction of the particulate number in the nucleation mode (5-100nm).

For the mass weighted distributions, the peak positions are for much larger size particles than on the number spectra. It is invariably the case that PM in the accumulation mode, despite the lower concentration in the number spectra compared with PM in the nucleation mode, can still dominate the mass weighted distributions. The E10 case has a larger sized peak position than the base fuel, and this indicates that more soot agglomerates were present when E10 was used.

However, the response of the PM emissions to ignition timing was less clear. There might be two reasons for this: (1) the baseline level was less than one order of magnitude higher than the background level, which made the signal to noise ratio too low to show any definite trends; (2) 2 minutes sampling time was insufficient to increase the signal/noise ratio by averaging the data.

The results for relative AFR 1.1 were broadly similar to the results for relative AFR 1 shown above. The number and mass concentrations for relative AFR 1.1 were lower than for relative AFR 1 by less than one order of magnitude.

Filter samples were also taken at the following three operating conditions and the results are listed in Table 4.4.

1. Ignition timing of 35º bTDC with the base fuel;
2. Ignition timing of 35º bTDC with the E10 blend;
3. Ignition timing of 15º bTDC with the base fuel.

Table 4.4 TGA results for the 3 filter samples

	Mass loss (mg)		Weight (%)	
	VOF	Carbon	VOF	Carbon
Condition 1	1.22	0.20	86.05	13.95
Condition 2	0.36	0.27	57.05	42.95
Condition 3	1.13	0.15	88.33	11.67

The volatile organic fraction (VOF) and carbonaceous content of the collected particulate matter was determined by Thermo-Gravimetric Analysis (TGA). One half of the Whatman^{TM} GF/C glass fibre filters was used for each condition. The sample was ramped to 500ºC in nitrogen to remove any volatile material and then ramped to 600ºC in air to combust the soot particles. The mass loss was monitored and logged throughout the TGA experiment.

Test conditions 1 and 3 showed similar mass losses in different volatility ranges, whilst condition 2 showed different characteristics. In other words, adding 10% ethanol by volume led to a significant rise in carbon content, however, little effect of ignition timing on PM composition was observed here.

Fig. 4.3 shows the particle size and mass distributions results at relative AFR of 0.9.

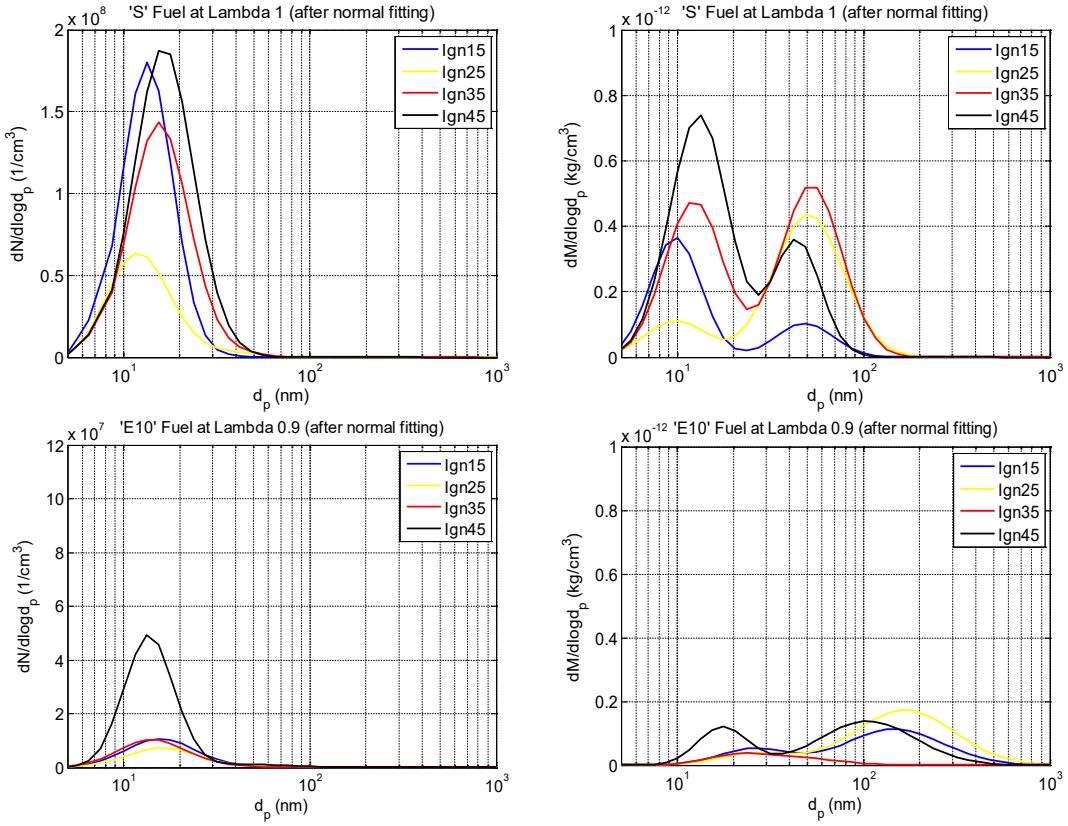

Fig. 4.3 *Size resolved number concentrations and mass concentrations of PM emissions at different ignition timings with a relative AFR of 0.9 ('S': base fuel; 'E10': E10 blend fuel)*

An obvious feature with this rich condition is the much higher emission levels compared to either the weak or stoichiometric mixture. Also, that adding ethanol leads to a reduction of Pn by more than one order of magnitude, while the reduction in Pm is by less than one order of magnitude. This is in contrast to operation at stoichiometric conditions, so the tendency for ethanol to reduce the homogeneity of the mixture appears to be less significant at the rich condition. However, liquid fuel drops will always be present in the cylinder, regardless of any change in ignition timing. Consequently, another competing effect seems to have dominated the results. That is, the 'leaning effect' of oxygen atoms in the E10 blend. The presence of oxygen in the fuel molecule reduces the concentrations of key intermediate species required for the formation of soot precursors (Litzinger *et al.*, 2000).

For the number spectra, the peak position of the Pn size distributions for the base fuel is slightly larger than for the E10 blend, which suggests that agglomeration or even homogeneous nucleation of organic species may occur, in addition to absorption onto the surface of larger particles due to the high PM emissions. It is worth noting that adding 10% by volume ethanol reduced the overall PM emissions under the rich condition.

For both fuels used here, advancing the ignition timing increased both the Pm and Pn with the exception of the ignition timing of 15° bTDC. Advancing the ignition timing shortened the time for fuel evaporation and subsequently caused more locally rich regions at the start of combustion, resulting in more PM emissions. Retarded ignition timing can also promote post combustion oxidation of PM during the expansion stroke because of the higher temperatures later into the expansion stroke. The total Pn and Pm for test sequence 1 are listed in Table 4.5.

Table 4.5 Summary of test sequence 1 in terms of total particulate number and particulate mass

Ignition timing	Total Number (1/cc)				Total Mass (kg/cc)			
	15°bTDC	25°bTDC	35°bTDC	45°bTDC	15°bTDC	25°bTDC	35°bTDC	45°bTDC
'S' Fuel, λ=1	2.28×10^{6}	1.16×10^{6}	2.22×10^{7}	2.59×10^{7}	2.77×10^{-13}	3.22×10^{-14}	4.39×10^{-13}	2.96×10^{-13}
'S' Fuel, λ=0.9	2.25×10^{8}	9.05×10^{7}	2.18×10^{8}	2.91×10^{8}	1.62×10^{-13}	2.48×10^{-13}	4.02×10^{-13}	4.06×10^{-13}
E10 Fuel, λ=1	3.25×10^{6}	1.72×10^{5}	2.83×10^{6}	4.33×10^{5}	0.77×10^{-14}	9.67×10^{-15}	2.00×10^{-14}	1.70×10^{-14}
E10 Fuel, λ=0.9	4.51×10^{6}	3.31×10^{6}	3.45×10^{6}	1.20×10^{7}	0.77×10^{-13}	1.18×10^{-13}	4.03×10^{-14}	9.28×10^{-14}

The trends with the rich mixture are clearer than with stoichiometric and weak mixtures. For the rich mixture, advancing the ignition timing increased both the PM

number and mass emissions, and the use of E10 reduced the number emissions by a factor of 24-63 and the mass emissions by a factor of 2.1-9.9.

Test Sequence 4 - Tests with PURA and PURA E10 in the Optical Engine

The ignition timing was swept from 10 to 45° bTDC in 5° increments with PURA only. Fig. 4.4 shows the size distributions of PM on number and mass bases.

The data are truncated to a size range of 23-700 nm using the Matlab code introduced in 2.4.1, and then plotted on a double log scale in order to show the difference between the cases more clearly. As mentioned in 2.4.1, European legislation excludes particles smaller than 23nm, and data above 700nm have been ignored as the number concentrations are low and comparable to the noise level in the instrument. The early ignition timings of 40° and 45° bTDC produced more Pn and Pm, but by less than one order of magnitude compared with the other cases. The remaining ignition timings gave very similar Pn and Pm distributions across the whole size range of 23-700nm, with little effect of ignition timing on the PM being observed.

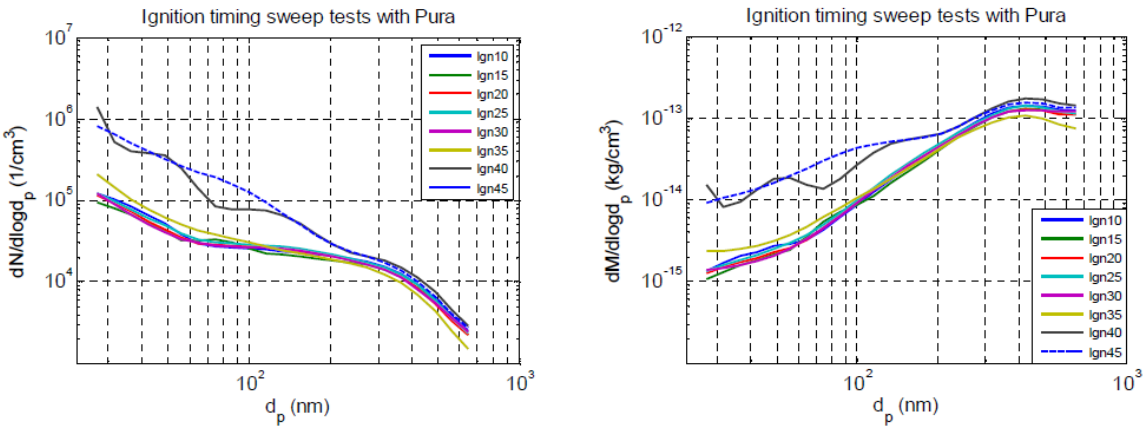

Fig. 4.4 *Size resolved number and mass concentrations of PM emissions at different ignition timings with PURA at stoichiometric conditions.*

Compared with previous results when the toluene reference fuel was used, the number and mass concentrations for PURA were lower by more than one order of magnitude. This may be attributable to the low aromatic contents of PURA, hence the soot precursor formation during combustion could be lower than that with the toluene reference fuel.

The injection timing was swept from 150-330° bTDC on the single cylinder engine with both PURA and PURA E10, and the results are shown in Fig. 4.5.

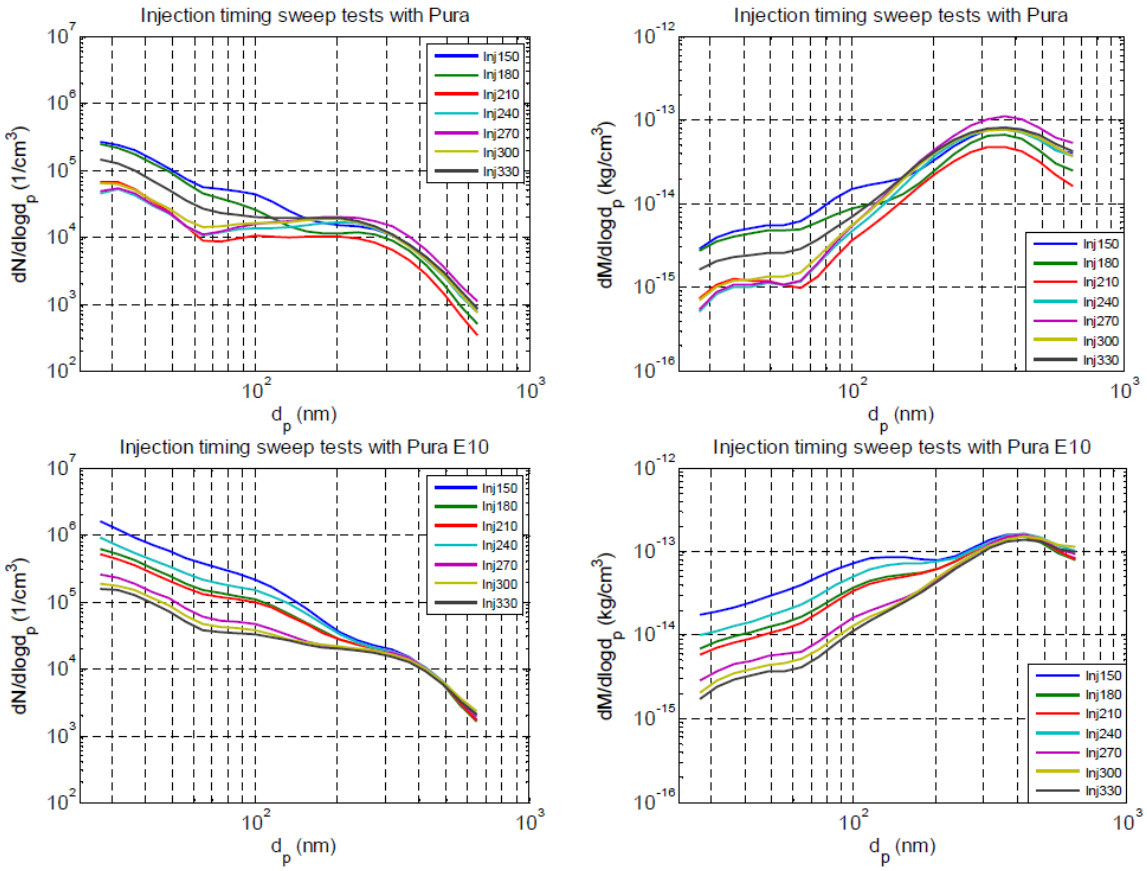

Fig. 4.5 *Size resolved number concentrations and mass concentrations of PM emissions at different injection timings with PURA and PURA E10 at stoichiometric conditions.*

In order to compare the data more clearly, both Pn and Pm spectra were again truncated with a size range between 23 – 700nm on a double log scale. Apart from the atypical high values for the injection timing of 150° bTDC with PURA and for the injection timing of 240° bTDC with PURA E10, the trend for both fuels is clear: advancing the injection timing decreased both the Pn and Pm. This is attributed to the reduction in time for fuel evaporation when the injection timing is retarded.

By numerical integration, using the trapezium rule in MATLAB, the total Pn and Pm can be calculated from the above size distributions. The average total Pn was larger with PURA E10 than with PURA by a factor of 4, whilst the Pm was higher by a factor of 3. One possible explanation is that due to the higher enthalpy of evaporation for ethanol than for PURA, the mixture at the starting point of combustion is less homogeneous when ethanol is blended. Serras-Pereira *et al*. (2008) found that a ULG fuel spray seemed to break-up and evaporate more than an ethanol spray, which may increase PM emissions for ethanol blends due to the relatively poorer evaporation (Serras-Pereira *et al*., 2008).

Test Sequence 4 - Comparison between triple and single injection

Comparison tests between triple and single injection were also carried out on the single-cylinder optical access engine with PURA and PURA E10. The triple pulses were converted from a single pulse by a gated pulse generator. The triple pulse system was intended to reduce jet penetration so as to reduce the possibility of wall wetting. The SOI (Start of Injection) for triple injection was 300°, 290°, 280° bTDC whilst the SOI for single injection was 280° bTDC. For each single and triple injection tests, two repeat runs were taken and the data are plotted in Fig. 4.6.

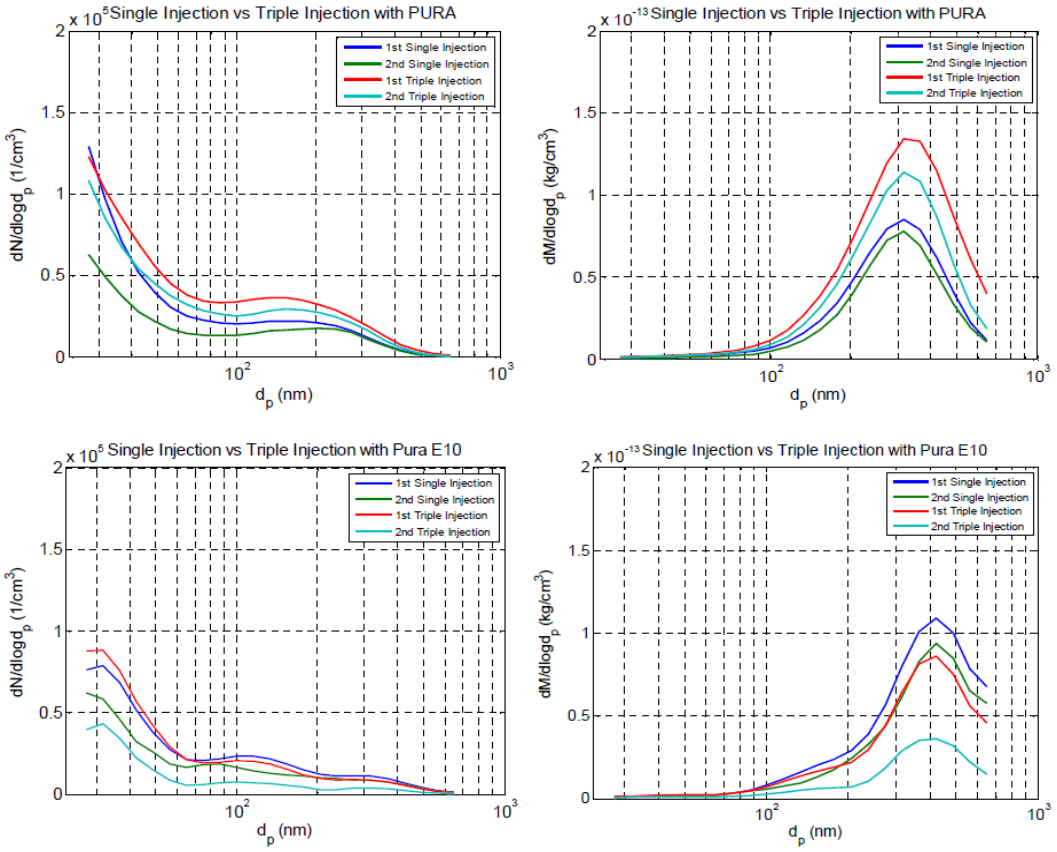

Fig. 4.6 *Size resolved number concentrations and mass concentrations of PM emissions for single and triple injection mode with PURA and PURA E10 at stoichiometric conditions.*

The low level of PM emissions for all runs is less than one order of magnitude higher than the background level, hence the relatively larger systematic error in the small size range (<23nm) and large size range (>700nm) could easily confound the actual results. On average, the triple injection with PURA E10 produced slightly less Pn and Pm than the single injection mode. This is thought to be due to the fact that triple injection should produce a more homogeneous mixture than single injection by reducing the amount of fuel at each pulse by 2/3. With PURA, the triple injection mode yielded slightly more PM emissions on both a number and a mass basis. The difference, however, was small. In other words, injection modes have little effect on both Pm and Pn spectra derived from the DMS500 measurements.

A series of injection and combustion images was captured by a Photron PCI-1024 high speed video camera in conjunction with synchronized cylinder pressure data recorded by a National Instruments^{TM} PCI-MIO-16E-1 data acquisition card with 12-bit resolution. 200 cycles of data were recorded for each operation point. The injection images were taken at 3,000 fps, which is equivalent to 3° CA per image whilst the combustion images were taken at 9,000 fps, which is equivalent to 1° CA per image for an engine speed of 1500 rpm. 9,000 fps was too high to capture enough light for the injection images, so 3,000 fps was selected to achieve a reasonable balance between brightness and speed.

Combustion analysis was undertaken based on 60 cycles of cylinder pressure data. A typical cycle, which had the nearest IMEP value to the average IMEP, was selected for each run. Fig. 4.7 and Fig. 4.8 show 4 series of typical cycle images illustrating the process of injection and combustion for both injection modes with both fuels.

The nominal injection timings for triple injection were 300º, 290º, 280º bTDC with 280º bTDC for single injection. In reality, there was a 3-5º CA delay before the start of injection. The numbers labelled on the injection images represent the crankangle before combustion TDC at which the images were taken. The E10 spray was notably larger and of longer duration than the PURA spray for both single and triple injection cases, which may be attributed to the slightly increased quantity of fuel and the higher heat of evaporation of ethanol compared to PURA.

The combustion images shown in Fig. 4.8 were taken from 20º bTDC to 31º aTDC with 3º increments. The 'pink spots' in these images indicate the presence of soot in

the cylinder. By comparing the images for PURA and its E10 blend, one can see that the E10 blend produced much more soot within the cylinder than PURA. A slight reduction in soot presence was observed when the triple injection mode was used compared to the single injection mode.

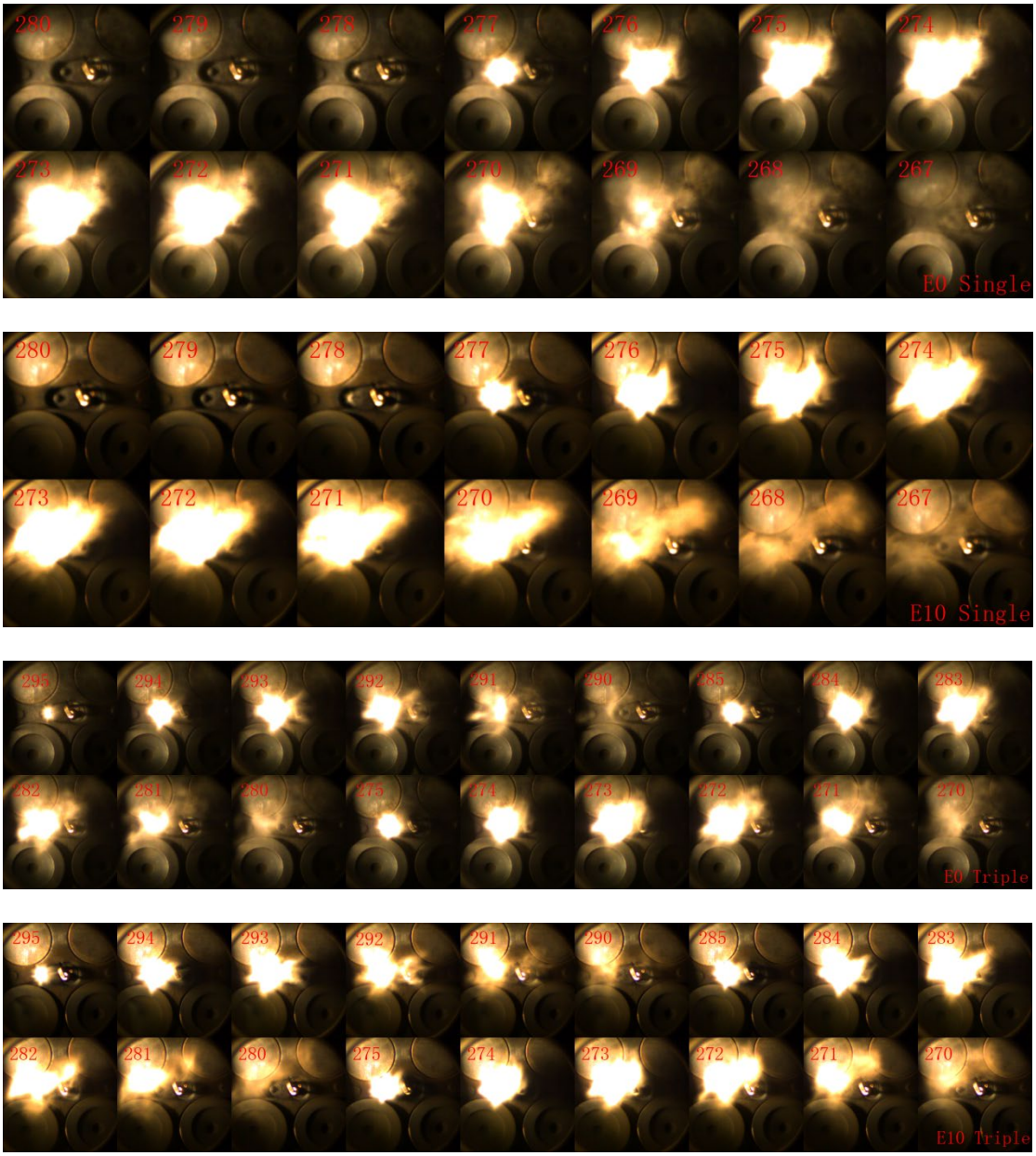

Fig. 4.7 *Injection images of 4 typical cycles: PURA Single (top), E10 Single, PURA Triple, E10 Triple (bottom), with the images at 1° CA increments starting at 280° CA (the nominal Start of Injection) for single injection cases and starting at 295° CA for triple injection cases.*

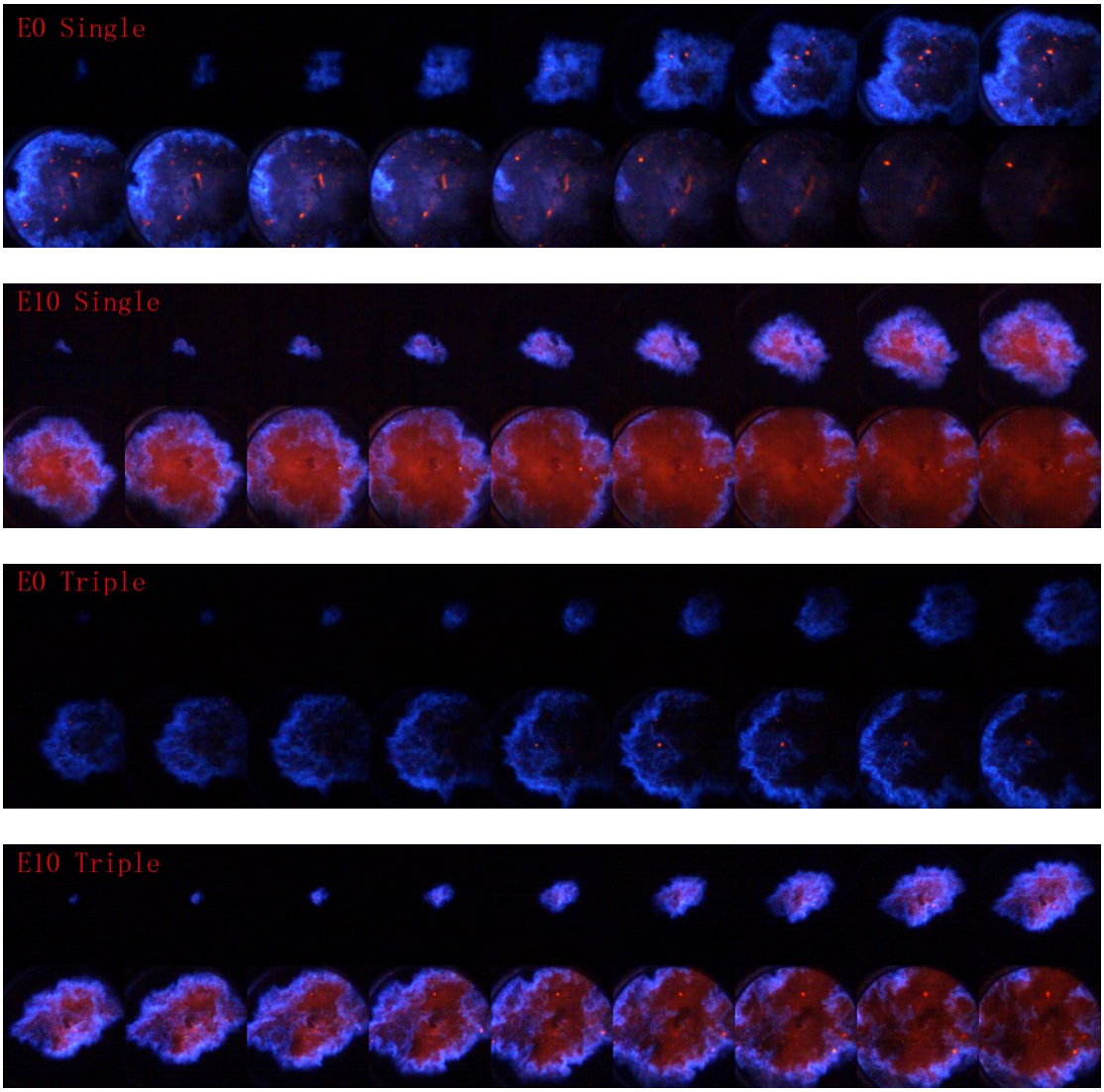

Fig. 4.8 *Combustion images of 4 typical cycles. The images had contrast and brightness enhancement to make the flame front more visible: Images taken from 20° bTDC to 31° aTDC with 3° CA increments.*

4.3.2 V8 Engine Tests Results

Test Sequence 2 - V8 injection timing sweep tests

The injection timing was swept from 120-360° bTDC in 30° increments on the V8 engine with PURA and PURA E10 stoichiometric mixtures. The exhaust sample was extracted upstream and downstream of a three-way catalyst and then analysed by the DMS500. By integrating the number and mass size-distributions, the total Pn and Pm

can be obtained for each operating point; Fig. 4.9 shows the results. The PM size and mass distributions from the V8 engine can be found in Figs. 5.6 – 5.9.

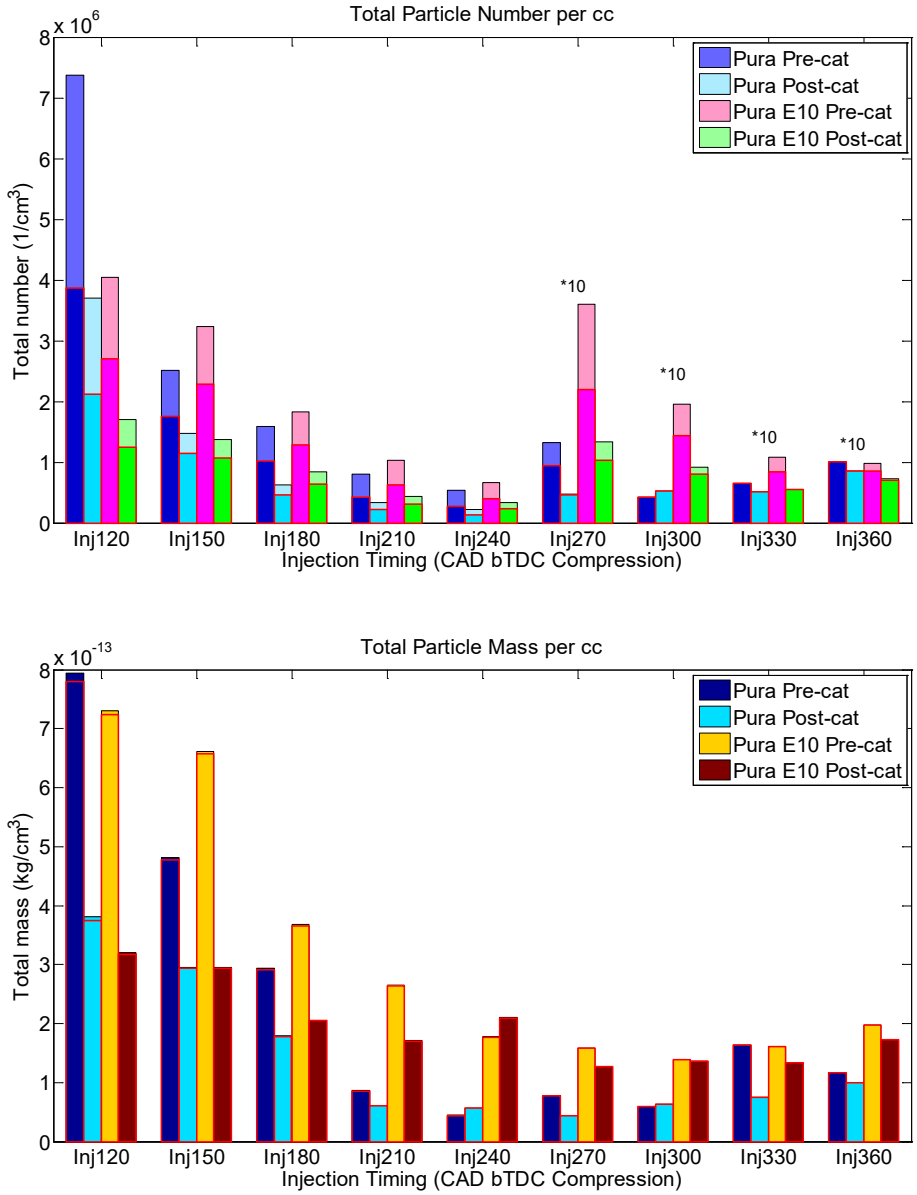

Fig. 4.9 *Total Pn (above) and Pm (bottom) at different injection timings for PURA and PURA E10 with the ignition timing of 35° bTDC (the red boxes contain data for particles that are larger than 23nm). Note: the change in (×10) scale for Pn with injection timing of 270 – 360° bTDC*

In general, retarding the injection timing increased both the total Pn and Pm. The trend for total Pn is monotonic and clearer than for total Pm. This is because retarding

the injection timing will shorten the time for mixture preparation and hence increase the likelihood of locally rich mixtures during combustion.

At late injection timings (120°, 150° bTDC), PURA E10 produced slightly less Pn and Pm than PURA. For the other injection timings, PURA E10 produced more Pn and Pm than PURA by up to about 3 times. It seems that at late injection timings PM emissions are primarily determined by the 'leaning effect' of the oxygen atoms present in PURA E10 (Hsieh *et al*., 2002) while at other early injection timings PM emissions are affected more by the difference in vaporization characteristics between PURA and PURA E10.

The pre-catalyst sample has higher Pn and Pm than the post-catalyst sample. Comparing the ratio between small and large particles on a number basis, it is fair to say that post-catalyst PM has a lower ratio than the pre-catalyst PM, and this implies that the catalyst had a reduction effect on the more volatile small particles. In order to quantify this reduction effect of the three-way catalyst on the PM emissions, the ratio between pre- and post-catalyst PM number concentrations were calculated and then plotted using a double-log scale with respect to the particle size as shown in Fig. 4.10. It is worth noting that the ratios for PM mass concentrations are the same as for number concentrations as the mass weighting factors are cancelled out when calculating the ratios at the same particle size.

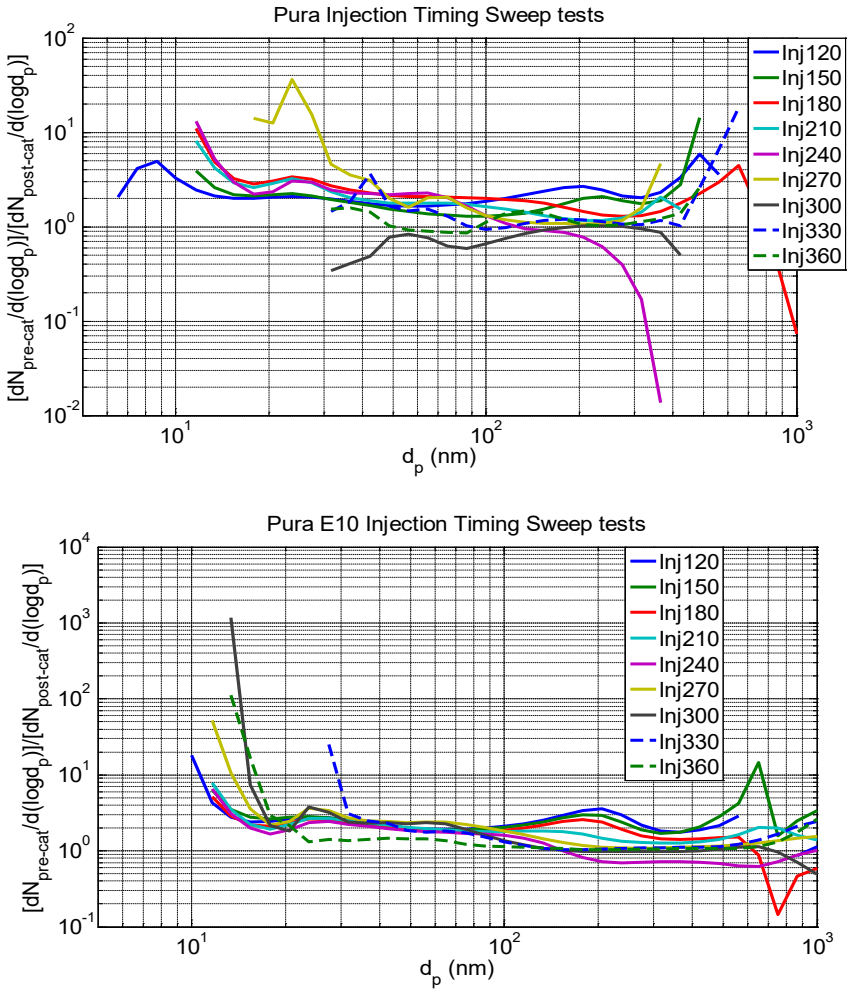

Fig. 4.10 *The PM ratios between pre- and post-catalyst samples at different injection timings with PURA (above) and PURA E10 (below)*

When the ratio is unity at a specific particle size, it means that there is no effect of the catalyst on PM emissions because the pre- and post-catalyst samples are identical in terms of Pn and Pm at that size. There is a reduction effect on PM emissions if the ratio is above 1 and an enhancement effect if the ratio is below 1.

Generally speaking, the catalyst exhibits a notable reduction effect on nucleation mode PM (smaller than 50 nm) whilst there is little effect on accumulation mode PM (50 – 200 nm). The trends at large sizes (larger than 200 nm) are unclear, presumably

because the absolute PM number concentrations measured by the DMS500 are too low to show any definite trends.

Test Sequence 3 - V8 ignition timing sweep tests

The ignition timing sweep tests (5-45° bTDC in 5° increments) on the V8 engine were with PURA and PURA E10. Pre- and post-catalyst samples were analyzed by the DMS500 for 2 minutes for each engine condition. Fig. 4.11 shows the results in terms of the total Pn and Pm. The PM size resolved spectra can be found in Figs. 5.6 – 5.9.

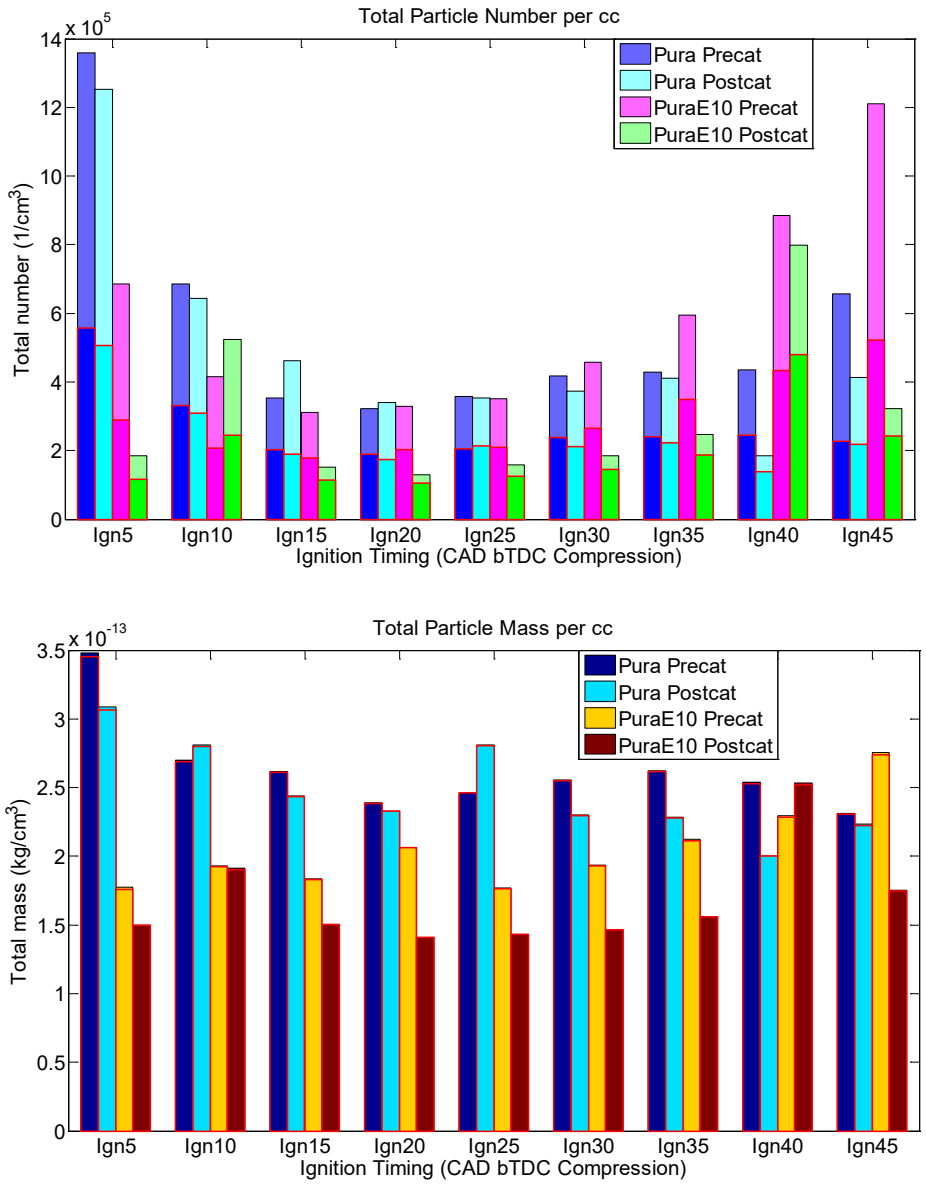

Fig. 4.11 *Total Pn (above) and Pm (bottom) at different ignition timings for PURA and PURA E10 with the injection timing of 280° bTDC (Red boxes contain data for particles that are larger than 23nm)*

There was a parabolic response of Pn to ignition timing with the lowest Pn being registered at an ignition timing of 20° bTDC. In contrast, the ignition timing has little influence on the Pm spectrum. Advancing the ignition timing from 20° bTDC resulted in a rise of Pn due to two combined effects: less time for fuel evaporation and less post-combustion oxidation of PM because of the lower in-cylinder temperatures.

Retarding the ignition timing from 20° bTDC might have led to poor combustion quality and thus more PM might have escaped oxidation.

Apart from a few exceptions, there are lower PM emissions post-catalyst than pre-catalyst in terms of total number and mass. Again, the ratio between the pre- and post-catalyst PM emissions were calculated and plotted versus the particle size as shown in Fig. 4.12.

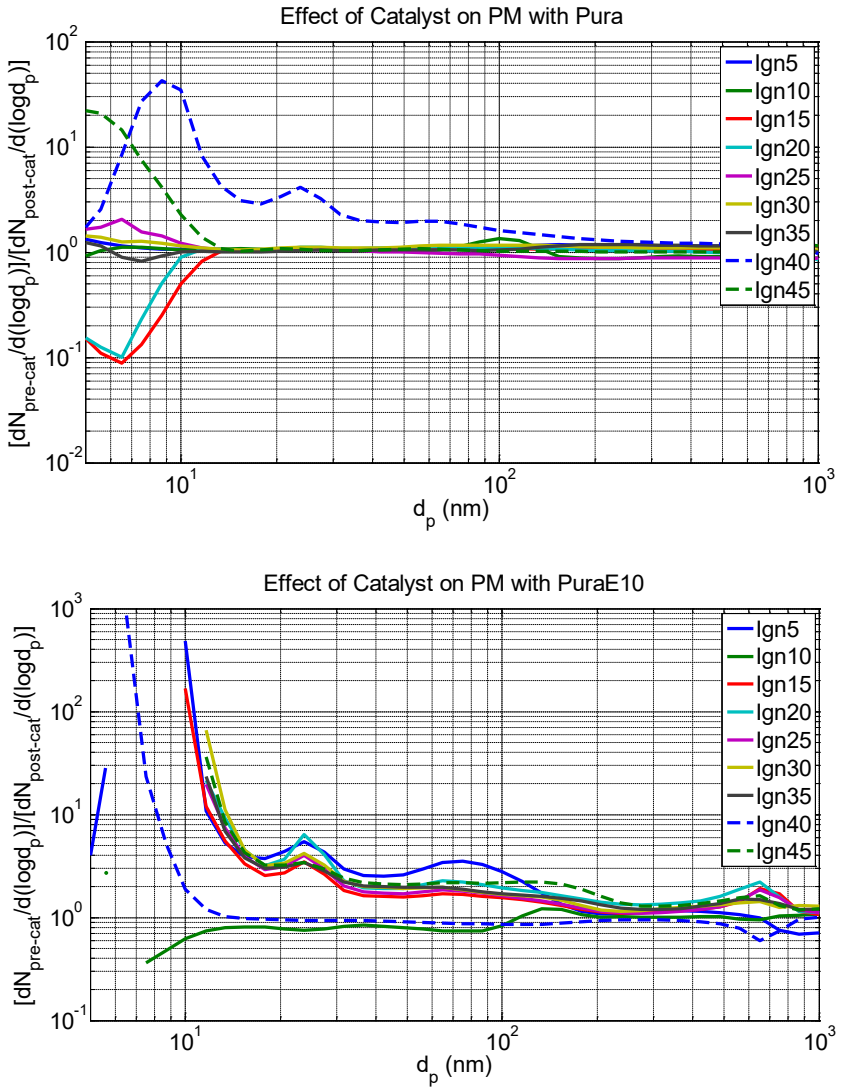

Fig. 4.12 *The PM ratios between pre- and post-catalyst samples at different ignition timings with PURA (above) and PURA E10 (below)*

A similar trend can be observed in Fig. 4.12 as in Fig. 4.10. That is, the catalyst primarily reduces the PM emissions at small sizes (below 50 nm), with little effect on large particles (larger than 50 nm). This trend is more clear when PURA E10 is used compared with PURA data. This implies that the catalyst is more prone to eliminate volatile species of PURA E10 generated PM than those of PURA generated PM.

4.4 Conclusions

- The V8 engine produced more stable PM emissions than the single cylinder engine, presumably because the optical engine has large crevice volumes. Therefore the trends found using the V8 engine are clearer than those from the single-cylinder engine for the same test procedure.
- PURA produced less PM emissions (both number and mass) than the toluene reference fuel (65% iso-octane - 35% toluene). It is postulated that the lower aromatic content of PURA could reduce the in-cylinder soot precursor and hence the PM emissions.
- Ethanol has a higher heat of evaporation than the base fuels, and more ethanol is needed to achieve stoichiometric combustion. This is qualitatively vindicated by comparing the injection images for PURA and PURA E10. These two physical effects make ethanol more prone to generate an inhomogeneous mixture at the start of combustion.
- Advancing the ignition timing from 25º to 45º bTDC increased both the PN and PM. This trend is applicable to both the V8 and the single-cylinder engine. Presumably it is the result of the combined effects of less time for fuel evaporation and a reduction in the post combustion oxidation. When the ignition timing was retarded from 20º to 5º bTDC, the PM emissions increased, and this may be attributed to the poor combustion performance with late ignition timings.
- With a few outliers, a generalization was made that advancing the injection timing during the intake stroke on the single-cylinder engine decreased both the Pn and Pm monotonically. The V8 PM emissions followed the same trend with no outliers. Advancing the injection timing increased the time for fuel evaporation and thus the homogeneity of the mixture was improved.

- The triple injection mode with PURA E10 produced slightly less Pn and Pm than the single injection mode. The images of combustion showed that PURA E10 had more soot present in the cylinder than PURA. Images of injection showed that PURA E10 had a larger spray area and took longer to evaporate than PURA. Similar results were found in the literature when ULG was used as the base fuel.
- The three-way catalyst on the V8 engine primarily reduced the volatile PM in the nucleation mode, with the accumulation mode PM being less affected.
- In terms of composition, the E10 blend produced a much higher carbonaceous content than its base fuel (65% iso-octane and 35% toluene). Little effect of ignition timing on PM composition was observed in this work.

5. Effects of Valve Timings and Coolant Temperature on Particulate Emissions in a GDI Engine

5.1 Introduction

Variable Valve Timing (VVT) technology has been widely used in modern spark-ignition engines for the optimization of torque delivery, and it allows obtaining combined internal EGR and Reverse Miller Cycle effects so to achieve a significant dethrottling at part load operation (Fontana *et al*., 2009). The use of the VVT strategy enables quick changes in the amount of trapped hot exhaust gases, i.e. internal exhaust gas recirculation (EGR), and is one promising way to control CAI (controlled auto-ignition) combustion (Milovanovic *et al*., 2004). The combustion process in Spark Ignition (SI) engines is strongly affected by the quality and quantity of the fluid within the cylinder at Intake Valve Closing (IVC). Residual gas affects the engine combustion processes (and therefore emissions and performance) through its influence on charge mass, temperature and dilution (Cavina *et al*., 2004). For a GDI engine, differing valve timings can also lead to significant changes in the gas exchange process and charge properties and therefore play a crucial role in combustion performance and particulate matter (PM) emissions.

It is conceivable that internal EGR, i.e. trapping the hot exhaust gases in the cylinder, would promote the spray break-up and evaporation and hence result in a higher mixture homogeneity, which is favourable for HC, PM emissions and combustion quality. But on the other side, high EGR could lead to a decrease in burning rate and thermal efficiency due to large residual gas fractions. The question as to which of

these competing effects would dominate in a DISI engine triggers the need for experimental and computational studies in this field.

Bai *et al*. (2010) found that in a GDI engine, internal EGR accomplished by NVO (negative valve overlap) can improve fuel economy and reduce BSFC (Break Specific Fuel Consumption) by 5-16% at part load. It was also found that CO, HC and NO_x emissions were all reduced when using internal EGR, especially for NO_x which decreased by more than 70%. Fontana *et al*. (2009) found that internal EGR achieved by retarding cam phaser positions at constant overlap can also improve thermal efficiency and reduce NO_x emissions, on the other side, it is necessary to employ charge motion optimization technology (valve masking) to improve the worsened combustion quality caused by high internal EGR fractions.

In this work, tests were performed using a Jaguar V8 SGDI engine for 4 different combinations of intake and exhaust valve timings. The primary objective of this study was to investigate the effects of valve timing on the characteristics of particulate emissions in a GDI engine, such as size/mass distributions and mass fractions in different volatility ranges. The influence of valve timing on the combustion stability was also studied.

5.2 Experimental Arrangement

5.2.1 Test Engine and Fuel

The test engine is a Jaguar 5L AJ133 V8 naturally aspirated engine with a homogeneous spray guided direct injection combustion system and four continuously

variable cam torque actuated cam phasing actuators. The engine specifications can be found in Section 2.2.

The engine is fitted with four cam torque actuated (CTA) VCT phasers and cam profile switching (CPS) technology. The inlet and exhaust camshaft VCT phasers are designed to provide 62 and 50 degrees of variable camshaft timing respectively (Sandford *et al*., 2009). This wide range of control results in high levels of internal exhaust gas recirculation (EGR) through wide positive valve overlaps at light to medium loads. The detailed cam timings are listed in Table 5.1.

Table 5.1 Cam timings of the test engine

	Inlet cam		Exhaust cam
	Low lift	High lift	
Total lift (mm)	5.5	10.53	9.36
Period (CAD)	210	250	250
VCT range (CAD)	62 Advance	62 Advance	50 Retard
	Baseline timing		
Valve opening	34 CAD aTDC	24 CAD aTDC	244 CAD bTDC
MOP	139 CAD aTDC	149 CAD aTDC	126 CAD bTDC
Valve closing	244 CAD aTDC	277 CAD aTDC	6 CAD aTDC

The valve timings in Table 5.1 are given with respect to crank angles after or before intake TDC. In this work, only the high lift cam profile was selected.

The base fuel used in this work is PURA, a gasoline provided by Shell. A detailed description of PURA in terms of its composition and distillation characteristics has been presented in Section 4.2. Apart from PURA, its 10% by volume ethanol blend was also used to examine the influence of ethanol addition on engine-out PM emissions. Some properties of pure ethanol were also presented in Section 4.2.

5.2.2 TGA Instruments and Test Method

Whatman^{TM} GF/A 47mm glass-fibre filters were used to sample the engine-out PM. The PM-laden filters were then analyzed by a Pyris 1 TGA from Perkin Elmer to examine the mass change of a sample as a function of temperature and time as it is subjected to a controlled temperature programme in a controlled atmosphere. An automatic gas switching unit called the Thermal Analysis Gas Station (TAGS) was used in conjunction with TGA to provide a programmable control of all gases used in the TGA, in this case, N_2 and air. The TAGS also controls the gas flow rate independent of the type of the gas. For all the TGA tests reported here, N_2 and air were used as inert gas and oxidizing gas at a constant flow rate of 20 ml/min.

A PC is connected to both TGA and TAGS via RS-232 cables to provide full control over both instruments using a programmable heating ramp procedure. The configuration of the TGA and its peripheral instruments is shown in Fig. 5.1.

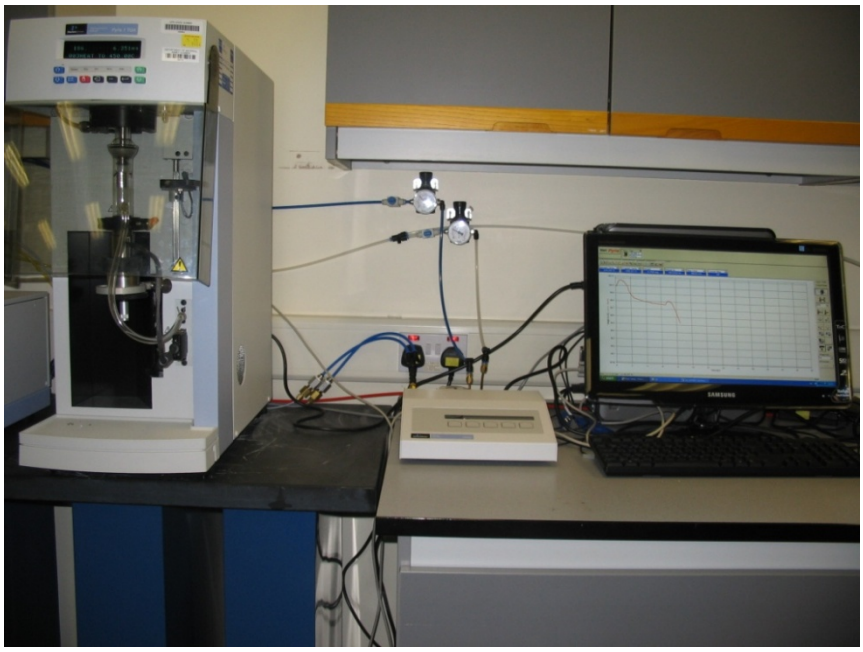

Fig. 5.1 Photograph of the Thermo-gravimetric Analyzer and its peripheral instruments

The pre-determined heating and gas switching program was kept unchanged throughout all the test runs. Fig. 5.2 illustrates the TGA heating and gas switching program used in this work.

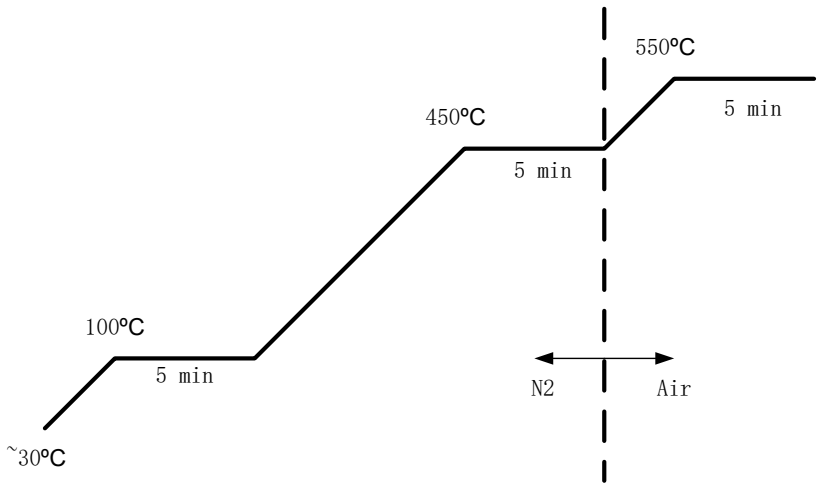

Fig. 5.2 *The Thermo-Gravimetric Analyzer (TGA) heating and gas switching programme*

As shown in Fig. 5.2, the heating programme starts under a nitrogen atmosphere at room temperature of around 30ºC and then holds at 100ºC for 5 minutes to ensure that any moisture is completely removed. And then there is another heating ramp to 450ºC which is followed by a 5 minute isothermal period. 450ºC was previously selected because it is high enough to assure the volatilization of the organic compounds (Lapuerta *et al*. 2007, Stratakis *et al.* 2003). After the isothermal process at 450ºC, the purge gas in the sample chamber is changed to air, meanwhile, the chamber is heated to 550ºC and the final temperature holds for 5 minutes to make sure that all the remaining soot has been oxidized.

An often cited concern of TGA is the influence of the temperature ramp rate on the mass loss results. To investigate any such influence, three different ramp rates were

selected, namely, 10, 20, 50 ºC/min for analyzing one single blank filter. The mass loss curves, together with a typical curve for a PM-laden filter, are shown in Fig. 5.3.

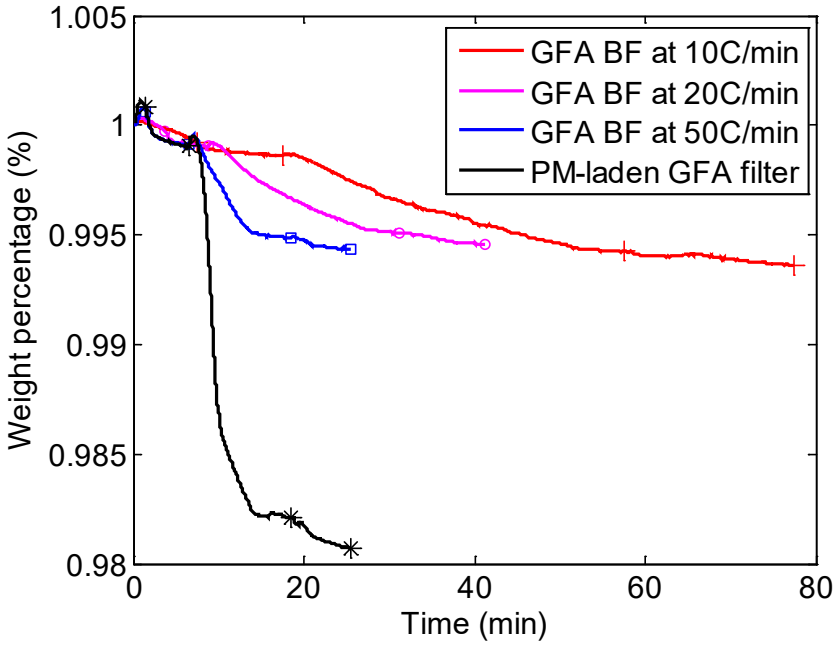

Fig. 5.3 *Thermo-Gravimetric Analysis (TGA) curves for a blank filter and a typical PM-laden filter with different ramp rates*

Four markers attached with each curve separate different regions according to volatility, and the weight percentage difference between two adjacent points represents the mass percentage of water fraction (WF), volatile organic fractions (VOF), and soot respectively. Table 5.2 summarizes the mass losses for the 4 curves.

Table 5.2 *The mass losses for a blank filter and a PM-laden filter at different heating rates (BF: Blank Filter; WF: Water Fraction; VOF: Volatile Organic Fraction.)*

	WF%	VOF%	SOOT%
GFA BF at 10ºC/min	0.139%	0.437%	0.064%
GFA BF at 20ºC/min	0.097%	0.394%	0.052%
GFA BF at 50ºC/min	0.089%	0.426%	0.050%
PM-laden filter	0.096%	1.692%	0.141%

The blank filter curves exhibit similar mass losses for VOF and soot regardless of the heating ramp rate. The difference between the three blank filter traces is negligible compared to the difference between the blank filter and the PM-laden one. Therefore, the highest ramp rate of 50ºC/min was selected for this study for the sake of saving time. The water fractions showed a larger variation. In fact, it is always the case that the percentage of water fraction was rather random for all the filters being examined. This is because moisture content is prone to be affected by handling and storage conditions after the engine experiments. In this work, only the ratio between VOF and soot by mass for the filter-borne PM has been taken into account.

The method for determining the VOF and soot mass percentage of the PM collected on the filters is described below. Some parameters discussed here are referred to in Fig. 5.4, which illustrates the scheme of the whole PM-laden filter area, denoted as S_1.

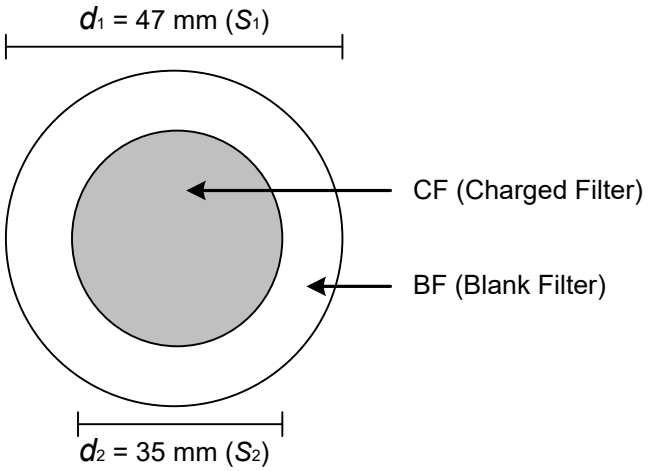

Fig. 5.4 Illustration of the PM-laden filter

S_2 refers to the inner portion of S_1 where the PM is collected. The diameters of S_1 and S_2 are 47mm and 35mm respectively. S_3, which is introduced into the TGA analysis,

is a small, unknown-sized portion of S_2. S_3 portions were cut from the particle-laden area (S_2) from different filters. T_0 refers to ambient temperature.

Some parameters which are initially known or can be calculated based on the given parameters prior to TGA experiments are listed as follows:

- d_1, d_2 and their corresponding areas S_1 and S_2 are initially known;
- $m_{\mathrm{BF,S1}}^{\mathrm{T0}}$, $m_{\mathrm{CF,S1}}^{\mathrm{T0}}$ i.e. the mass of the whole blank filter and the whole charged filter under ambient temperature, as they were measured with a microbalance before and after sampling each filter. $m_{\mathrm{PM,S1}}^{\mathrm{T0}}$ refers to the mass of PM collected on the filter and is the difference between $m_{\mathrm{BF,S1}}^{\mathrm{T0}}$ and $m_{\mathrm{CF,S1}}^{\mathrm{T0}}$;
- $m_{\mathrm{PM,S2}}^{\mathrm{T0}}$ is the same as $m_{\mathrm{PM,S1}}^{\mathrm{T0}}$ because there is no PM on the peripheral blank rims;
- $m_{\mathrm{BF,S2}}^{\mathrm{T0}}$ can be calculated from equation (5.1) assuming the mass is uniformly distributed on the blank filter;

$$m_{\mathrm{BF,S2}}^{\mathrm{T0}} = m_{\mathrm{BF,S1}}^{\mathrm{T0}} \times \frac{S_2}{S_1} \tag{5.1}$$

- $\mathrm{m}_{\mathrm{CF,S2}}^{\mathrm{T0}}$ can be obtained from equation (5.2),

$$m_{\mathrm{CF,S2}}^{\mathrm{T0}} = m_{\mathrm{BF,S2}}^{\mathrm{T0}} + m_{\mathrm{PM,S2}}^{\mathrm{T0}} \tag{5.2}$$

The above parameters are all based on the whole filter (S_1) and its PM-laden area (S_2), which can be obtained easily given the known area of S_1 and S_2 and initial mass weighed using a microbalance before and after each PM sampling test. However, the calculation of the mass parameters based on S_3 (a small portion of S_2 for TGA analysis) such as $m_{\mathrm{BF,S3}}^{\mathrm{T0}}$, $m_{\mathrm{PM,S3}}^{\mathrm{T0}}$ requires the TGA data because the cut area of S_3 is unknown.

In the TGA experiments, $m_{CF,S3}^{T}$ is continuously recorded under the pre-determined heating program, and its initial value is $m_{\mathrm{CF,S3}}^{\mathrm{T0}}$. Assuming that the PM is uniformly collected on S_2, $m_{\mathrm{PM,S3}}^{\mathrm{T0}}$ and $m_{\mathrm{BF,S3}}^{\mathrm{T0}}$ can then be calculated using equations (5.3) and (5.4) respectively. The right-hand part of both equations, namely $m_{\mathrm{PM,S2}}^{\mathrm{T0}}$, $m_{\mathrm{BF,S2}}^{\mathrm{T0}}$ and $m_{\mathrm{CF,S2}}^{\mathrm{T0}}$ have been already calculated in equations (5.1) and (5.2).

$$m_{\mathrm{PM,S3}}^{\mathrm{T0}}/m_{\mathrm{CF,S3}}^{\mathrm{T0}} = m_{\mathrm{PM,S2}}^{\mathrm{T0}}/m_{\mathrm{CF,S2}}^{\mathrm{T0}} \tag{5.3}$$

$$m_{\mathrm{BF,S3}}^{\mathrm{T0}}/m_{\mathrm{CF,S3}}^{\mathrm{T0}} = m_{\mathrm{BF,S2}}^{\mathrm{T0}}/m_{\mathrm{CF,S2}}^{\mathrm{T0}} \tag{5.4}$$

The main objective is to calculate the mass loss behaviour of the PM itself under the TGA heating program, i.e. $m_{\mathrm{PM,S3}}^{\mathrm{T}}$. Based on $m_{\mathrm{PM,S3}}^{\mathrm{T}}$, the ratio between VOF and soot mass fractions can be easily obtained using equation (5.5):

$$m_{\mathrm{VOF}}^{\mathrm{T}}/m_{\mathrm{SOOT}}^{\mathrm{T}} = \left(m_{\mathrm{PM,S3}}^{\mathrm{T0}} - m_{\mathrm{PM,S3}}^{\mathrm{T=450}}\right)/\left(m_{\mathrm{PM,S3}}^{\mathrm{T=450}} - m_{\mathrm{PM,S3}}^{\mathrm{T=550}}\right) \tag{5.5}$$

In which, $m_{PM,S3}^{T=450}$ is the PM mass at the end of the isothermal phase of 450ºC as shown in Fig. 5.2 ,while $m_{PM,S3}^{T=550}$ is the PM mass at the end of the isothermal phase of 550ºC. In order to calculate $m_{PM,S3}^{T}$, equation (5.6) can be used.

$$m_{PM,S3}^{T} = m_{CF,S3}^{T} - m_{BF,S3}^{T} \tag{5.6}$$

So far, the only unresolved parameter is $m_{BF,S3}^{T}$. It consists of two parts: the initial mass $m_{BF,S3}^{T0}$ and its following mass loss behaviour. The initial mass $m_{BF,S3}^{T0}$ can be obtained using equation (5.4), which requires equations (5.1) and (5.2) to be solved first. In terms of the mass loss behaviour for the blank filter, two methods could be used to determine it. The first method is using the average behaviour of a batch of blank filters as a reference behaviour. However, the variation of the mass loss traces for 7 blank filters tested in this work is so large that a second method was used. The second method uses the peripheral blank rim to obtain a representative mass loss behaviour for each sample filter being examined. This method is believed to be more precise than the first one because the filter composition is believed to be identical for the whole filter area (including the central area and the rim). Therefore, the second method was used to obtain the results presented in Section 5.3.3.

5.2.3 Test Matrix

4 sets of engine tests were conducted using PURA and PURA E10 with the coolant temperature being 20ºC for the cold condition and 90ºC for the warm condition. For each set of tests, 4 different combinations of intake and exhaust valve timings were

selected and they are termed: VVT1, VVT2, VVT3 and VVT4. Table 5.3 summarizes the test matrix.

Table 5.3 Test Matrix

Test sequence	1	2	3	4
Fuel	PURA	PURA	PURA E10	PURA E10
Speed (rpm)	1500	1500	1500	1500
Torque (Nm)	92	92	92	92
Fuel Pressure (bar)	150	150	150	150
Injection Timing (ºCA bTDC)	280	280	280	280
Ignition Timing (MBT) (ºCA bTDC)	30-40	30-40	30-40	30-40
Relative AFR	1	1	1	1
High lift cam timings	VVT1,2,3,4	VVT1,2,3,4	VVT1,2,3,4	VVT1,2,3,4
Coolant Temperature (ºC)	20	90	20	90

The 4 valve timing combinations are illustrated in Fig. 5.5. VVT1 was the baseline timing. VVT2 had the same exhaust valve timing as VVT1 whilst the intake valve timing was advanced 50 CAD. VVT3 had 50 CAD advanced intake valve timing and 20 CAD retarded exhaust valve timing compared to the baseline timing. VVT4 had 20 CAD retarded exhaust valve timing whilst the intake valve timing is the same as the baseline timing.

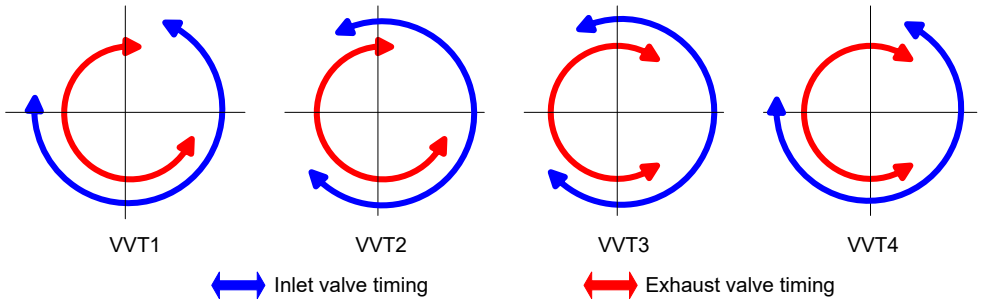

Fig. 5.5 Four different high lift cam valve timings

Details of the VVT combinations with respect to intake TDC are given in Table 5.4.

Table 5.4 Four VVT timings with respect to intake TDC

	IVO (ºaTDC)	IVC (ºaTDC)	EVO (ºbTDC)	EVC (ºaTDC)	Changes from baseline timing	Overlap (º CA)
VVT1	24	274	244	6	Baseline timing	-18
VVT2	-26	224	244	6	50º Inlet adv.	32
VVT3	-26	224	224	26	50º Inlet adv. and 20º Exhaust Ret.	52
VVT4	24	274	224	26	20º Exhaust Ret.	2

5.3 Results and Discussion

5.3.1 PM number and mass concentrations measurement using the DMS500

Number concentrations normalized with the differential interval of the logarithm of particle size were automatically derived from the DMS500 electrometer currents. The DMS500 software uses a specially written Bayesian statistical algorithm to generate two lognormal distribution fitting spectra, which are meant to represent the nucleation mode and the accumulation mode with no clear cut-off size in between. PM mass concentrations were derived from PM number concentrations using a PM density model, which is defined by Equation 2.9.

Fig. 5.6 shows the PM number concentrations and mass concentrations for the first set of tests, i.e. PURA tests with coolant temperature of 20ºC.

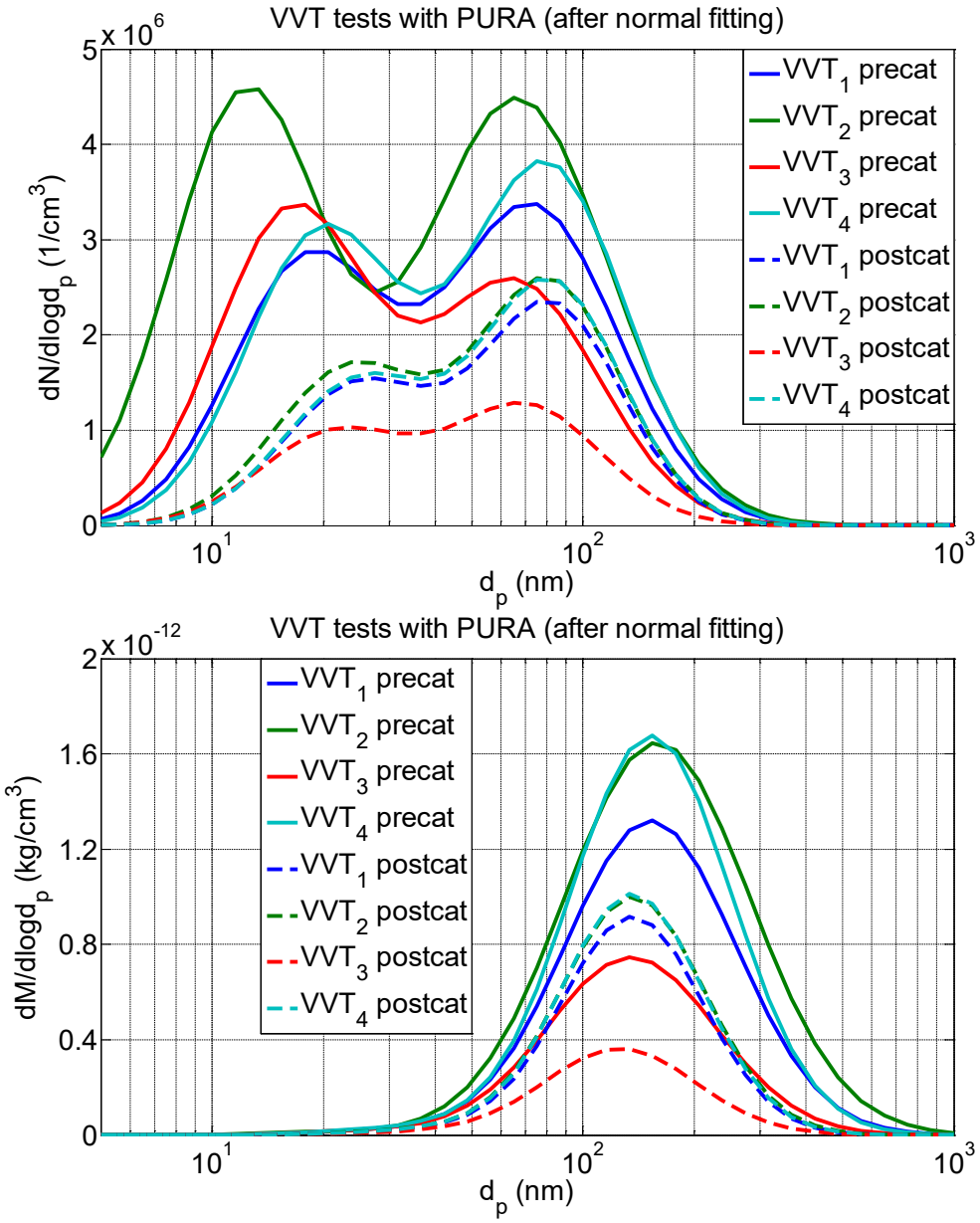

Fig. 5.6 *Size resolved number concentrations (above) and mass concentrations (below) of PM emissions at different valve timings (defined in Table 5.4) using PURA with a coolant temperature of 20 ℃*

At each valve timing combination, both pre- and post-catalyst samples were measured by the DMS500. In Fig. 5.6, solid lines are for the pre-cat data while broken lines are for the post-cat data. Compared to the pre-cat PM samples, the post-cat samples exhibited a significant reduction in both the PM number concentrations and mass

concentrations, especially for the nucleation mode PM which has a particle size of less than 50 nm.

For the number spectra, the pre-cat samples showed clear bi-lognormal spectra characteristics whilst the post-cat samples had more accumulation PM than nucleation PM. This indicates that the catalyst reduced the nucleation mode PM to a larger extent than it did the accumulation mode PM. For the mass spectra, the peak positions are for much larger size particles than on the number spectra. It is invariably the case that PM in the accumulation mode (>50nm), despite the low number concentration, can still dominate the mass weighted distributions.

In general, compared to the baseline (VVT1), VVT2 and VVT4 had a larger PM emissions on both a number and a mass basis whilst VVT3 decreased PM number and mass concentrations.

Fig. 5.7 shows the results for the second set of PURA tests with coolant temperature being 90ºC.

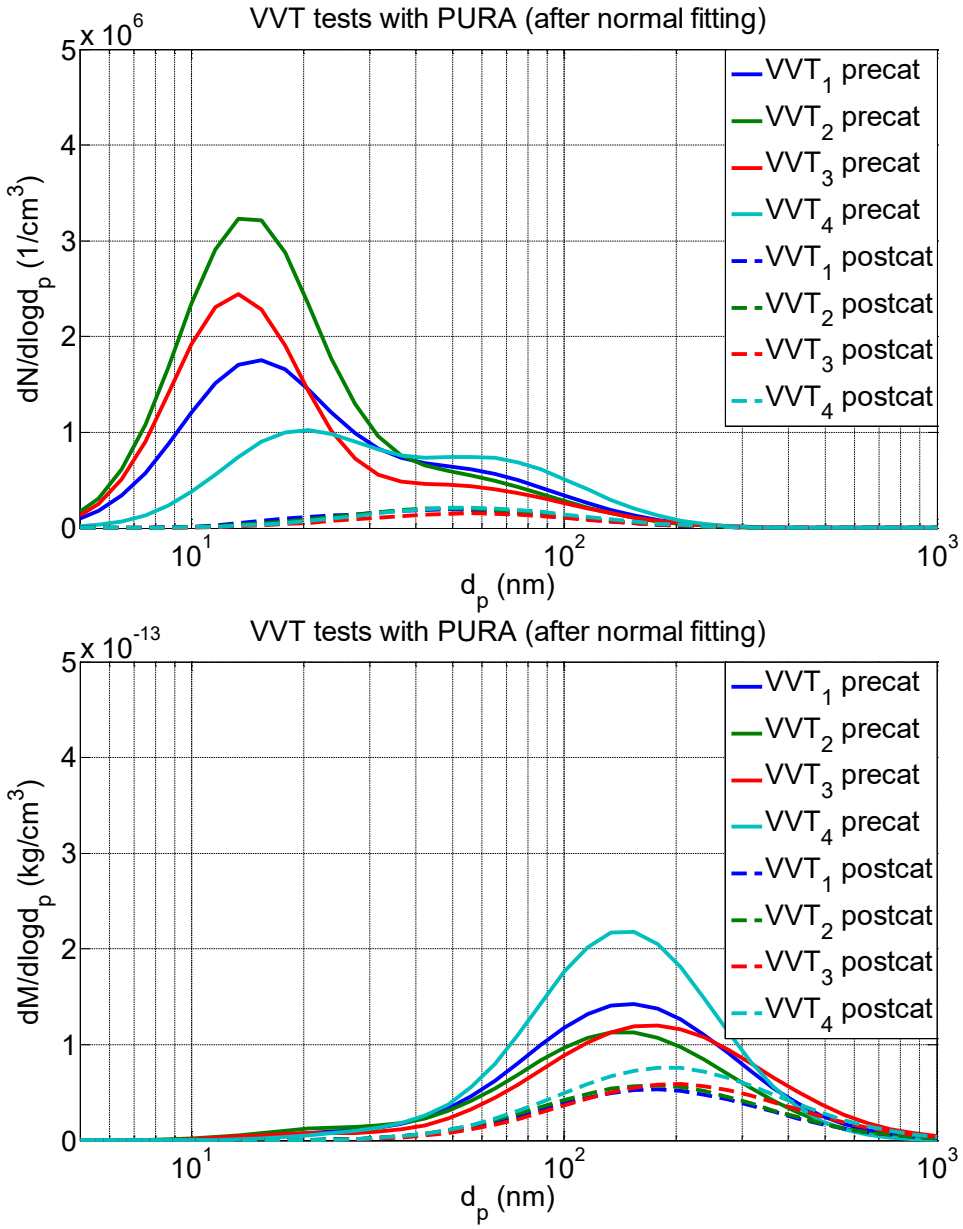

Fig. 5.7 *Size resolved number concentrations and mass concentrations of PM emissions at different valve timings (defined in Table 5.4) using PURA with a coolant temperature of 90℃*

For the number spectra, the nucleation mode again dominates over the accumulation mode. For post-catalyst samples, the nucleation PM can be barely detected, and this maybe because the higher exhaust temperatures under warm operation conditions increased the removal efficiency of the catalyst for the nucleation mode PM. For the mass spectra, the accumulation mode dominates in all cases.

By comparing Fig. 5.6 and Fig. 5.7, it can be seen that the PM emissions under warm engine conditions are significantly less than those under cold engine conditions in terms of both number and mass concentrations by approximately an order of magnitude. It is because the spray disperses more under warm conditions than under cold conditions, which in turn will lead to better mixture homogeneity and combustion stability for the warm engine. As a result, the PM emissions decreased markedly when the coolant temperature increased from 20ºC to 90ºC.

Fig. 5.8 shows the results for the third set of PURA E10 tests under cold conditions (coolant 20ºC).

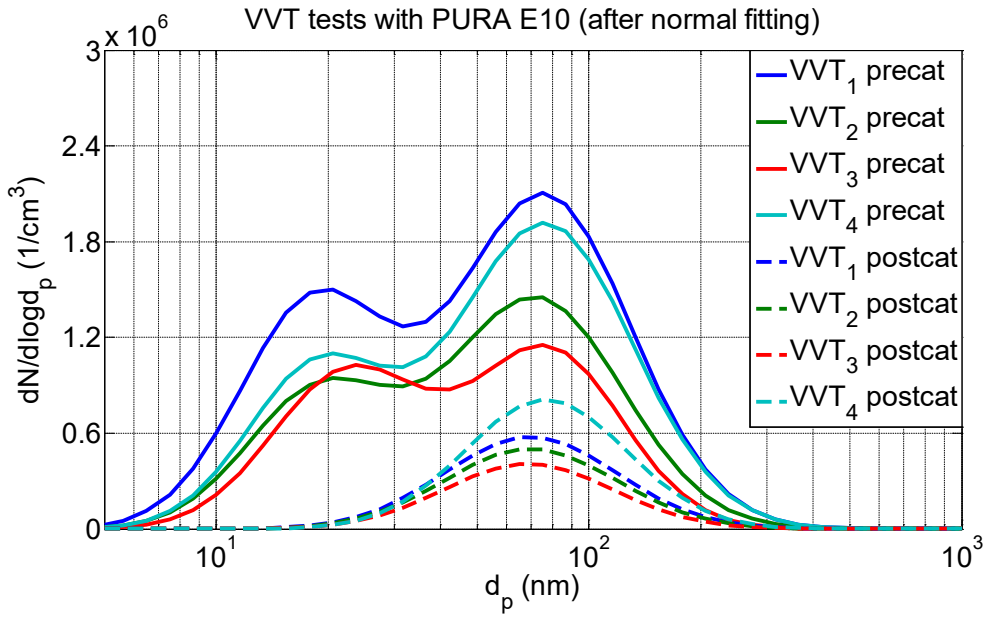

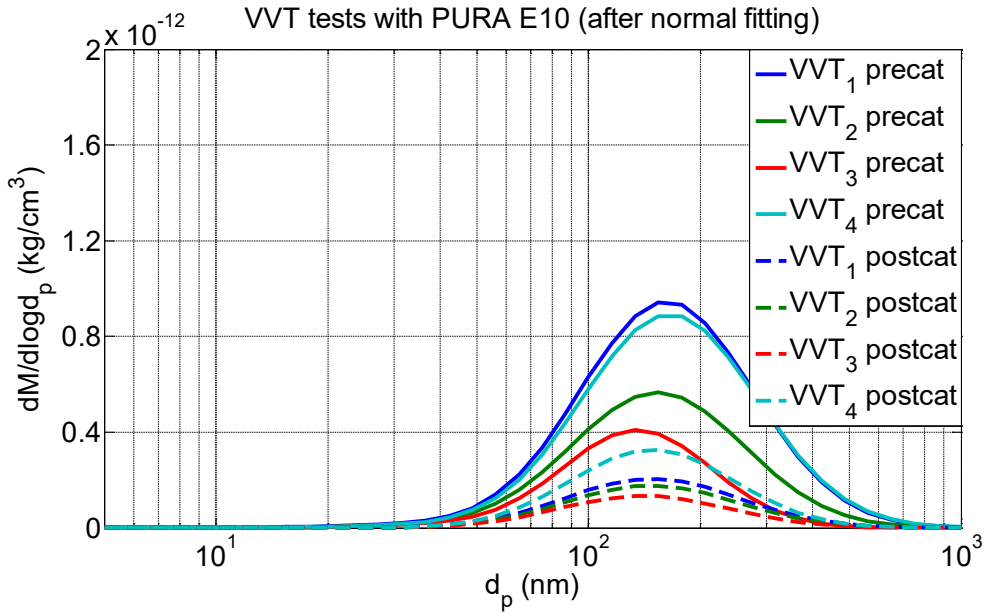

Fig. 5.8 *Size resolved number concentrations and mass concentrations of PM emissions at different valve timings (defined in Table 5.4) using PURA E10 with coolant temperature of 20ºC*

In Fig. 5.8, there are clear bi-lognormal spectra characteristics for the pre-cat samples number spectra whilst no obvious nucleation mode is present for the post-cat samples. This indicates a high particle removal efficiency by the catalyst for the nucleation mode PM. Accumulation mode PM dominates the mass spectra with little nucleation mode PM being detected.

Compared to the cold coolant PURA tests data presented in Fig. 5.6, adding 10% by volume ethanol seems to have reduced both PM number and mass concentrations by about 2-3 times. It is presumably because the presence of oxygen atoms in the ethanol molecule improves the oxidation of locally rich mixtures or droplets, and hence reduces the in-cylinder PM emissions for cold engine conditions.

Fig. 5.9 shows the fourth set of tests data, in which PURA E10 was used with the coolant temperature being 90ºC.

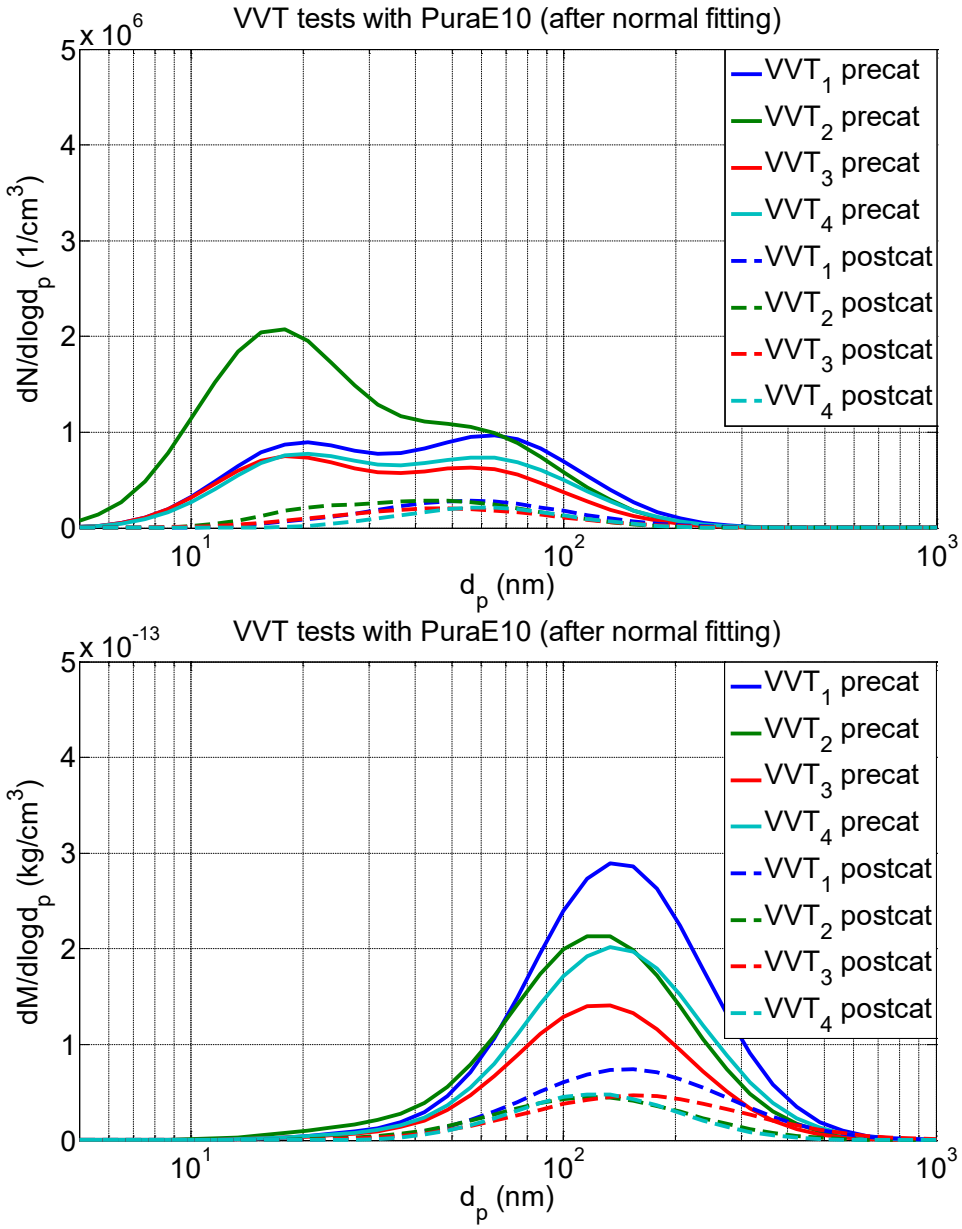

Fig. 5.9 Size resolved number concentrations and mass concentrations of PM emissions at different valve timings (defined in Table 5.4) using PURA E10 with coolant temperature of 90ºC

The number spectra and mass spectra in Fig. 5.9 are broadly similar to those in Fig. 5.7 when PURA was used under warm engine conditions. However, adding 10%

ethanol seems to have increased the PM mass for most cases. One possible reason is that PURA E10 has a higher enthalpy of vaporization than PURA under warm engine conditions, and it will lead to greater mixture inhomogeneity and hence higher PM emissions in terms of both number and mass.

By integrating the number and mass size-distributions, the total particle number (Pn) and total particle mass (Pm) can be obtained for each operating point. Fig. 5.10 summarizes the total Pn and Pm emissions for the pre-catalyst samples for all four sets of tests.

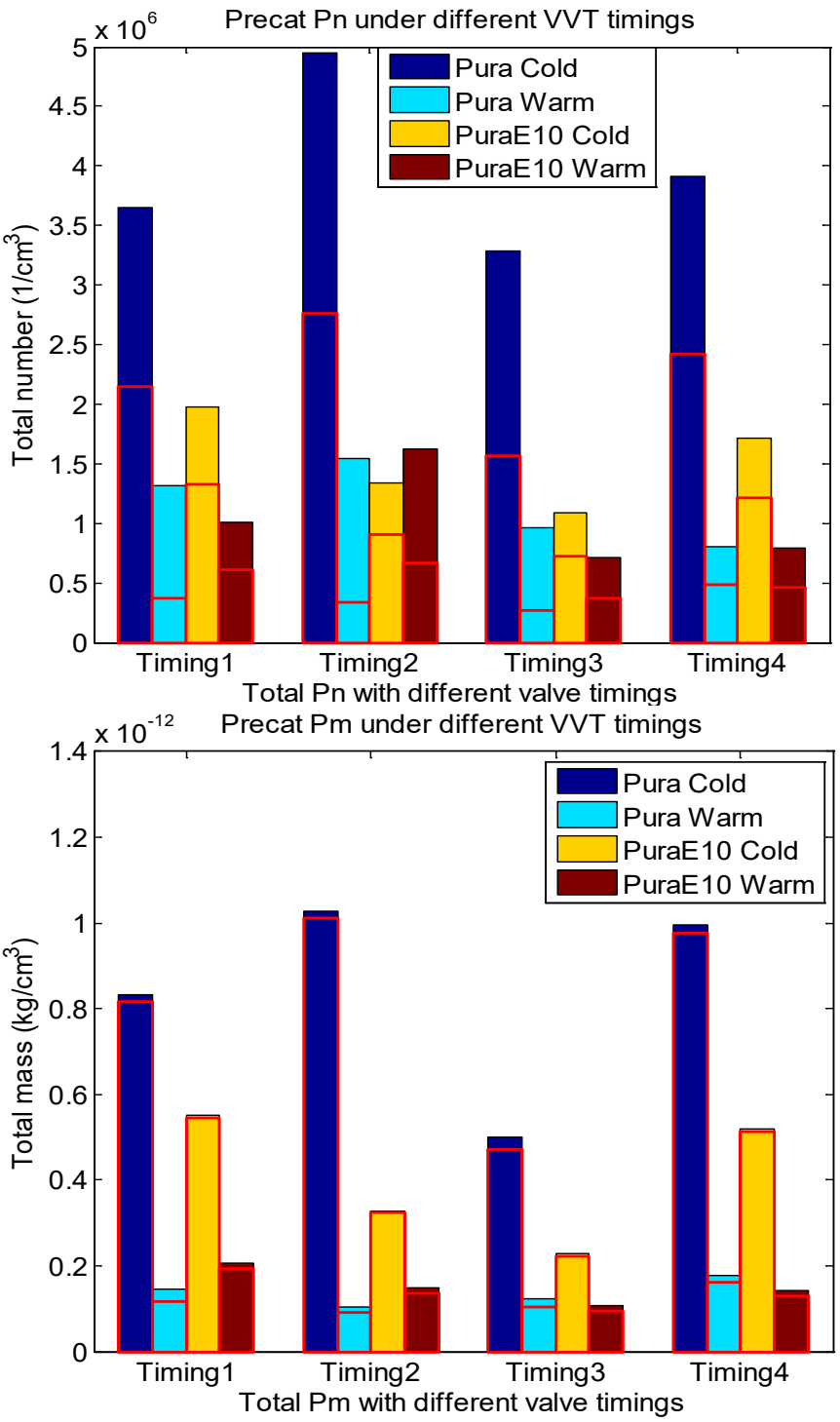

Fig. 5.10 *Total Pn and Pm of pre-cat samples at different valve timings (defined in Table 5.4) for PURA and PURA E10 under cold (Coolant, 20ºC) and warm (Coolant, 90ºC) conditions. Note: the red boxes contain data for particles that are larger than 23nm.*

Apart from the whole size range data, data above 23nm were calculated and plotted within red boxes in Fig. 5.10. The truncated data replicate the test procedure proposed

by the EU PMP program, which specifies that a volatile particle remover is used to remove sub-23nm particles, as particles at such small sizes tend to be very susceptible to variations in dilution profiles and sampling conditions. In order to improve the repeatability and reproducibility of number-based PM measurements, the particles smaller than 23nm were deliberately eliminated. It is believed that the gas-to-particle conversion and adsorption of volatile particles had little effect on PM size distributions at the dilution ratio of 10 used in this work as a result of low saturation ratio. In addition, the DMS500 has a relatively higher noise to signal ratio for sub-23nm PM measurement than for larger sized PM measurements, which could make the truncated data more robust and reliable than the whole size range data.

From Fig. 5.10, the following observations can be made:

- The sub-23nm particles contributed significantly to the total Pn whilst very little to the total mass;
- In general, the cold engine produced higher total Pn than the warm engine by a factor of 2-6, and higher total Pm by a factor of 3-7;
- Under cold engine conditions, adding 10% by volume ethanol led to a reduction in both total Pn and Pm by a maximum of 3. On the contrary, adding ethanol led to a slight increase in total Pn and Pm by a maximum of 2 under warm engine conditions;
- VVT3 produced the lowest total Pn and Pm among the 4 valve timing combinations for all the 4 sets of tests. VVT2 produced the second lowest total Pn and Pm except for PURA cold data. VVT1 and VVT4 produced broadly similar PM emissions. This might be because that VVT3 and VVT2 had

relatively large valve overlaps and hence more residual gas fraction would have been trapped in the cylinder, which will improve fuel spray atomization. The implications will be discussed in the following section.

Fig. 5.11 shows the total Pn and Pm of post-catalyst samples for all the 4 sets of tests.

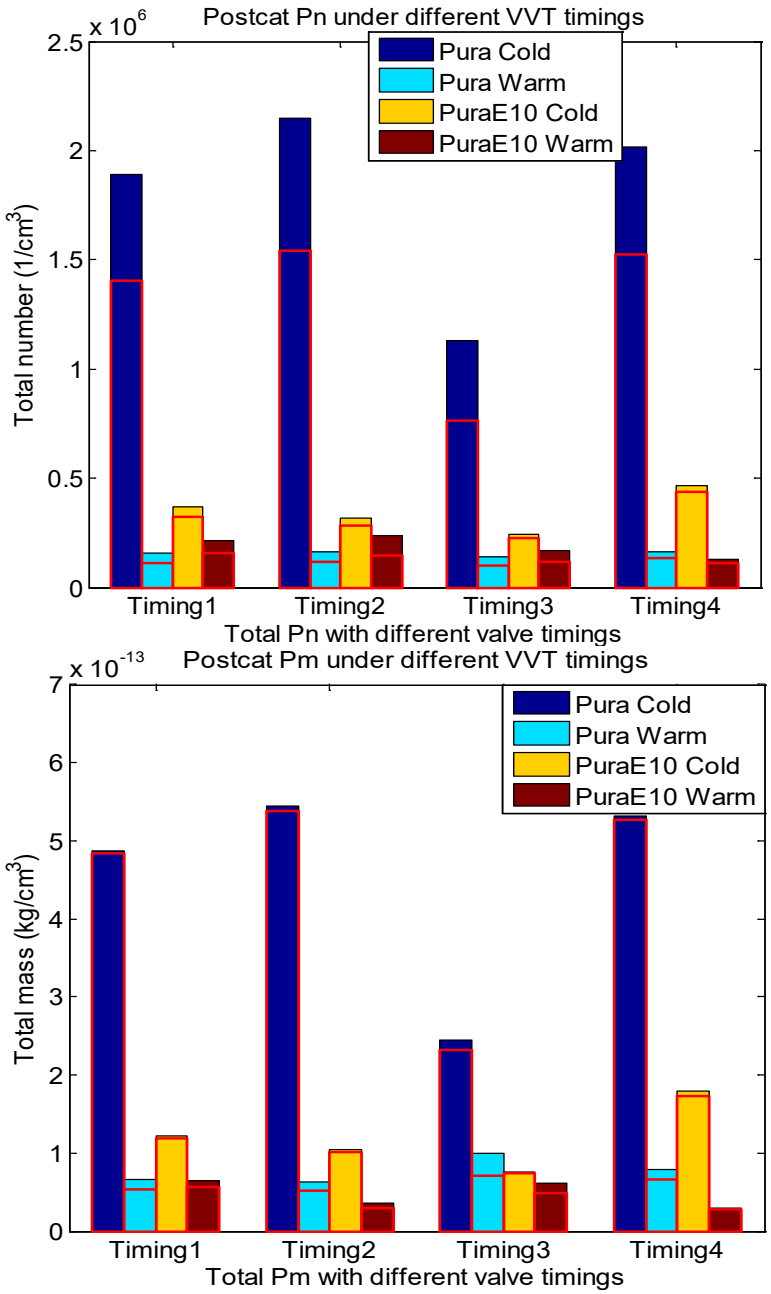

Fig. 5.11 Total Pn and Pm of post-cat samples at different valve timings (defined in Table 5.4) for PURA and PURA E10 under cold (Coolant, 20°C)

and warm (Coolant, 90ºC) conditions. Note: the red boxes contain data for particles that are larger than 23nm.

The key findings for the post-cat results in Fig. 5.11 are:

- The sub-23nm particles accounts for little of the total Pm. Apart from PURA cold data, the sub-23nm particles also account for a small proportion of the total Pn. This implies that the catalyst reduces the nucleation mode PM to a larger extent than it did the accumulation mode PM;
- The cold engine produced higher total Pn and Pm for post-cat PM samples than the warm engine by up to an order of magnitude;
- Under cold engine conditions, adding 10% by volume ethanol led to a significant reduction in both total Pn and Pm by a maximum of 5, Whilst the influence of ethanol addition on post-cat PM emissions is less clear under warm conditions;
- Like the pre-catalyst results, VVT3 also produced the lowest total Pn and Pm among the 4 different valve timing combinations; it will be seen in Section 5.3.2 that VVT3 had the highest level of exhaust residuals;
- The total Pn and Pm for post-cat emissions are roughly half those of the pre-cat samples.

5.3.2 Computational results of in-cylinder gas temperature and internal EGR rate

Valve timings may well affect the in-cylinder gas temperature and residual gas fraction trapped in the cylinder through their influence on the gas exchange process. The charge temperature on compression will provide an indication of the energy available for fuel vaporization, and this will affect the mixture homogeneity which

plays a crucial role in PM formation in SGDI engines. Since the charge temperature is primarily determined by the mass fraction of the residuals trapped in the cylinder, it is therefore desirable to assess the in-cylinder gas temperature and the mass fraction of residuals at different valve timing strategies. The gas exchange process is often coupled with rather complicated mechanisms such as the ram effect (the inertia of the gas in the intake system as the intake valve is closing increases the pressure in the port and continues the charging process as the piston slows down around BDC and starts the compression stroke) and reverse flow into the intake as a consequence of the inlet valve closing after compression BDC (Heywood, 1988), therefore, simulation is almost a necessity for estimating the gas exchange process to predict the internal EGR levels and the gas temperature history.

Simulation work was conducted by Jaguar using Ricardo Ltd WAVE, a 1D engine and gas dynamics simulation software (http://ricardo.com/Software/Products/WAVE/), coupled to a sophisticated fuel injection and vaporization model to provide simulations of the charge temperature and residual mass fraction for the experimental tests. Input parameters for the modelling such as air inlet temperature, manifold air pressure, ambient barometric pressure, ignition and injection timings were obtained from the experimental data. In order to give the best in-cylinder gas temperature prediction, the modelling work was processed to match the manifold pressure under different valve timings (so there may be a slight difference in load) using indolene as the fuel. The differences within the simulated results could provide explanations for the differences in PM emissions between the different valve timing strategies.

Fig. 5.12 shows the simulated in-cylinder gas temperature traces for the different valve timings under cold and warm engine conditions. The temperature traces during the late compression phase are enlarged.

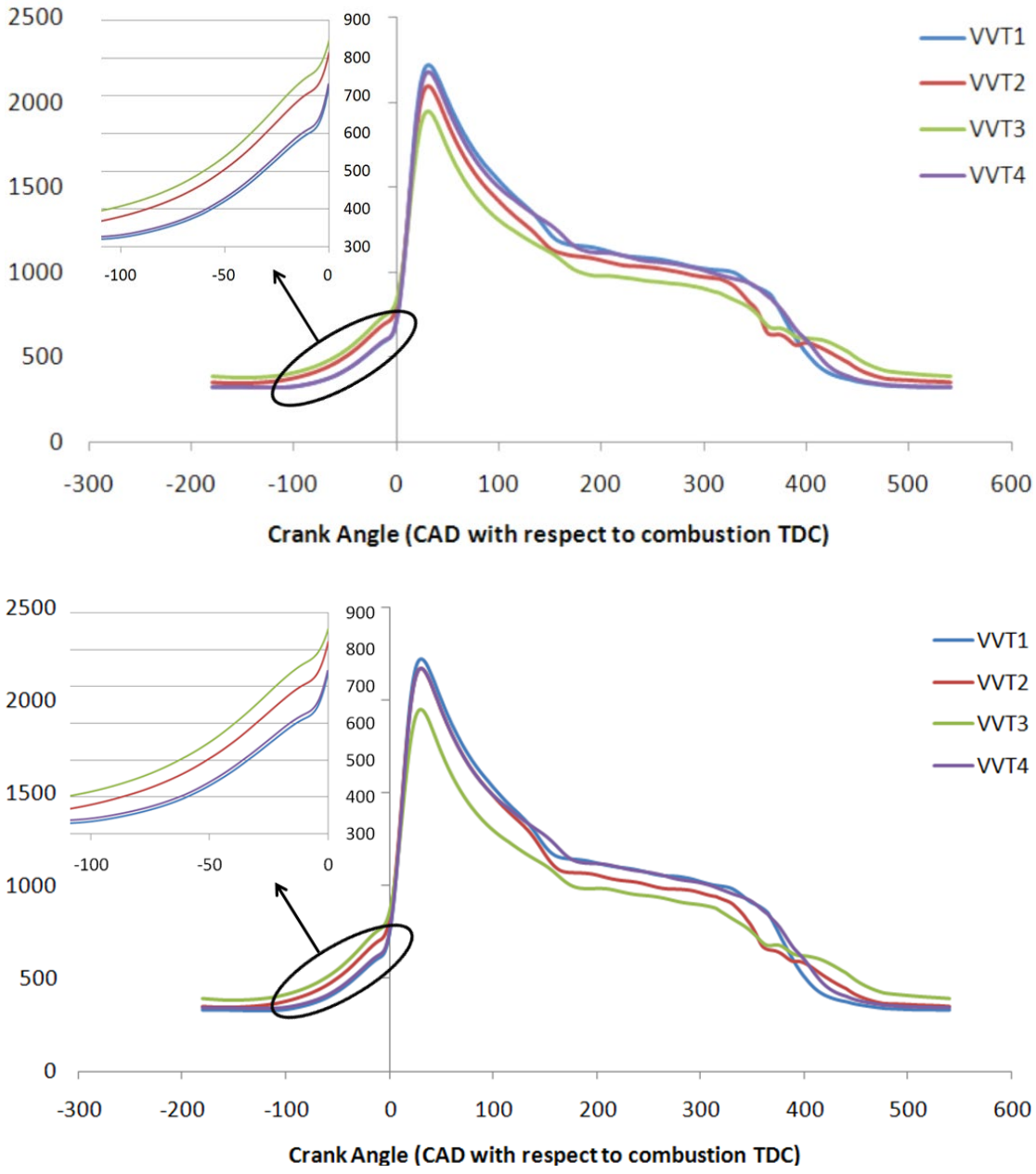

Fig. 5.12 Simulated in-cylinder gas temperature traces for different valve timings under cold (above) and warm (below) conditions

Table 5.5 summarizes the simulated results for the mass fraction of residuals after the intake valve closing (IVC) and before ignition.

Table 5.5 Mass fraction of residuals for different valve timings under cold (20ºC) and warm (90ºC) conditions

VVT timings	MFR under cold condition	MFR under warm condition
VVT1	9.7%	9.4%
VVT2	22.2%	17.1%
VVT3	33.8%	33.1%
VVT4	13.4%	13.6%

From Fig. 5.12 and Table 5.5, it can be seen that for both cold and warm conditions the descending order for the internal EGR rate or residual mass fraction is VVT3, VVT2, VVT4 and VVT1. As a result of the highest EGR rate, VVT3 exhibits the highest gas temperature on compression, followed by VVT2 which had a lower gas temperature by approximately 50ºC. VVT1 and VVT4 showed similar temperature traces which were lower than VVT2 by approximately 100ºC.

By inspecting the valve timings at different valve timing strategies as shown in Table 5.4, it is fair to say that the residual mass fraction and the in-cylinder gas temperature on compression rise as the positive valve overlap increases. This positive relationship between the level of residuals and the valve overlap can be found elsewhere in the literature (Stone, 1999). It is presumably because as the valve overlap increases, more residual gases will be pushed into the intake port compared to the exhaust port (because of the lower pressure in the intake port), hence more residual gases will be inducted back into the cylinder during the ensuing intake stroke. The gas temperature on compression gives indications of the heat energy available for fuel spray atomization, which is crucial in determining the mixture homogeneity and hence the

PM emissions. Inspection of total Pn and Pm for pre-cat PM samples in Fig. 5.10 demonstrates that higher gas temperature generally leads to lower total Pn and Pm due to the higher heat energy of residual gas promoting fuel vaporization.

VVT3 showed the highest gas temperature on compression, but its peak temperature during combustion is the lowest among all the valve timing strategies. This is because the highest EGR rate leads to the lowest peak temperature and peak pressure and this normally reduces the combustion quality and stability. Stone (1999) also pointed out that high levels of exhaust residuals trapped in the cylinder lead to greater cycle-by-cycle variations in combustion and lower NO_x emissions, presumably due to lower peak temperature (Stone, 1999). To verify this, the CoVs (Coefficient of Variance) of IMEP were calculated based on the experimental data and these are presented in Fig. 5.13. In general, the descending order for the CoV of IMEP is VVT3, VVT2, VVT4 and VVT1, which is consistent with the results for mass fraction of residuals and gas temperature on compression as shown in Fig. 5.12 and Table 5.5.

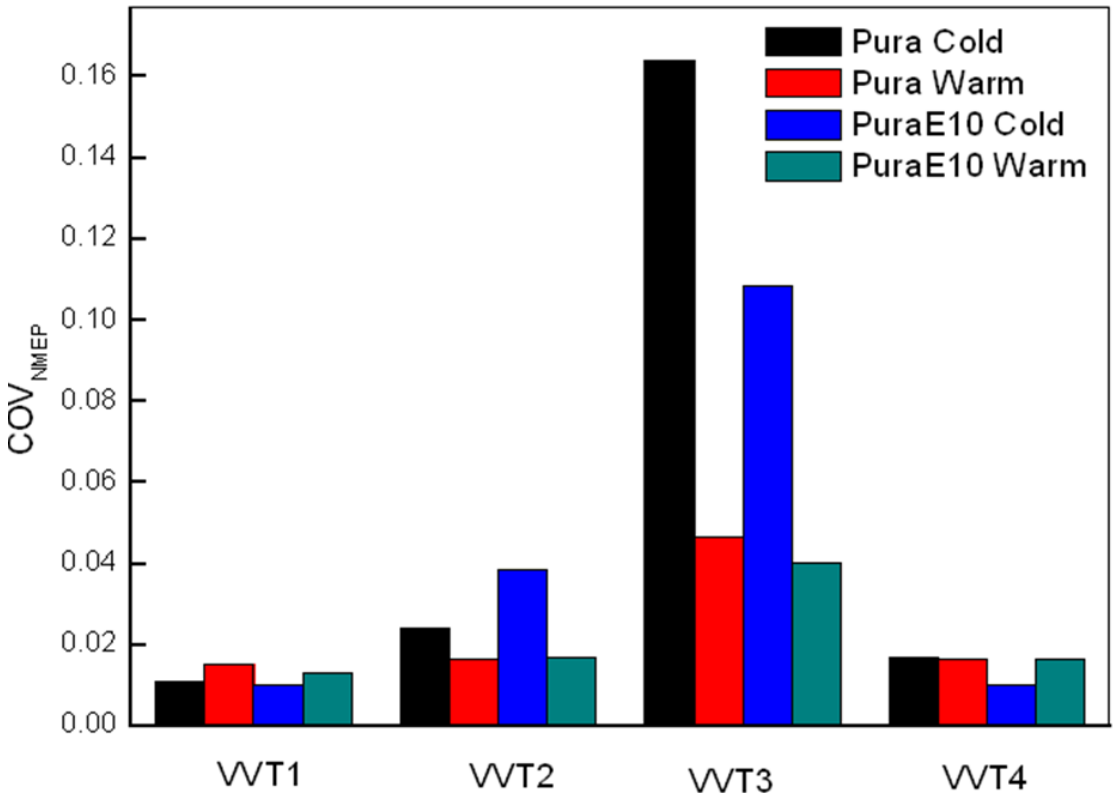

Fig. 5.13 CoV of IMEP for different valve timings (defined in Table 5.4)

5.3.3 Thermo-Gravimetric Analysis (TGA) of PM-laden filters

Compared to a cold engine, a warm engine normally produces much less PM emissions, which causes the TGA results for the warm engine tests to be less accurate due to the noise and uncertainties (such as the buoyancy effect) in the measurement. For this reason, only cold engine tests filters were analyzed and the mass fraction percentages of soot and VOF for different samples are presented in Fig. 5.14.

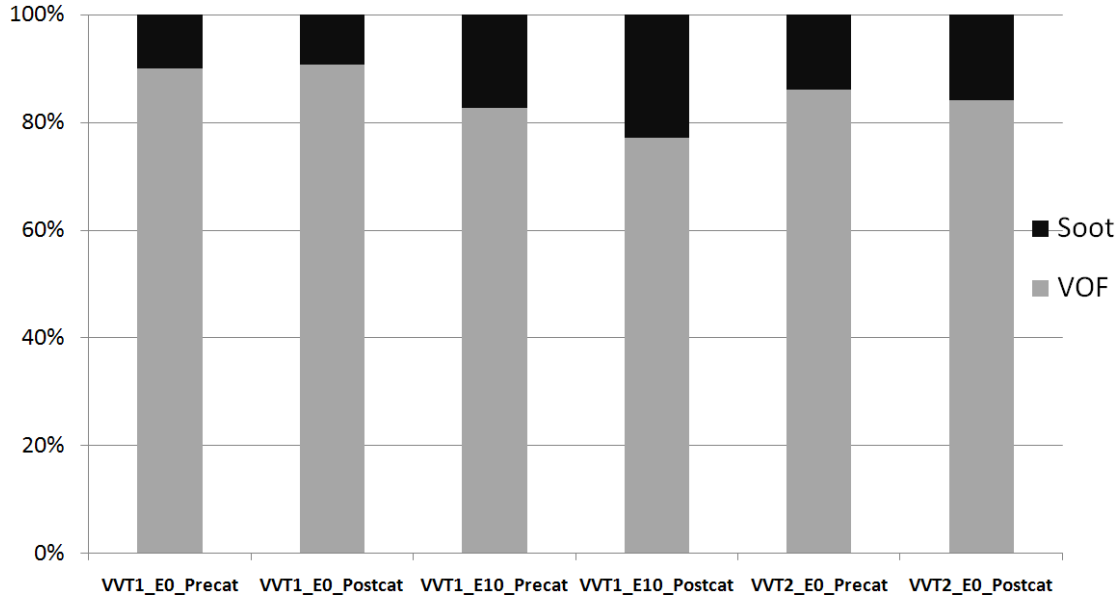

Fig. 5.14 *Soot and Volatile Organic Fraction (VOF) mass fraction percentages of different filter-borne PM*

Three different operating points were selected for the TGA tests, namely, PURA with VVT1, PURA E10 with VVT1 and PURA with VVT2. Under each condition, both pre- and post-catalyst PM samples were analyzed. VVT2 was selected as a representative valve timing with high valve overlap, and hence a high internal EGR rate.

Most of these filter-borne PM exhibit less than 20% mass percentage of soot. In general, little difference was observed between pre- and post-catalyst samples as far as the ratio between VOF and soot is concerned. The high EGR level at VVT2 seems to have led to a rise in the carbonaceous content slightly, whilst adding 10% ethanol doubled the soot mass percentage compared to the base fuel results.

5.4 Conclusions

In this study, four different combinations of intake and exhaust valve timings, two different fuels (PURA and PURA E10) and two coolant temperatures were tested in a V8 spray guided injection engine. PM emissions from the upstream and downstream of the engine catalyst were measured by the DMS500 and sampled by glass-fibre filters. The effects of the valve timing, engine coolant temperature, fuel and the catalyst on the characteristics of engine-out PM such as size/mass distributions and mass fractions in different volatility ranges have been studied. A dedicated simulation was conducted to provide predictions of the internal EGR rate and mass fractions of residuals under different valve timings. The simulated results correlated with the PM results measured by the DMS500. The key findings are listed as follows:

- The total Pn increased by a factor of 2-6 while the total Pm increased by a factor of 3-7 when the engine coolant temperature decreased from 90ºC to 20ºC;
- Under cold engine conditions, PURA produced higher total Pn and Pm than its E10 blend by up to 3 times. On the contrary, adding 10% by volume ethanol led to a slight increase in total Pn and Pm by a maximum of 2 under warm engine conditions;
- VVT3 (with the highest residuals level) always produced the lowest PM emissions on both a number and mass basis among the four valve timing combinations for all the tests. VVT2 produced the second lowest total Pn and Pm except for PURA cold data. VVT1 and VVT4 produced similar PM emissions;

- WAVE simulation shows that due to the relatively larger valve overlap at VVT3 and VVT2, more residual gas fraction is trapped in the cylinder and hence there is a higher gas temperature during compression, which will improve fuel spray atomization and mitigate PM formation. But high internal EGR can reduce the combustion stability;
- In terms of PM mass fractions in different volatility ranges, all the tested filter-borne PM had generally less than 20% by mass soot. A high EGR level seems to have led to a rise in the carbonaceous content slightly, whilst adding 10% ethanol doubled the soot content.

6. A Study of Spray Vaporization Behaviour, Mixture Homogeneity, Combustion Stability and Particulate Emissions with a Range of Gasoline/Ethanol Blends

6.1 Introduction

It is likely that the spray pattern and mixture preparation play a significant role in PM emissions from DISI engines, especially from the second generation spray-guided direction injection engines. Chapter 4 shows that the E10 spray was notably larger and of longer duration than the gasoline spray for both single and triple injection modes (Chen *et al*., 2010).

The current study presents the PM emissions measured by the DMS500 in a single-cylinder optical access DISI engine fuelled with a range of fuels including PURA (a low aromatic gasoline) and its E10, E20, E50, E70, E85 blends under cold and warm conditions (20ºC and 80ºC engine coolant temperature). The engine was at 1500 rpm and 0.5 bar MAP with a stoichiometric relative Air Fuel Ratio (AFR) throughout the experiments. Synchronized spray images are presented here, along with results from some Matlab-based image processing software, which has been developed to calculate the projected spray area and to aid visual interpretation by using a false colour imaging technique. Fast FID (fFID) measurements have been undertaken to examine the cyclic variability of in-cylinder pre-flame HC concentrations, so as to give an indication of the mixture homogeneity in the vicinity of the spark plug immediately before ignition. Finally combustion data, such as indicated mean effective pressure

and mass fraction burned traces are presented in order to examine the response to ethanol addition in different proportions with gasoline.

6.2 Experimental apparatus and test method

6.2.1 Engine, Fuels and Operating Conditions

The test engine for this study is the single-cylinder optical access SGDI engine as introduced in Section 2.2. An AFR sensor was used to measure oxygen content in the exhaust and to set the correct fuel injection pulse width to achieve a stoichiometric mixture, which was maintained for all the tests presented in this chapter.

PURA is a gasoline provided by Shell with known composition that was shown in Section 4.2. The range of ethanol blended fuels used in this study was 10%, 20%, 50%, 70% and 85% volumetric percentage of ethanol. As already mentioned (Section 4.2.2), the latent heat of evaporation for a stoichiometric mixture of ethanol and air is about 5 times that of PURA and air mixture - this could make evaporation of PURA/ethanol blends more difficult and hence lead to higher heterogeneity of the mixture than that for PURA. Furthermore, the lower stoichiometric air fuel ratio of ethanol requires about 1.5 times more ethanol to achieve the same energy output (Hsieh *et al*., 2002).

All the tests were performed under a steady-state part load operating condition with an engine coolant temperature of about 20ºC or 80ºC and Table 6.1 summarizes the operating conditions.

Table 6.1 Engine operating conditions

Fuel	Pura, PuraE10, PuraE20, PuraE50, PuraE70, PuraE85
Injection timing	280º bTDC
Ignition timing	30º bTDC
Engine speed	1500 rpm
Manifold pressure	0.5 bar
Coolant temperature	20ºC, 80ºC

Inspection of the injection timing in Table 4 shows that the Start of Injection (SOI) occurs in the intake stroke, and this is meant to produce a nominally homogeneous mixture. The ignition timing selected here is the MBT (Minimum ignition advance for Best Torque) for PURA only. The MBT for its ethanol blends may vary due to the difference in burning velocity and mixture preparation between ethanol and PURA. The reason for adopting the same ignition timing for all fuels is that the time for spray break-up and evaporation is the same so that the time for mixture preparation will have no influence on PM emissions.

6.2.2 Instrumentation

Instruments for PM Measurements

PM number (Pn) concentrations and size distributions were measured using a Cambustion Ltd DMS500. The Cambustion Ltd sampling system was used, as it has a heated sample pipe and uses dilution air to prevent water condensation. A detailed description of its working principle is in Section 1.6.1 and elsewhere in the literature (Symonds *et al*., 2007). An attempt was also made to measure the exhaust soot concentration using an AVL GmbH Photo Acoustic Soot Sensor (PASS). It turned out that the soot concentrations for all tests were too low to maintain a satisfactory signal-to-noise level, therefore these results are not reported here.

Fast FID for Measuring In-cylinder Pre-flame Hydrocarbon Concentration

The Flame Ionization Detector (FID) is an instrument for the determination of the HC concentration in a gas sample. The concept was first demonstrated by McWilliam and Dewar for the detection of hydrocarbon species in gas chromatography (McWilliam and Dewar, 1958).

A Cambustion Ltd HFR400 fast FID was used in this work to investigate the variability of pre-flame hydrocarbon concentration near the spark plug. The fast prefix refers to the instrument time response which can be as low as one millisecond. The Cambustion Ltd Sampling Spark Plug (SSP) kit was used with the Cambustion Ltd HFR400 Fast Response FID hydrocarbon detector to measure in-cylinder transient hydrocarbon concentration on a millisecond time-scale. The SSP is an offset spark plug with a threaded hole for accommodating a sampling capillary as shown in Fig. 6.1. When assembled, the tip of the sampling capillary should be adjacent to the spark plug electrodes to provide an accurate measure of the hydrocarbon concentration at this location before ignition.

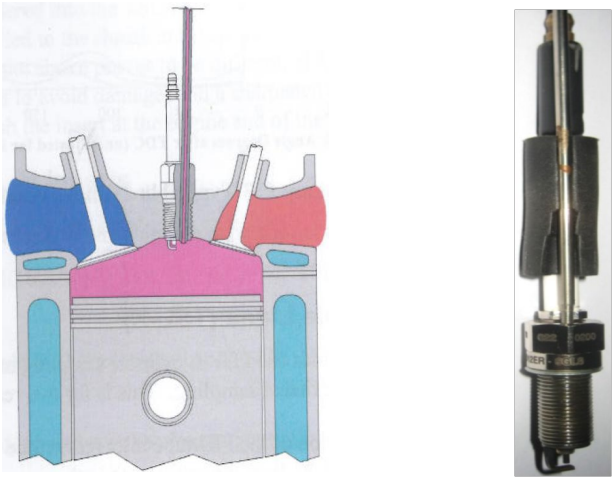

Fig. 6.1 *The Cambustion Ltd Sampling Spark Plug (User Manual of HFR400 Fast FID)*

Instruments for Data Logging and Imaging

Injection and combustion images of 20 consecutive cycles were captured by a Photron PCI-1024 high speed video camera in conjunction with synchronized DAQ signals for each operation point. Both spray and combustion images were recorded at a frame rate of 6000 frames per second (fps), equivalent to 1.5° crank angle per image for an engine speed of 1500 rpm. The camera allowed a maximum spatial resolution of 512×256 pixels at this frame rate.

Illumination was achieved with a synchronized LED system for imaging the spray, whilst the combustion process was visualized by imaging the visible light flame chemiluminescence on a cycle-by-cycle basis without LED illumination. The trigger TTL pulses for controlling the LED and the camera were generated by the Engine Timing Control System (ETCS), which also facilitates the synchronized data logging via RS-232 serial links to the NI DAQ cards. In order to reduce the risk of overflowing the on-board camera memory, 2 intermittent TTL pulses, rather than one long TTL pulse, were fed into the camera as a trigger signal to capture both spray and combustion events separately. The pulse generation diagram is shown in Fig. 6.2 followed by a detailed explanation.

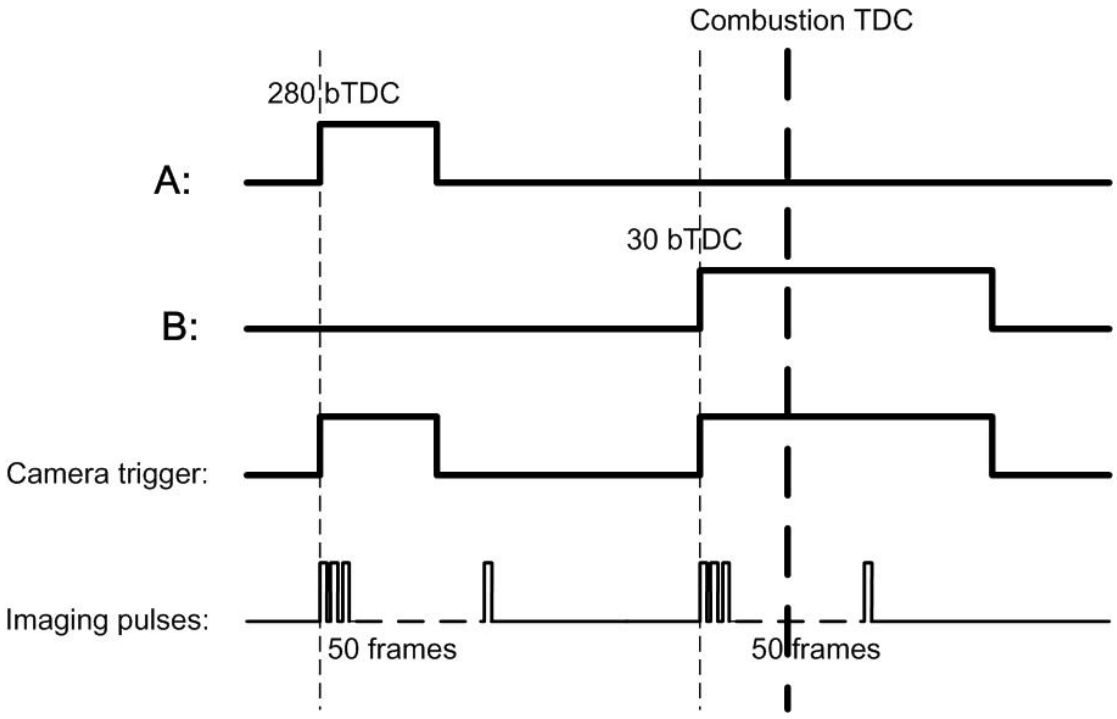

Fig. 6.2 Pulse generation diagram for the camera trigger signal

Signal A is sent by the ETCS with a pulse width of 40°CA, which is used to trigger the LED power supply for illuminating the spray for 40°CA continuously. 40°CA was selected because it is long enough to cover the main period of injection and any longer pulse width could break the LED as it was being over-driven. A function generator with zero delay was used between the ETCS and the LED system to prevent potential damage to the ETCS. Signal B is also generated by the ETCS with a pulse width of 100°CA, which can comfortably cover the combustion process. Signal A and Signal B were combined by using an OR in a logic gate interface box and the combined signal was fed into the camera merely as the trigger signal. Upon reception of a rising edge of the camera trigger signal, 50 frames were automatically taken at the pre-determined frame rate of 6000 fps, which is equivalent to 75°CA duration for an engine running at 1500 rpm.

6.2.3 Data Analysis and Image Processing

The DMS500 Data Analysis

PM number concentrations normalized with the differential interval of the logarithm of particle size were automatically inverted from the matrix of the DMS500 electrometer currents. 1.5 minutes of data were logged for each operation point after the engine fired and had been stabilized for 20-30s. However, spikes in the region of sub-23nm occasionally occurred on the particulate number weighted spectra, which could easily obscure the ensemble-averaged results. Therefore, sub-23 nm data were truncated (this is also in agreement of test procedure proposed by EU PMP program, which specifies that a volatile particle remover is used as introduced in Section 2.4). Data from above 700 nm particle size were truncated as well, due to the fact that the number concentration in this range is low and comparable to the noise level in the instrument.

Image Processing

For spray images, the image processing procedure illustrated in Fig. 6.3 is divided into 4 steps:

1. Convert original images to greyscale ones;
2. Convert greyscale images to binary ones by setting a threshold pixel intensity which is meant to differentiate spray plumes and other small bright components (such as the spark plug, edges of valves) from the dark background;

3. Set another threshold value for the region size and further filter out those small sized bright components so as to set the pixel value to 1 for the spray plume region only;
4. Using the binary images, apply false colouring to the spray plumes whilst keeping the background and other regions in greyscale to aid visual interpretation of spray plumes.

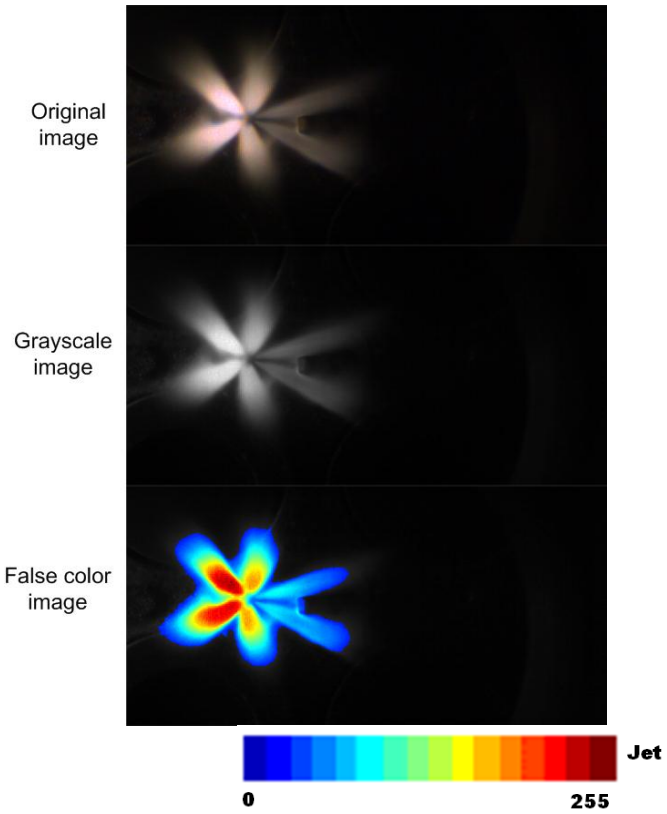

Fig. 6.3 Image processing sequence

After step 3, i.e. the fuel plumes being separated from the background, the pixel intensity of the plumes in each image was numerically integrated as an indicator of the amount of fuel present in the cylinder. As shown in Fig. 6.3, a 'Jet' colourmap has been used for spray images, and the colourmap ranges from blue (0) to red (255). The integrated values enable a comparison of spray development between different fuels in a quantitative manner (this will be seen later in Fig. 6.10).

Combustion images for representative cycles (those which had the nearest IMEP value to the ensemble-averaged IMEP) were superimposed on the MFB traces.

Fast FID Data Analysis

Making in-cylinder fFID measurements is more difficult than exhaust measurements and it requires great caution for both the system operation and data interpretation. During the intake stroke in which injection occurred, the cylinder is at sub-atmospheric pressures and the flow may reverse in the sample line; this will lead to an erroneous output. Therefore only signals near the combustion TDC are taken as valid signals because sample flow reversal is not an issue within this range, due to the high in-cylinder pressure. Typical pre-flame fFID signals are shown in Fig. 6.4 together with the synchronized in-cylinder pressure traces.

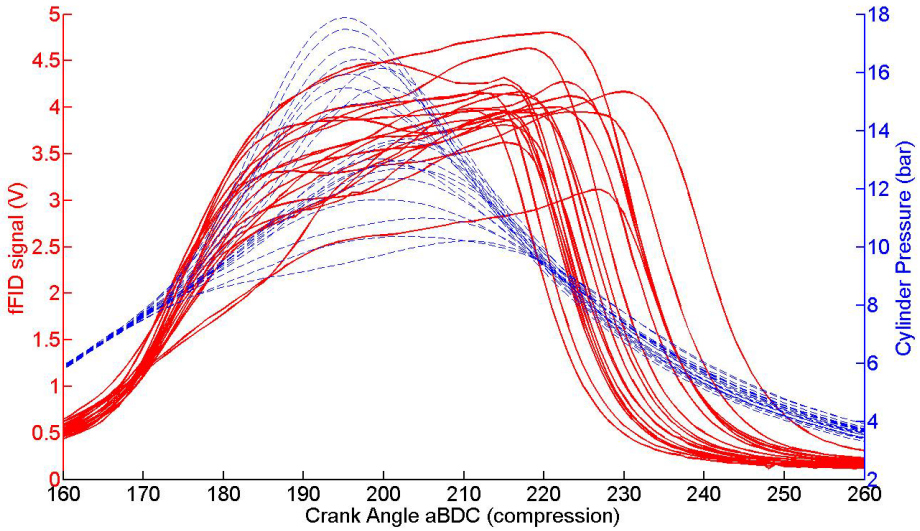

Fig. 6.4 *An example of pre-flame fFID signals and the in-cylinder pressure traces (PURA, 80°C)*

The drop associated with each fFID trace indicates the combustion of the mixture at the spark plug (sample probe) and it is worth noting that both the flame arrival time

and the pre-flame HC concentration exhibit cyclic variability. Since the ignition occurs at a fixed crank angle position for all cycles, the variability in the apparent flame arrival time will be due to a genuine variation and any variability of the transit time in the fFID sampling capillary (which is due to differences in the pressure history). Therefore, the local maximum values for each trace have been taken as the indicator of the pre-flame mixture HC concentration and the ensemble coefficient of variation has been calculated to represent the cyclic variability of the pre-flame HC concentration, which reflects the mixture in-homogeneity.

Combustion Data Analysis

Crank angle resolved in-cylinder pressure data were split on a cyclic basis and a range of combustion performance parameters were calculated using the MATLAB-based software, CoBRA. The parameters presented in this chapter include: indicated mean effective pressure (IMEP) and crank positions at which 10% and 80% MFB occur and their statistical parameters such as average values and the coefficient of variation.

6.3 Results and Discussion

6.3.1 Particulate Emissions Characteristics with Different Ethanol Blends

As stated in section 6.2.1, the engine was running under a steady-state light load operating point, i.e. 1500 rpm, 0.5 bar MAP. The injection timing and the ignition timing were also fixed throughout all the tests as listed in Table 6.1. The only engine operation parameter varied is the coolant temperature, which is 20°C for the cold condition and 80°C for the warm condition. Figure 6.5 shows the size resolved

number concentrations for the PM emissions with different fuels calculated on the basis of the deliberately truncated data for the 23-700 nm size range particles.

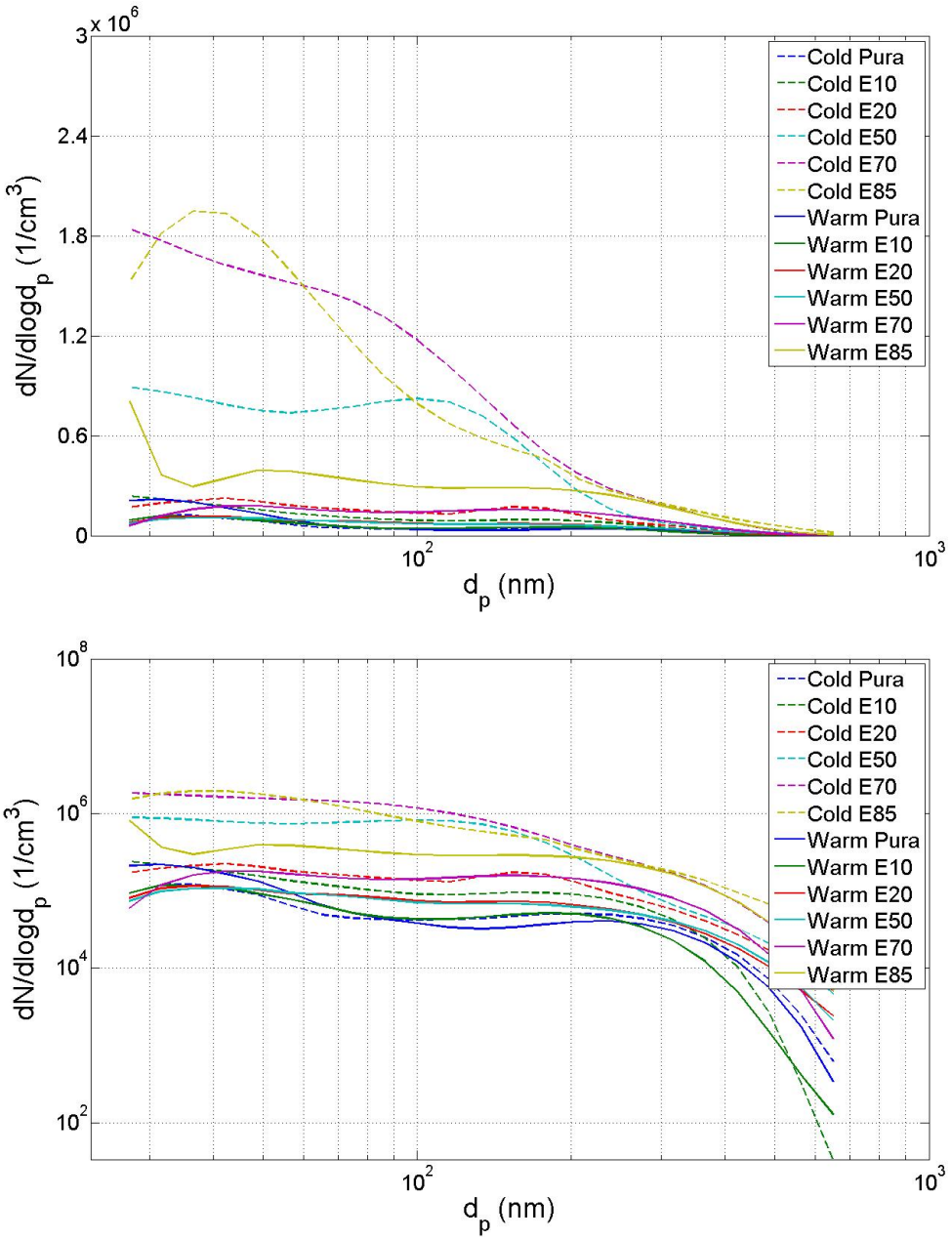

Fig. 6.5 *Size resolved number concentrations of PM emissions on a semi-logarithmic scale (top) and on a double-logarithmic scale (bottom) for different PURA/ethanol blends in a cold (20ºC) and a warm (80ºC) engine*

The reason for adopting a double-log scale is that the whole dataset over the size range of 23-700 nm spans several orders of magnitude and the difference in the results

(especially at large sizes) is indiscernible on a semi-log scale. On both figures, the cold engine data are represented by broken lines whilst the warm engine data are represented by solid lines. For each ethanol/PURA blend, it is clear that the cold engine always produced a higher particulate number concentration for almost the whole size range examined here. The effect of ethanol blending on the PM emissions is that the increase in ethanol content results in the increase in particulate number over the whole size range. This trend for the cold operating points is clearer than that for the warm condition. The phenomena observed here are attributed to the differences in the fuel spray characteristics. Due to the higher enthalpy of vaporization and lower energy density of ethanol compared with PURA, the extent to which the spray breaks-up and collapses decreases as the ethanol blending percentage increases, therefore a fuel with a higher ethanol content will produce a greater mixture in-homogeneity and higher PM number. This effect might be reduced when the engine is warm due to the improved spray atomization for all the tested fuels.

The size resolved PM mass concentrations are shown in Fig. 6.6.

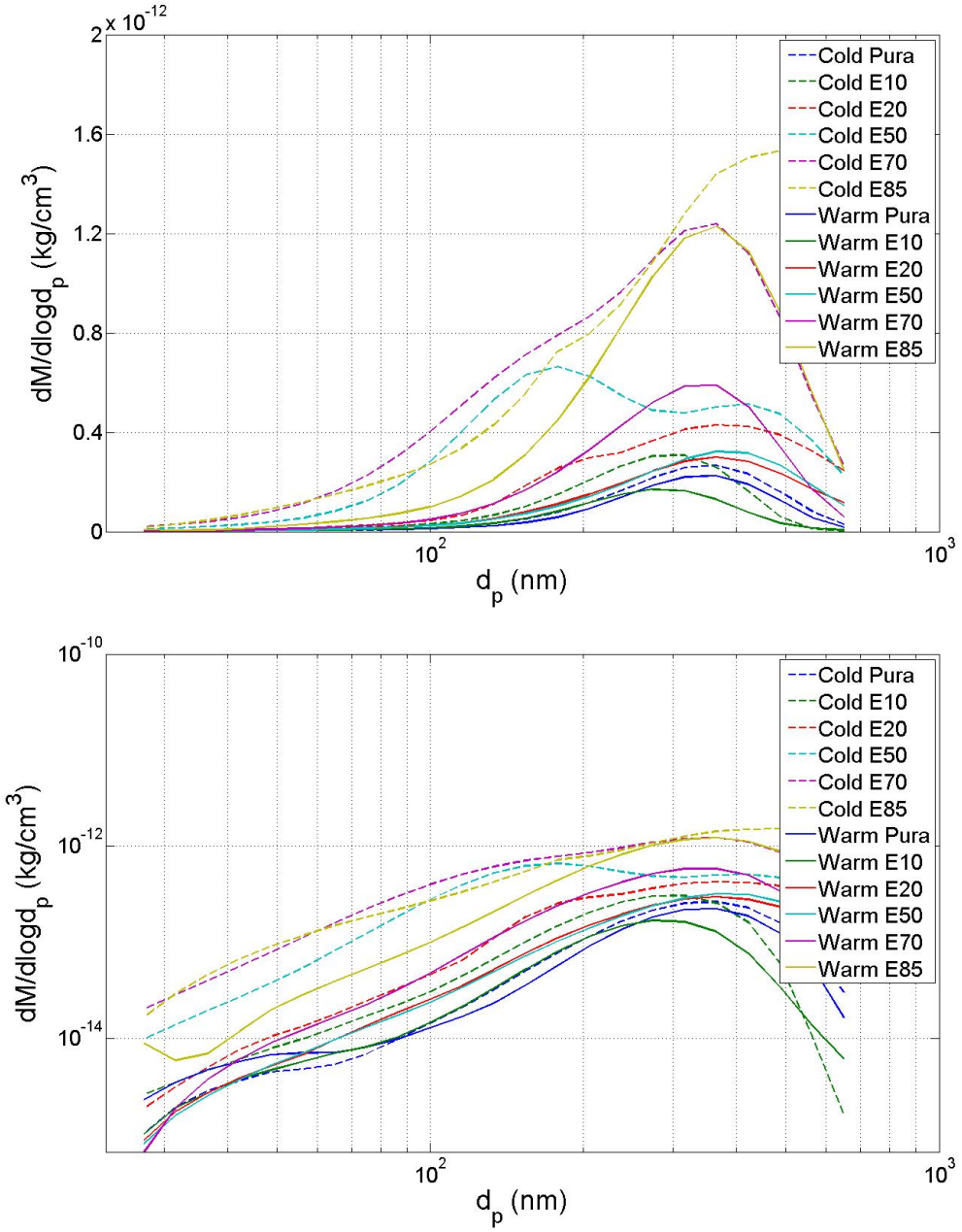

Fig. 6.6 *Size resolved mass concentrations of PM emissions on a semi-logarithmic scale (top) and on a double-logarithmic scale (bottom) for different PURA/ethanol blends in a cold (20ºC) and a warm (80ºC) engine*

An obvious difference between these mass weighted distributions and the above number weighted distributions is that the peak positions on the mass spectra always lie in the accumulation PM mode size range, i.e. above 100 nm whilst the sub-100 nm particles dominate the number spectra. This feature is universally applicable to PM

emissions from DISI engines because the mass of nucleation mode particles (5-50 nm), despite their high quantity in number, contributes little to the total mass. In this sense, the double-log figure will make the data at small particle sizes discernible.

Apart from the E10 data at large sizes, the effect of the ethanol blends on the PM mass concentrations is similar to that found on the PM number concentrations. In other words, the PM mass concentrations increase as the ethanol content increases. And this trend is clearer for the cold condition than for the warm condition. Again, the poor spray atomization performance and hence the high mixture in-homogeneity for the ethanol blends induces their high PM mass emissions. Since the number at large sizes is very small, the high noise to signal ratio could confound the actual results, which may cause the abnormality of the E10 results at large sizes.

By numerically integrating the above PM number and mass spectra, the total particulate number and mass for all the operating points were calculated and these are shown in Fig. 6.7.

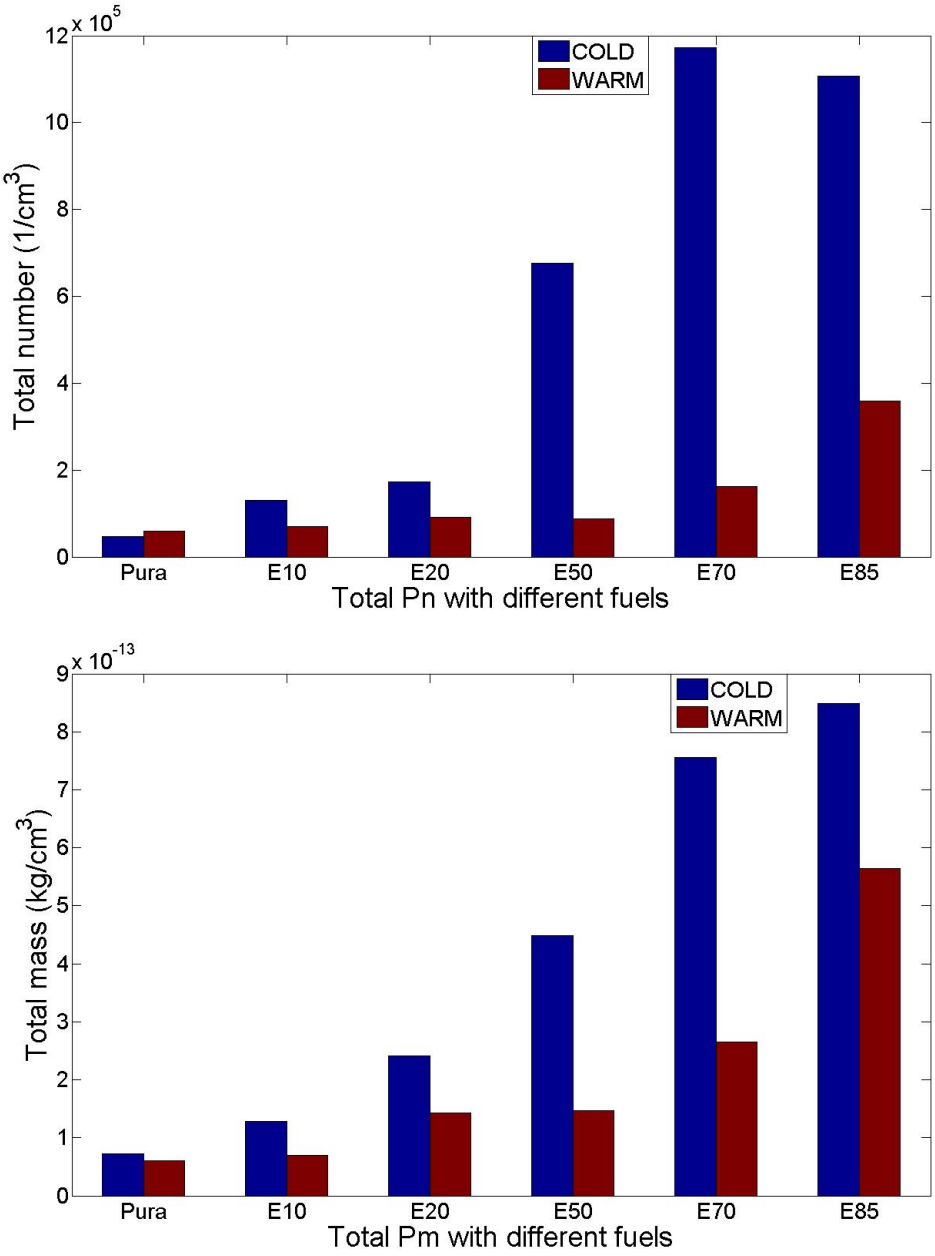

Fig. 6.7 *Total particulate number (top) and total particulate mass (bottom) emissions for different PURA/ethanol blends in a cold (20℃) and a warm (80℃) engine*

Fig. 6.7 shows that under the cold condition, the increased ethanol content produced higher PM emissions in terms of both total number and total mass. The trend for the warm condition is less clear, and is subject to exceptions for PURA and its blends with low ethanol contents. For PURA, the PM total number under the warm condition is higher than under cold condition. The main reason for these abnormalities is that

PURA and its E10 produce very low level of PM emissions (less than one order of magnitude more than background level) due to its composition of low aromatics and hence the high noise to signal ratio might have confounded the actual results. Also, any slight difference in AFR would affect the results.

In terms of total PM number, E85 produces 15 times higher total PM number than PURA under cold condition but only 6 times higher under warm condition. The total PM mass with PURA E85 is 11 times that with PURA under the cold condition whilst it is 8 times higher under the warm condition.

6.3.2 Spray and Combustion Images and Combustion Performance Analysis

Spray Development with Different Fuels under Cold and Warm Conditions

As introduced in section 6.2.3, false colour images have been obtained using a Matlab-based image processing software. Combustion analysis was applied to the cylinder pressure data using the Rassweiler and Withrow method (Rassweiler and Withrow, 1938). The spray images from a typical cycle, which had the nearest IMEP value to the ensemble average IMEP, have been presented in Fig. 6.8 and Fig. 6.9. Fig. 6.8 and 6.9 show spray development of typical cycles for different fuels under cold and warm conditions respectively.

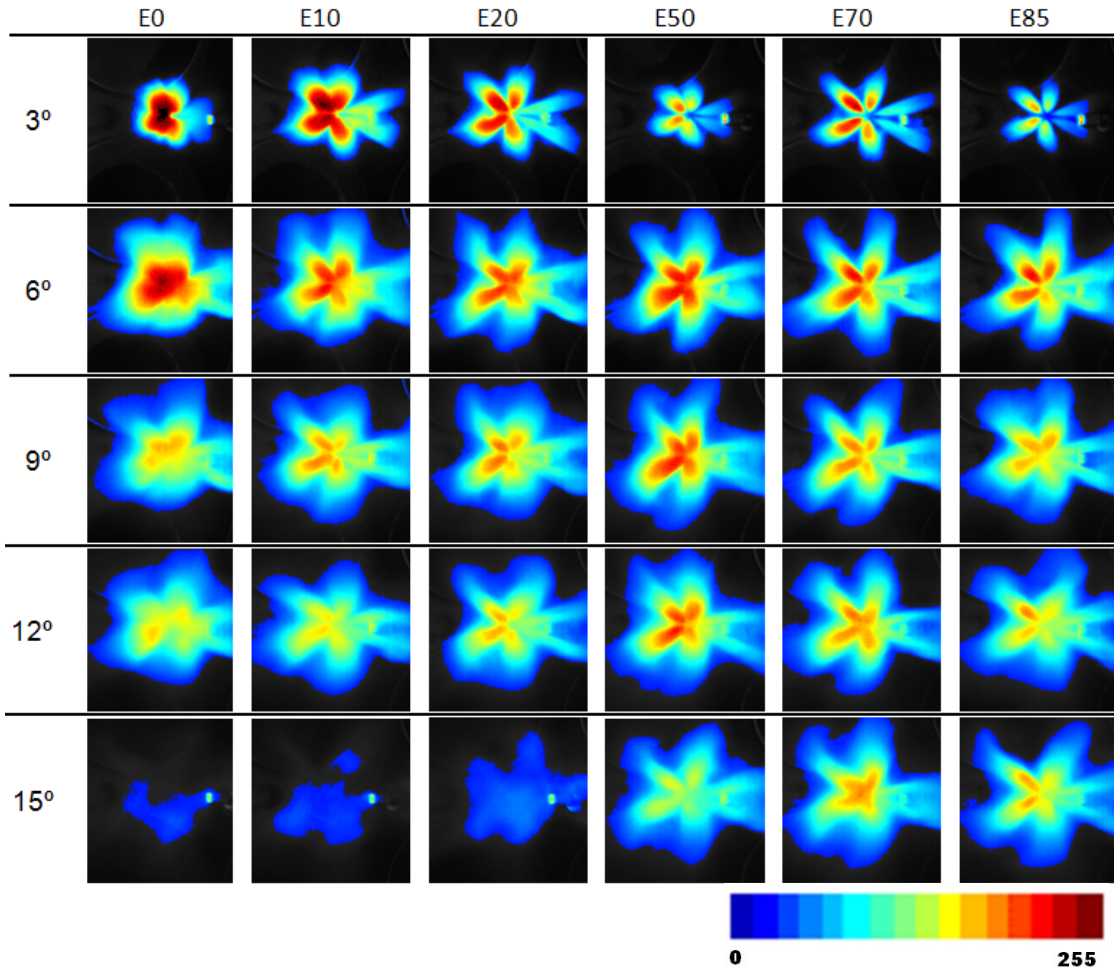

Fig. 6.8 *Spray development on swirl plane under cold (20°C) coolant condition from 277 to 265 CA bTDC (3° to 15° CA with respect to the SOI) in steps of 3°CA for different PURA/ethanol blends*

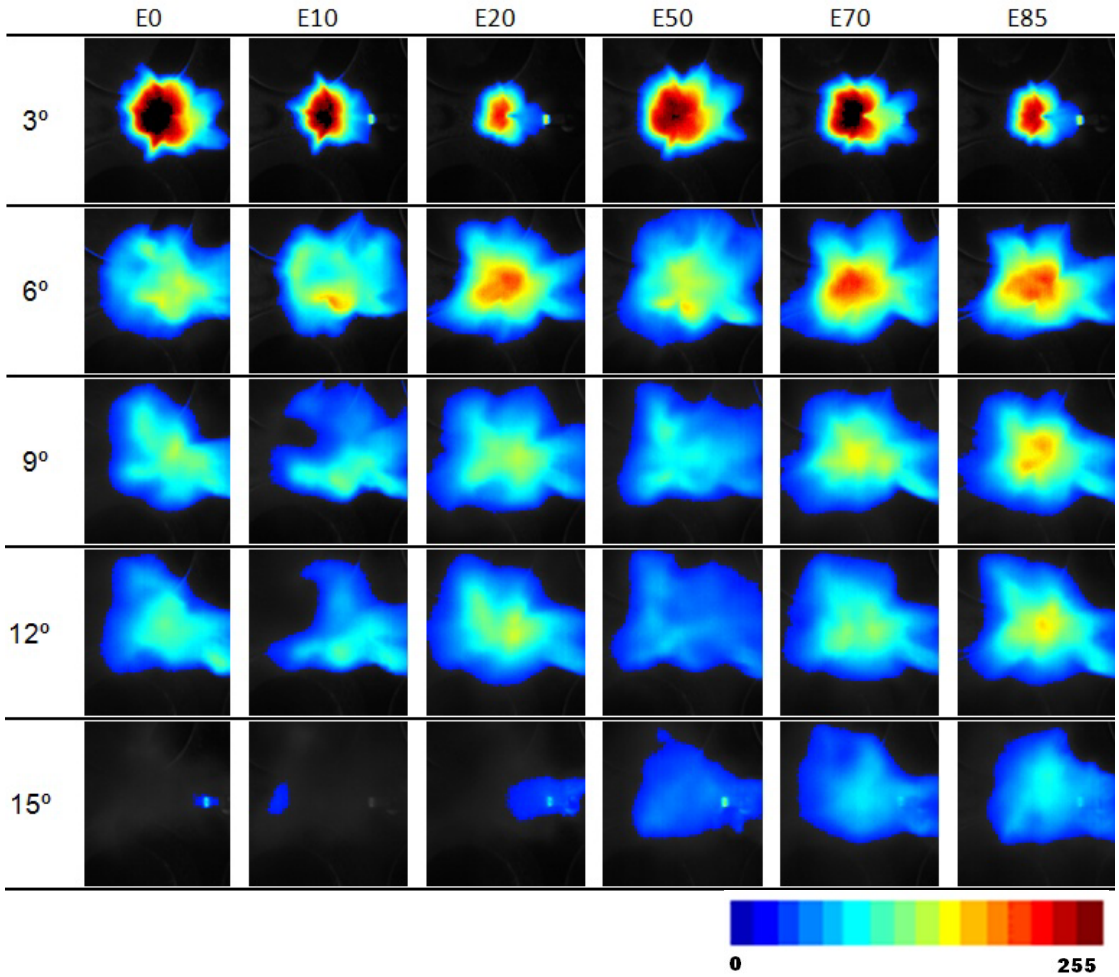

Fig. 6.9 *Spray development on swirl plane under warm (80ºC) coolant condition from 277 to 265°CA bTDC (3º to 15º CA with respect to the SOI) in steps of 3°CA for different PURA/ethanol blends*

The selected images for each column start with 277º bTDC and end with 265º bTDC, i.e. from 3º to 15º CA after the SOI. As shown in both figures, there is a notable variability in terms of spray area at 3º CA after the nominal start of injection, which is due to shot-to-shot variations in injection.

From Fig. 6.8 and Fig. 6.9, two general observations can be made:

1. Cold engine injection plumes are more defined and have higher pixel values than warm ones. This is visible immediately in the first frame, which indicates that all the test fuels break-up and collapse to a lesser extent under the cold condition than under the warm condition;
2. For both the cold and warm engine images, spray area and spray duration increase as the ethanol blending percentage increases. For cold E70 and E85, the individual plumes are even identifiable at 265°bTDC (15º CA after the SOI) whilst the spray almost vanishes for fuels with small ethanol blending percentages.

In order to compare the Mie scattering (the scattering of electromagnetic radiation by spherical particles) images of the different fuels quantitatively, the pixel value on each image was integrated as an indicator of the amount of fuel present in the cylinder. The ensemble averaged values were calculated and plotted on Fig. 6.10. The bars associated with the average values are ±1 standard deviation.

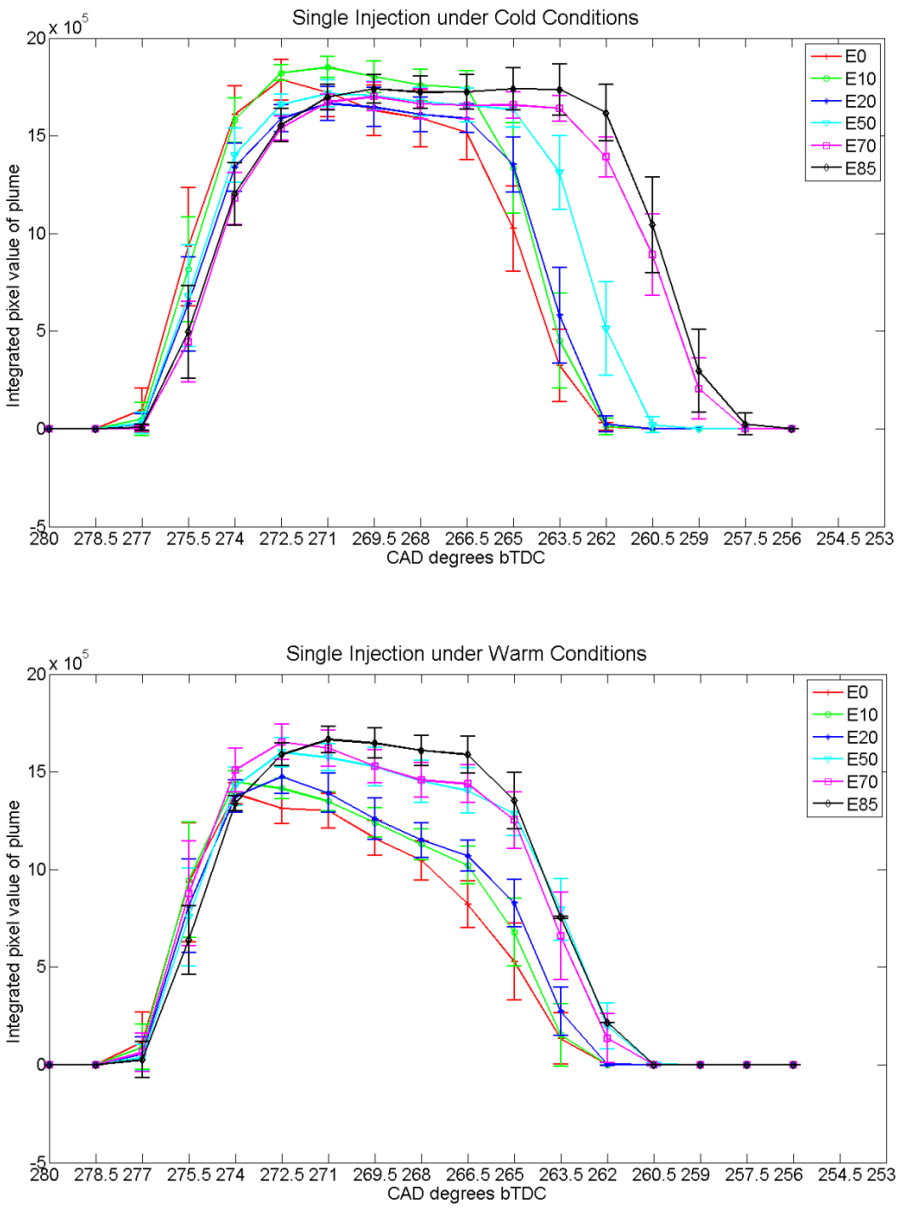

Fig. 6.10 *Integrated pixel values as a function of crank angle for the cold condition (20ºC, top) and warm condition (80ºC, bottom) for different PURA/ethanol blends; the bars associated with the average values are ±1 standard deviation.*

In general, the warm fuel plumes exhibit smaller integrated pixel values than the cold fuel plumes for all the fuels tested, and the spray duration for the warm engine is also shorter than for the cold engine. This is because warm coolant heats the injector and hence promotes the fuel evaporation process.

The spray duration increases as the ethanol content increases, and this implies that ethanol addition worsens fuel evaporation due to its high enthalpy of vaporization and low energy density. This trend is clearer for the cold engine than for the warm engine, in other words, the cold engine is more susceptible to a deterioration in fuel evaporation caused by the ethanol addition.

The standard deviations in the 'plateau' region are always smaller than at the start or at the end due to the fact that the plumes change more rapidly at both ends than in the 'plateau' region.

Combustion Analysis and Chemiluminescence Images

Table 6.2 summarizes the combustion performance parameters with different fuels under cold and warm conditions.

Table 6.2 Ensemble average values of combustion parameters for the different PURA/ethanol blends in a cold (20ºC) and warm (80ºC) engine

	IMEP (bar)	0-10% MFB (°CA)	10-80% MFB (°CA)
E0,cold	2.7	44.9	31.3
E10,cold	2.6	45.5	31.8
E20,cold	2.8	44.9	31.3
E50,cold	2.8	46.9	34.9
E70,cold	2.8	47.1	39.4
E85,cold	2.7	47.6	38.7
E0,warm	2.7	40.2	26.2
E10,warm	2.5	39.3	26.6
E20,warm	2.8	39.5	26.4
E50,warm	2.6	41.9	29.1
E70,warm	2.5	42.5	29.5
E85,warm	2.6	42.4	28.7

Fig. 6.11 shows the CoV of IMEPs indicating the combustion stability with different fuels.

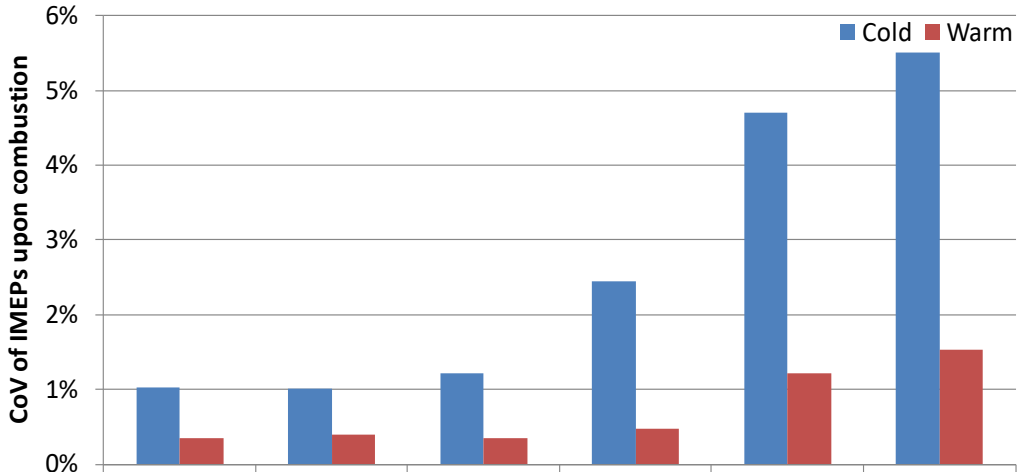

	Pura	E10	E20	E50	E70	E85
Cold	1.02%	1.01%	1.21%	2.45%	4.70%	5.51%
Warm	0.35%	0.39%	0.35%	0.47%	1.22%	1.53%

Fig. 6.11 CoV of the IMEP with different PURA/ethanol blends for the cold (20°C) and warm (80°C) conditions

In general, a warm engine exhibits less variability than a cold engine in terms of IMEP for all the test fuels. In other words, the combustion stability becomes better when the engine warms up.

Fig. 6.12 shows the durations of 10% and 80% Mass Fraction Burned (MFB) for different fuels in terms of crank angle degrees.

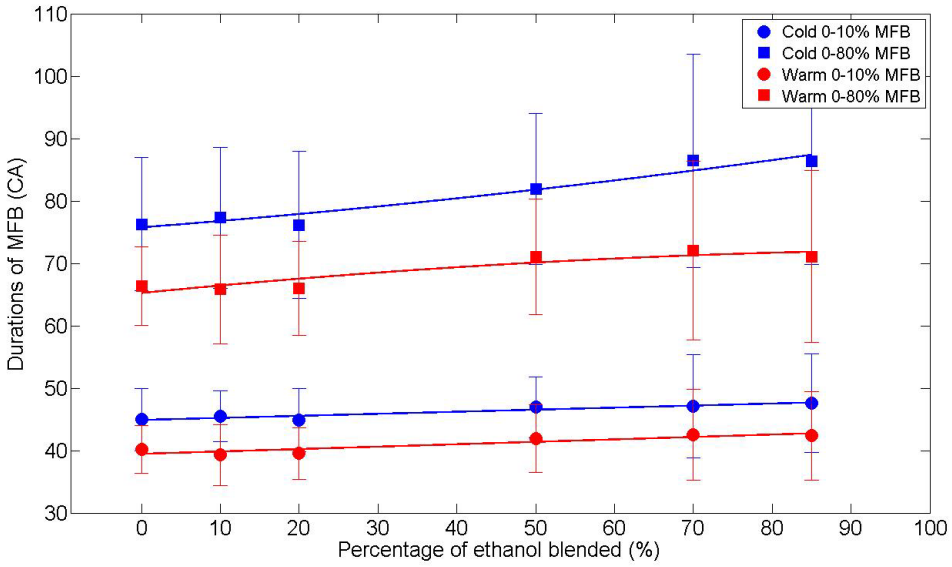

Fig. 6.12 *The durations of 10% and 80% Mass Fraction Burned (MFB) with the different PURA/ethanol blends for the cold (20°C) and warm (80°C) conditions*

The 10% and 80% Mass Fraction Burned (MFB) durations represent the initial and main stages of combustion. The end of combustion (80-100% MFB) exhibits much higher variability and this is because the optical engine has large crevice volumes (polymeric piston rings, no lubricant, differences in thermal expansion between the engine block and piston, etc.) than normal production engines and hence there could be more fuel trapped in the crevices which might be burned late during the expansion stroke (Ma, 2006). Therefore, 80% MFB is considered to be the end of the main combustion period.

Fig. 6.12 demonstrates that adding ethanol slowed down the combustion process slightly and this trend is more clear for the main combustion stage (80% MFB) than for the initial combustion stage (10% MFB). Aleiferis *et al.* (2010) found that the poorer atomization and break-up efficiency indicated from droplet sizing and spray imaging for E85 could have contributed to the lower peak combustion pressures, and

marginally slower combustion compared with the base fuel. Wang (2008) also pointed out that the high latent heat of evaporation and the lower calorific value of ethanol will lower the combustion temperature and hence reduce the flame speed.

Fig. 6.13 illustrates the combustion process during the expansion stroke by superimposing chemiluminescence images over ensemble averaged in-cylinder pressure and MFB traces. As introduced in section 6.2.3, the selected images are from cycles which have the IMEP nearest to the ensemble-averaged one. In this chapter, only PURA and its E85 images are presented because they are representative of both chemiluminescence-dominated images and sooty (red glowing) images respectively.

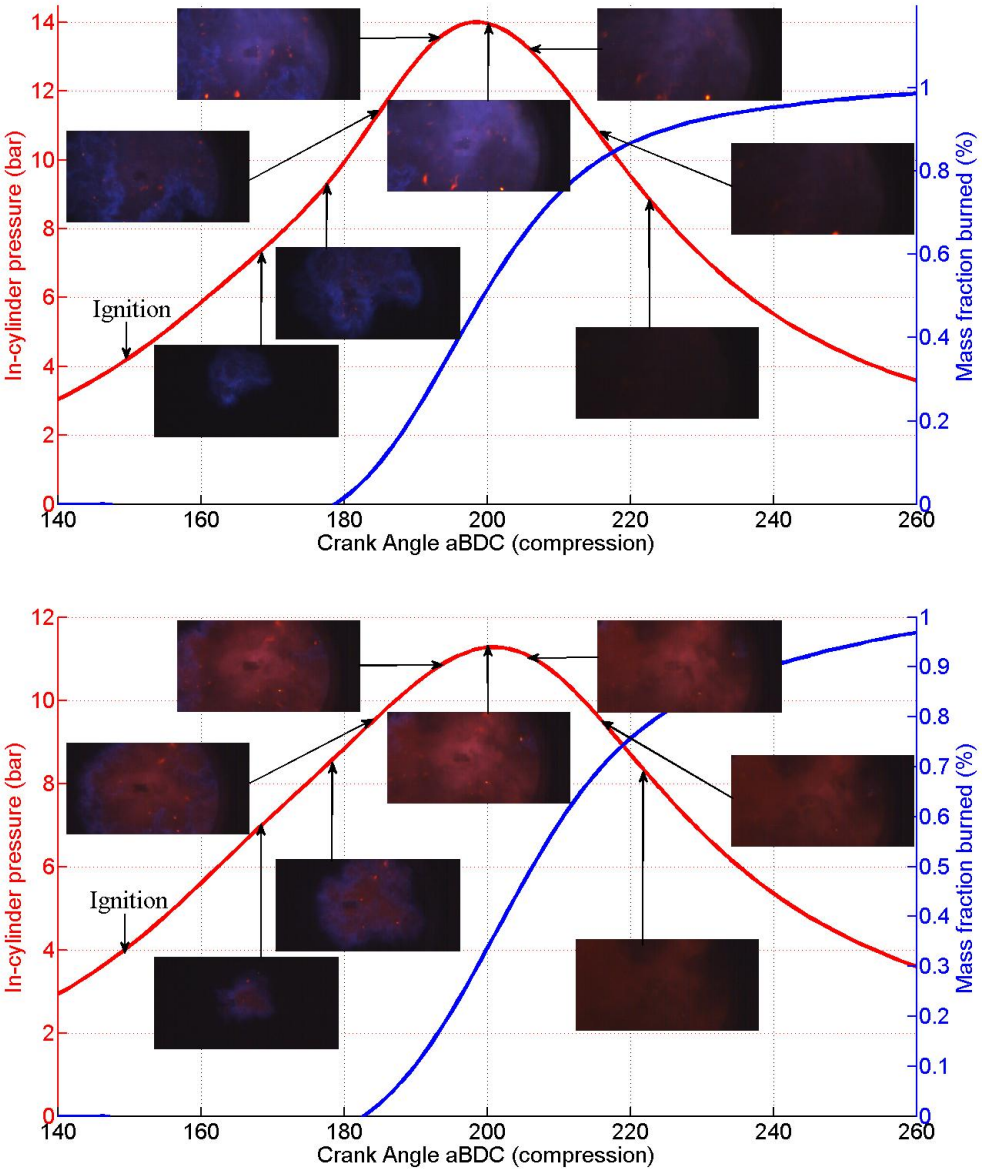

Fig. 6.13 *Ensemble averaged in-cylinder pressure and MFB traces superimposed with the corresponding combustion chemiluminescence images from 170-222.5°aBDC in steps of 7.5°CA (top: warm PURA; bottom: warm E85)*

For the images with PURA, which has a low aromatic content, the blue flame dominates with a few red spots indicating the presence of soot. Whilst for the E85 images, the blue flame can hardly be detected because the red spots dominate the whole cylinder. This implies that E85 produced much more PM than PURA during

the combustion stroke, which is consistent with the DMS500 measurement results for engine-out emissions.

The fact that the blue flames in the PURA images are not visible any more after approximately 70% MFB is because the radiation intensity was too low to be detected by the camera at 6000 fps. The sooty spots in the E85 images are visible even beyond the 80% MFB point, which is consistent with the burning rate results derived from Table 6.2, i.e. E85 burns slower than PURA.

6.3.3 Pre-flame Mixture Homogeneity

The CoV of the pre-flame fFID signals was calculated as an indicator of mixture in-homogeneity in the vicinity of the spark plug. In this study, no attempt was made to resolve the absolute HC concentration. The reason is that the variability of the HC concentration rather than their absolute values is the subject of interest, so no complicated dynamic calibration was needed. Fig. 6.14 shows the CoV of the pre-flame HC concentration for each fuel under cold and warm conditions.

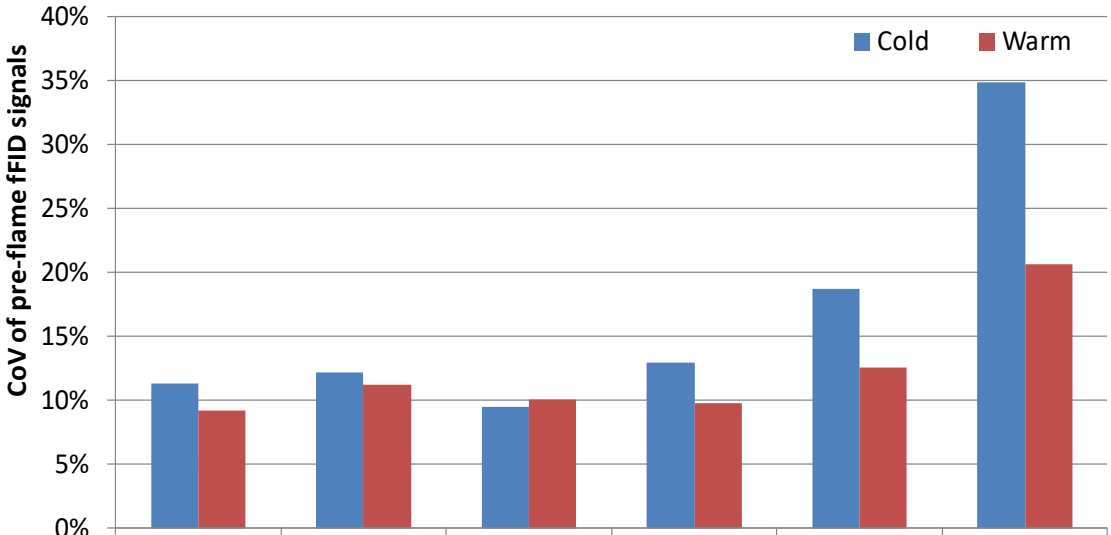

	Pura	E10	E20	E50	E70	E85
Cold	11.3%	12.1%	9.5%	13.0%	18.7%	34.9%
Warm	9.2%	11.2%	10.0%	9.7%	12.6%	20.7%

Fig. 6.14 CoV of the pre-flame fFID signals for the different fuels in a cold (20°C) and warm (80°C) engine

For fuels with an ethanol content higher than 50%, the increase in ethanol blending led to an increase in the CoV of the pre-flame fFID signals; the trend is less clear with fuels with a low ethanol proportion. In other words, a high ethanol percentage could lead to an increase in the mixture in-homogeneity at the spark plug, presumably because of the deteriorating effect of ethanol on the spray break-up efficiency. Apart from E20, the in-homogeneity values for the cold engine are higher than for the warm one, which implies that the increase in engine coolant temperature helped to decrease the mixture in-homogeneity and hence stabilize the subsequent combustion.

6.4 Conclusions

Particulate emissions in a single-cylinder optical access DISI engine were measured using the Cambustion Ltd DMS500 for size-resolved number concentrations and derived mass concentrations. A range of fuels including PURA and its ethanol blends

in different blending proportions (E0 to E85) have been tested under cold (20ºC) and warm (80ºC) coolant conditions. Spray and combustion characteristics were investigated using high-speed imaging and the variability of pre-flame HC concentration at the spark plug was also measured using the Cambustion Ltd fFID. The main findings are:

- An increase in ethanol addition led to an increase in both particle number and mass over the size range of 23-700 nm, due to the deleterious effect of ethanol on spray break-up and the evaporation efficiency as a result of its high vaporization enthalpy and low energy density. This trend is more pronounced in a cold engine than in a warm one. The ratios between maximum and minimum values in terms of total Pn and Pm are 16 and 11 under cold conditions and 7 and 8 under warm conditions.
- Cold spray plumes are more clearly defined and last longer than warm plumes for all the test fuels. Integrated pixel values of the plumes on each image have been calculated to indicate the amount of fuel present in the cylinder at a particular crank angle. As the ethanol content increases, the integrated pixel values remain high for longer which implies that spray breaks-up and evaporates to a lesser extent for fuels with high ethanol proportions than with low ethanol proportions.
- A warm engine exhibits less variability than a cold engine in terms of IMEP and MFB durations for all the test fuels, and a warm engine also produces a higher maximum in-cylinder pressure and faster burning rate than a cold one. In terms of the effects of ethanol on combustion performance, the ethanol addition appears to have reduced the burning velocity and reduced the

maximum in-cylinder pressure. Combustion images showed that fuels with a high ethanol content generated much more soot than fuels with a low ethanol content. The latter images exhibited a clear blue flame front which could be further analysed to derive flame growth and motion speeds.

- The variability of the pre-flame HC concentrations under the cold conditions is normally higher compared with the warm conditions, and this indicates that the increase in coolant temperature facilitates evaporation and hence stabilizes the subsequent combustion. For fuels with high ethanol blending ratios, the increase in ethanol content led to an increase in the mixture in-homogeneity at the spark plug.

7. Conclusions and Suggestions for Future Work

7.1 Conclusions

Particulate Matter (PM) emissions from vehicles have progressively become a subject of great interest in recent years. Despite the compelling potential for reductions in fuel consumption, gasoline direct injection engines are subject to increased PM emissions due to the inevitably reduced time for spray atomization and increased chance of fuel impingement. This has led to a need to investigate the characteristics of the particulate emissions from these engines. Measuring these PM emissions is of great importance, not only to the automotive industry due to the increasingly stringent PM regulations, but also to the medical profession for their epidemiological and toxicological studies on humans' health.

In this chapter, conclusions will be made based on the results of engine tests described in Chapters 4, 5 and 6. The majority of the findings fall into two catalogues: firstly they are concerned with the effects of engine operating parameters on PM emissions, i.e. the effects of injection and ignition timing, injection strategy, coolant temperature, three-way catalyst (TWC) and valve timing on PM emissions; secondly they are concerned with the influence of fuel composition (different gasoline/ethanol blends) on PM emissions and other parameters such as spray behaviour, mixture homogeneity, and combustion stability. The major findings are summarized as follows.

7.1.1 The Influence of Engine Operating Parameters on PM Emissions

Tests have been carried out in both a single-cylinder optical engine and a V8 GDI engine with a three-way catalyst. The base fuels (PURA and a Toluene Reference Fuel) used in this work are of known composition and their E10 blends were also tested so as to investigate the effects of ethanol addition on PM emissions. Both engines were operated at 1500 rpm under part load and the exhaust aerosol at the upstream and downstream of the TWC fitted to the V8 engine were analyzed by the DMS500 and sampled by glass-fibre filters. The main findings include:

- In general, advancing the injection timing during the intake stroke led to a reduction in both the Pn (Particle number) and the Pm (Particle mass), which is attributed to the increased time for fuel evaporation and hence the improved mixture homogeneity.
- There was a parabolic response for PM emissions with ignition timing, with the lowest PM emissions registered at an ignition timing of 20º CA bTDC. Advancing the ignition timing from 20º to 45º CA bTDC led to a rise in both the total Pn and the total Pm whilst retarding the ignition timing from 20º to 5º CA bTDC also increased the PM emissions which may be due to the poor combustion quality with late ignition timings.
- The triple injection (SOI was at 300, 290, 280º bTDC) mode produced slightly less Pn and Pm than the single injection mode (SOI of 280º bTDC) under the same stoichiometric operating condition. This is qualitatively vindicated by the combustion images.

- The three-way catalyst has shown a significant reduction effect on volatile PM in the nucleation mode, whilst little effect on the accumulation mode PM has been observed.
- Reducing the coolant temperature from 90º to 20º C (the engine was run cold) led to a reduction in the exhaust temperature from 280ºC to 240ºC and an increase in the total Pn and Pm by factors of 2-6 and 3-7 respectively. For stoichiometric conditions, adding 10% ethanol can produce higher total Pn and Pm by 2 times under warm conditions whilst lower total Pn and Pm by about 1/3 under cold conditions.
- Both experimental and computational results show that increasing positive valve overlap can lead to a higher gas temperature during compression (due to more residual gas fraction being trapped in the cylinder), which will improve the fuel spray atomization and mitigate PM formation. On the other hand, as a result of increasing positive valve overlap, a high internal EGR (Exhaust Gas Recirculation) level will reduce the combustion stability.
- The injection images with PURA and PURA E10 showed that adding 10% by volume ethanol extended the vaporization process, presumably because ethanol has a higher enthalpy of vaporization and a lower energy density than the base fuels.
- In terms of PM mass fractions in different volatility ranges, little effect of ignition timing was found in this work. Increasing the internal EGR rate led to a slight increase in the carbonaceous mass percentage of filter borne PM whilst adding ethanol led to a significant rise in the carbonaceous mass percentage.

7.1.2 Effect of Ethanol Addition on PM Emissions

Particulate Matter (PM) legislation for gasoline engines and the introduction of gasoline/ethanol blends, make it important to know the effect of fuel composition on PM emissions. To address this issue, tests have been conducted with PURA (a low aromatic gasoline provided by Shell) and its E10, E20, E50, E70, E85 blends in a single-cylinder optical access engine under cold and warm conditions (20ºC and 80ºC engine coolant temperature). The engine was run at part load with an engine speed of 1500 rpm and a MAP of 0.5 bar absolute with a stoichiometric Air Fuel Ratio (AFR) throughout the experiments. A number of instruments were used together with the DMS500 to investigate the causes for the difference in the PM emissions. They included a Photron high speed camera with a synchronized LED illumination system for capturing spray and combustion images, and a Cambustion Ltd fFID for assessing the pre-flame mixture in-homogeneity. Combustion performance data (such as IMEP, MFB) were also calculated based on the in-cylinder pressure data. The main findings are summarized as follows.

- Increasing the ethanol content led to an increase in both the Pn and the Pm due to the deleterious effect of ethanol on spray atomization as a result of its high vaporization enthalpy and low energy density.
- Spray images with different fuels showed that fuel sprays break-up and evaporate to a lesser extent for fuels with high ethanol proportions than those with low ethanol proportions, and that spray plumes are more defined and persistent under cold engine conditions than those under warm engine conditions.

- The increase in ethanol content results in an increase in the pre-flame mixture in-homogeneity at the spark plug. Increasing the coolant temperature will decrease the mixture in-homogeneity, in other words, increasing the coolant temperature could help to stabilize the injection and hence the subsequent combustion.
- For stoichiometric conditions, adding ethanol or decreasing the coolant temperature will reduce the combustion stability. Combustion images showed that fuels with a high ethanol content produced much more soot than fuels with a low ethanol content, which is in agreement with the DMS500 data.

7.2 Suggestions for Future Work

The present studies were limited to steady-state engine operating conditions with constant load and speed. The DMS500 enables instantaneous acquisition of data for PM size-resolved number concentrations at a sampling rate of up to 10 Hz. Therefore, this work could be extended to chassis dynamometer tests to examine the PM emissions with transient driving cycles, which will enable car manufactures to tune calibratable parameters for PM abatement.

The dilution ratio and dilution air condition can be regarded as important parameters in respect of PM emissions. In the present study, a single dilution ratio (~10:1) and filtered ambient air was used for exhaust dilution. Further work can be extended to see the effects of varying these parameters on the PM emissions.

The use of Scanning Electron Microscopy (SEM) enables the observation and characterization of particulate matter on a nano-meter to micrometer scale. Nowadays,

SEM has been in increasing use due to its high resolution which makes it possible to examine at high magnifications (such as 100,000x), and the large depth of field (the amount of the sample that can be in sharp focus at any one time), which can be up to 400 times greater than that of an optical microscope. It would be useful to take SEM images of filter-borne PM and derive the PM size distributions. It is also worth comparing the size distributions obtained from the SEM images and the DMS500 results. The Transmission Electron Microscopy (TEM) offers an even better resolution than a scanning electron microscope. However, it requires a great deal of care for sample preparation and examination because the TEM grids are so delicate that they can be broken quite easily. Since the SEM and TEM are normally operated at very low pressure, HC evaporation will occur during the EM tests, leaving the carbonaceous material behind.

Filter weighing and storage inside a controlled environmental chamber was not possible in this work, so this might have impacts on the TGA results. Filters were stored in sealed petri-dishes before being analyzed by TGA. It would be desirable to keep and weigh filters in a well controlled room with constant temperature and humidity. TGA in the present work provided the information regarding the mass fractions of elemental carbon and volatile materials present in the PM. This can be extended to include the use of solvent extraction methods followed by the GCMS (Gas Chromatography and Mass Spectrometry). This will provide useful information regarding the chemical compositions of the organic materials, especially the PAHs, present in PM.

Spray images exhibited a notable shot-to-shot variation in injection. It is conceivable that this variation is due to the variability of the injection hardware, i.e. the driver units and injectors, given the fact that the injection pulse and camera trigger signal are all digitally controlled with negligible delay time. The current pulse supplied to the injector was comprised of two main sections: initially, the current rises rapidly to ensure rapid opening of the injector nozzle; the current then reduces to an intermediate level to hold the nozzle open, this lower current level ensuring a quicker closing at the end of the injection event (Romunde and Aleiferis, 2009). To assess the repeatability of the injection system, future work should include measuring the injector current and calculating the average and standard deviation of the delay time for reaching the maximum current level. The delay between driver voltage pulse and the start of current on the injector is also subject to cyclic variability (Romunde and Aleiferis, 2009) and might contribute to this shot-to-shot variation found in the injection images.

Finally, by developing numerical modelling (perhaps in collaboration with the simulation group or Professor Markus Kraft at Cambridge) more insight can be gained into the particulate formation and growth mechanisms in GDI engines.

7.3 Implications of This Work

In real-world applications, rich mixture operation (including departure from stoichiometric conditions during load change transients) leads to high levels of PM emissions – about an order of magnitude higher than at stoichiometric conditions. Under these circumstances bio-fuel addition leads to a significant reduction in PM emissions.

Vehicle manufacturers should introduce more flex-fuelled vehicles that are optimized for using gasoline that has wide ranging ethanol content. Government should give fiscal incentives for using ethanol that has been manufactured from non-food renewable sources.

References

Abdul-Khalek, I.S., Kittelson, D.B., and Graskow, B.R., *Diesel Exhaust Particle Size: Measurement Issues and Trends.* SAE Technical Paper 980525, 1998.

Akinlua, A., Torto, N., Ajayi, T.R., and Oyekunle, J.A.O., *Trace Metals Characterisation of Niger Delta Kerogens.* Fuel. 86(10-11): p. 1358-1364, 2007.

Aleiferis, P.G., Serras-Pereira, J., Romunde, Z., Caine, J., and Wirth, M., *Mechanisms of Spray Formation and Combustion from a Multi-hole Injector with E85 and Gasoline.* Combustion and Flame. 157(4): p. 735-756, 2010.

Alger, T.F., Mehta, D., Hall, M.J., Matthews, R.D., and Ng, H.K., *Particulate Characterization of a Disi Research Engine Using a Nephelometer and In-Cylinder Visualization.* 2001-01-1976, 2001.

Al-Hasan, M., *Effect of Ethanol-Unleaded Gasoline Blends on Engine Performance and Exhaust Emission.* Energy Conversion and Management. 44(9): p. 1547-1561, 2003.

Andersson, J., Wedekind, B., Hall, D., Stradling, R., Barnes, C., and Wilson, G., *Detr/Smmt/Concawe Particle Research Program: Sampling and Measurement Experiences.* SAE Technical Paper 2000-01-2850, 2000.

Andrews, G.E., Elamir, I.E., Abdelhalim, S., Shen, Y., and Williams, P.T., *The Measurement of Lubricating Oil Combustion Efficiency Using Diesel Particulate Analysis.* SAE Technical Paper 980523, 1998.

Bai, Y.L., Wang, Z., and Wang, J.X., *Study on Improvement of Part-Load Performance in a GDI Engine Using Exhaust Gas Trap.* Neiranji Xuebao/Transactions of CSICE (Chinese Society for Internal Combustion Engines). 27(4): p. 328-332, 2009.

Barale, R., Bulleri, M., Cornetti, G., Loprieno, N., and Wachter, W.F., *Preliminary Investigation on Genotoxic Potential of Diesel Exhaust.* SAE Technical Paper 920397, 1992.

Beltzer, M., Campion, R.J., and Petersen, W.L., *Measurement of Vehicle Particulate*

Emissions. SAE Technical Paper 740286, 1974.

Brunt, M. and Emtage, A.L., *Evaluation of Burn Rate Routines and Analysis Errors.* SAE Technical Paper 970037, 1997.

Cavina, N., Ponti, F., Siviero, C., and Suglia, R., *Residual Gas Fraction Estimation for Model-Based Variable Valve Timing and Spark Advance Control*. Long Beach, CA, United states: American Society of Mechanical Engineers, 2004.

Chen, L., Braisher, M., Crossley, A., Stone, R., and Richardson, D., *The Influence of Ethanol Blends on Particulate Matter Emissions from Gasoline Direct Injection Engines.* SAE Technical Paper 2010-01-0793, 2010.

Cheng, W.K., Summers, T., and Collings, N., *The Fast-Response Flame Ionization Detector.* Progress in Energy and Combustion Science. 24(2): p. 89-124, 1998.

Clenci, A.C., Descombes, G., Podevin, P., and Hara, V., *Some Aspects Concerning the Combination of Downsizing with Turbocharging, Variable Compression Ratio, and Variable Intake Valve Lift.* Proceedings of the Institution of Mechanical Engineers, Part D: Journal of Automobile Engineering. 221(10): p. 1287-1294, 2007.

Crawford, J.G. and Wallace, J.S., *Validation Tests for a Fast Response Flame Ionization Detector for In-Cylinder Sampling Near the Spark Plug.* SAE Technical Paper 961201, 1996.

Cuthbertson, R.D., Shore, P.R., Sundstrarm, L., and Hedaen, P.O., *Direct Analysis of Diesel Particulate-Bound Hydrocarbons By Gas Chromatography With Solid Sample Injection.* SAE Technical Paper 870626, 1987.

Cuthbertson, R.D., Stinton, H.C., and Wheeler, R.W., *The Use of a Thermogravimetric Analyser for the Investigation of Particulates and Hydrocarbons in Diesel Engine Exhaust.* SAE Technical Paper 790814, 1979.

Dipardo, J., *Outlook for Biomass Ethanol Production and Demand.* Energy Information Administration, US Department of Energy, Washington, D.C., 2000.

Eastwood, P., "*Particulate Emissions from Vehicles"*. John Wiley & Sons, 2007. ISBN 978-0-7680-2060-1.

Elegant, D.S., Kang, T., and Kyritsis, D.C., *Experimental Investigation of Electrostatic Effects on Ethanol and Ethanol-Diesel Blend Sprays in Atmospheric Ambiance.* International Journal of Vehicle Design. 50(1-4): p. 35-49, 2009.

Fontana, G. and Galloni, E., *Variable Valve Timing for Fuel Economy Improvement in a Small Spark-Ignition Engine.* Applied Energy. 86(1): p. 96-105, 2009.

Foster, D.E., Kweon, C.B., Schauer, J., and Okada, S., *Detailed Chemical Composition and Particle Size Assessment of Diesel Engine Exhaust.* SAE Technical Paper 2002-01-2670, 2002.

Fujiwara, Y., Tosaka, S., and Murayama, T., *Formation Process of SOF in the Combustion Chamber of IDI Diesel Engines.* SAE Technical Paper 932799, 1993.

Gao, J., Jiang, D.M., and Huang, Z.H., *Spray Properties of Alternative Fuels: A Comparative Analysis of Ethanol-Gasoline Blends and Gasoline.* Fuel. 86(10-11): p. 1645-1650, 2007.

Graham, L.A., Belisle, S.L., and Baas, C.L., *Emissions from Light Duty Gasoline Vehicles Operating on Low blend ethanol gasoline and E85.* Atmospheric Environment. 42(19): p. 4498-4516, 2008.

Graskow, B.R., Kittelson, D.B., Ahmadi, M., and Morris, J.E., *Exhaust Particulate Emissions From Two Port-Fuel-Injected, Spark-Ignition Engines.* SAE Technical Paper 1999-01-1144, 1999.

Griffiths, J.F. and Barnard, J.A., *Flame and Combustion.* Blackie, 1995. ISBN 0-7514-0199-4.

Hall, D.E., King, D.J., Morgan, T.B.D., Baverstock, S., Heinze, P., and Simpson, B.J., *A Review of Recent Literature Investigating the Measurement of Automotive Particulate; the Relationship With Environmental Aerosol, Air Quality and Health Effects.* SAE Technical Paper 982602, 1998.

Hansen, A.C., Zhang, Q., and Lyne, P.W.L., *Ethanol-Diesel Fuel Blends -- a Review.* Bioresource Technology. 96(3): p. 277-285, 2005.

Hasimoglu, C., *Exhaust Emission Characteristics of a Low-Heat-Rejection Diesel Engine Fuelled with 10 per cent Ethanol and 90 per cent Diesel Fuel Mixture.*

Proceedings of the Institution of Mechanical Engineers Part D-Journal of Automobile Engineering. 222(D1): p. 93-100, 2008.

Heywood, J., "*Internal Combustion Engine Fundamentals"*. 1988: McGraw-Hill. ISBN 0-07-100499-8.

Hinds, W.C., "*Aerosol Technology (1st ed.)"*. 1982: Wiley. ISBN 0-471-19410-7.

Hinds, W.C., "*Aerosol Technology (2nd ed.)"*. 1999: Wiley. ISBN 0-471-19410-7.

Hong, H., Parvate-Patil, G.B., and Gordon, B., *Review and Analysis of Variable Valve Timing Strategies - Eight Ways to Approach*. 2004: Professional Engineering Publishing.

Hsieh, W.D., Chen, R.H., Wu, T.L., and Lin, T.H., *Engine Performance and Pollutant Emission of an SI Engine Using Ethanol–Gasoline Blended Fuels.* Atmospheric Environment. 36: p. 403-410, 2002.

Kayes, D., Liu, H., and Hochgreb, S., *Particulate Matter Emission During Start-Up and Transient Operation of a Spark-Ignition Engine.* SAE Technical Paper 1999-01-3529, 1999.

Khalek, I.A., *2007 DIESEL PARTICULATE MEASUREMENT RESEARCH.* Final Report: Project E-66-Phase 2, 2006.

Kim, H. and Choi, B., *Effect of Ethanol-Diesel Blend Fuels on Emission and Particle Size Distribution in a Common-Rail Direct Injection Diesel Engine with Warm-up Catalytic Converter.* Renewable Energy. 33(10): p. 2222-2228, 2008.

Kittelson, D.B., *Engines and nanoparticles: a review.* Journal of Aerosol Science. 29(5-6): p. 575-588, 1998.

Kittelson, D.B., Arnold, M., and Watts, J.W.F., *Review of Diesel Particulate Matter Sampling Methods: Final report.* University of Minnesota, Center for Diesel Research, 1999.

Kuwahara, K., Ueda, K., and Ando, H., *Mixing Control Strategy for Engine Performance Improvement in a Gasoline Direct-Injection Engine.* SAE Technical Paper 980158, 1998.

Lapuerta, M., Armas, O., Ballesteros, R., and Duran, A., *Influence of Mini-Tunnel*

Operating Parameters and Ambient Conditions on Diesel Particulate Measurement and Analysis. SAE Technical Paper 1999-01-3531, 1999.

Lapuerta, M., Ballesteros, R., and Rodriguez-Fernandez, J., *Thermogravimetric Analysis of Diesel Particulate Matter.* Measurement Science and Technology. 18(3): p. 650-658, 2007.

Lee, H., Myung, C.L., and Park, S., *Time-Resolved Particle Emission and Size Distribution Characteristics During Dynamic Engine Operation Conditions with Ethanol-Blended Fuels.* Fuel. 88(9): p. 1680-1686, 2009.

Lipsky, E.M. and Robinson, A.L., *Effects of Dilution on Fine Particle Mass and Partitioning of Semivolatile Organics in Diesel Exhaust and Wood Smoke.* Environmental Science & Technology. 40(1): p. 155-162, 2005.

Litzinger, T., Stoner, M., Hess, H., and Boehman, A., *Effects of Oxygenated Blending Compounds on Emissions from a Turbocharged Direct Injection Diesel Engine.* International Journal of Engine Research. 1(1): p. 57-70, 2000.

Luders, H., Kruger, M., Stommel, P., and Luers, B., *The Role of Sampling Conditions in Particle Size Distribution Measurements.* SAE Technical Paper 981374, 1998.

Ma, H., "Optical Diagnostics and Combustion Analysis in a Gasoline direct Injection Engine". D.Phil. Thesis. Oxford, 2006.

Maricq, M.M., Podsiadlik, D.H., Brehob, D.D., and Haghgooie, M., *Particulate Emissions From a Direct-Injection, Spark Ignition (Disi) Engine.* 1999-01-1530, 1999.

Mathis, U., Ristimaeki, J., Mohr, M., Keskinen, J., Ntziachristos, L., Samaras, Z., and Mikkanen, P., *Sampling Conditions for the Measurement of Nucleation Mode Particles in the Exhaust of a Diesel Vehicle.* Aerosol Science and Technology. 38(12): p. 1149 – 1160, 2004.

Matthews, R.D., Huang, Y., and Ellzey, J.L., *Effects of Fuel Volatility, Load, and Speed on HC Emissions Due to Piston Wetting.* SAE Technical Paper 2001-01-2024, 2001.

McWilliam, I.G. and Dewar, R.A., *Flame Ionization Detector for Gas Chromatography.* Nature. 181(4611): p. 760, 1958.

Meyer, R.C. and Thring, R.H., *Mixture Preparation Measurements.* SAE Technical Paper 950069, 1995.

Milovanovic, N., Chen, R., and Turner, J., *Influence of Variable Valve Timings on the Gas Exchange Process in a Controlled Auto-Ignition Engine*. Proceedings of the Institution of Mechanical Engineers, Part D: Journal of Automobile Engineering, 2004.

Mohr, M., Forss, A.M., and Lehmann, U., *Particle Emissions from Diesel Passenger Cars Equipped with a Particle Trap in Comparison to Other Technologies.* Environmental Science & Technology. 40(7): p. 2375-2383, 2006.

Nguyen, D. and Honnery, D., *Combustion of Bio-oil Ethanol Blends at Elevated Pressure.* Fuel. 87(2): p. 232-243, 2008.

Olfert, J.S., Symonds, J.P.R., and Collings, N., *The Effective Density and Fractal Dimension of Particles Emitted from a Light-Duty Diesel Vehicle with a Diesel Oxidation Catalyst.* Aerosol Science. 38: p. 69-82, 2007.

Park, S.H., Kim, H.J., Suh, H.K., and Lee, C.S., *Atomization and Spray Characteristics of Bioethanol and Bioethanol Blended Gasoline Fuel Injected through a Direct Injection Gasoline Injector.* International Journal of Heat and Fluid Flow. 30(6): p. 1183-1192, 2009.

Patashnick, H., Rupprecht, G., Ambs, J.L., and Meyer, M.B., *Development of a Reference Standard for Particulate Matter Mass in Ambient Air.* Aerosol Science and Technology. 34(1): p. 42 – 45, 2001.

Poulopoulos, S.G., Samaras, D.P., and Philippopoulos, C.J., *Regulated and Unregulated Emissions from an Internal Combustion Engine Operating on Ethanol-Containing Fuels.* Atmospheric Environment. 35(26): p. 4399-4406, 2001.

Price, P., "Direct Injection Gasoline Engine Particulate Emissions". D.Phil. Thesis. Oxford, 2009.

Price, P., Stone, R., Collier, T., and Davies, M., *Particulate Matter and Hydrocarbon Emissions Measurements: Comparing First and Second Generation DISI with PFI in Single Cylinder Optical Engines.* SAE Technical Paper 2006-01-1263, 2006.

Price, P., Twiney, B., Stone, R., Kar, K., and Walmsley, H., *Particulate and Hydrocarbon Emissions from a Spray Guided Direct Injection Spark Ignition Engine with Oxygenate Fuel Blends.* SAE Technical Paper 2007-01-0472, 2007.

Queenan, K.B., Nightngale, C.J.E., and Bennett, J., *The Design and Testing of an Arrangement to achieve Stratified Charge through Port-Injection.* Proc. IMechE Seminar on Lean Burn Combustion Engines, 3-4 December, London, 1996.

Rakopoulos, D.C., Rakopoulos, C.D., Kakaras, E.C., and Giakoumis, E.G., *Effects of Ethanol-Diesel Fuel Blends on the Performance and Exhaust Emissions of Heavy Duty DI Diesel Engine.* Energy Conversion and Management. 49(11): p. 3155-3162, 2008.

Rassweiler, G.M. and Withrow, L., *Motion Pictures of Engine Flames Correlated With Pressure Cards.* SAE Technical Paper 380139, 1938.

Richter, H. and Howard, J.B., *Formation of Polycyclic Aromatic Hydrocarbons and their Growth to Soot: a Review of Chemical Reaction Pathways.* Progress in energy and combustion science, 2000.

Romunde, Z. and Aleiferis, P.G., *Effect of Operating Conditions and Fuel Volatility on Development and Variability of Sprays from Gasoline Direct-Injection Multihole Injectors.* Atomization and Sprays, 2009.

Sandford, M., Page, G., and Crawford, P., *The All New AJV8.* SAE Technical Paper 2009-01-1060, 2009.

Serras-Pereira, J. and Aleiferis, P.G., *Characteristics of Ethanol, Butanol, Iso-Octane and Gasoline Sprays and Combustion from a Multi-Hole Injector in a DISI Engine.* SAE Technical Paper 2008-01-1591, 2008.

Shi, J.P. and Harrison, R.M., *Investigation of Ultrafine Particle Formation during Diesel Exhaust Dilution.* Environmental Science and Technology. 33(21), 1999.

Sivia, D.S., "*Data Analysis: A Bayesian Tutorial*". 1994: Oxford: New York. ISBN 0-19-856831-2.

Sleightholme, G.R., *In-Cylinder Measurements of Charge Inhomogeneity in a Spark-*

Ignition Engine. SAE Technical Paper 900484, 1990.

Smallwood, G.J., Snelling, D.R., Guelder, O.L., Clavel, D., Gareau, D., Sawchuk, R.A., and Graham, L., *Transient Particulate Matter Measurements From the Exhaust of a Direct Injection Spark Ignition Automobile.* SAE Technical Paper 2001-01-3581, 2001.

Song, C.-L., Zhang, W.M., Pei, Y.Q., Fan, G.L., and Xu, G.P., *Comparative Effects of MTBE and Ethanol Additions into Gasoline on Exhaust Emissions.* Atmospheric Environment. 40(11): p. 1957-1970, 2006.

Stone, R., "*Introduction to Internal Combustion Engines"*. 1999: PALGRAVE. ISBN 0-333-74013-0.

Stratakis, G.A., Konstantas, G.S., and Stamatelos, A.M., *Experimental Investigation of the Role of Soot Volatile Organic Fraction in the Regeneration of Diesel Filters*. Proceedings of the Institution of Mechanical Engineers, Part D: Journal of Automobile Engineering, 2003.

Summers, T. and Collings, N., *Modelling the Transit Time of a Fast Response Flame Ionization Detector During In-Cylinder Sampling.* SAE Technical Paper 950160, 1995.

Symonds, J., Price, P., Williams, P., and Stone, R., *Density of Particles Emitted from a Gasoline Direct Injection Engine.* 12th ETH Conference on Combustion Generated Nanoparticles (Zurich), 2008.

Symonds, J., Reavell, K., Olfert, J., Campbell, B. and Swift, S., *Diesel Soot Mass Calculation in Real-Time with a Differential Mobility Spectrometer.* Journal of Aerosol Science. 38(1): p. 52-68, 2007.

Wang, X.W., "Instantaneous In-cylinder Heat Transfer and Combustion Analysis in Spark Ignition Engines". D.Phil. Thesis. Oxford, 2008.

Wei, Q., Kittelson, D.B., and Watts, W.F., *Single-Stage Dilution Tunnel Performance.* SAE Technical Paper 2001-01-0201, 2001.

Wirth, M., Zimmmermann, D., Friedfeldt, R., Caine, J., Schamel, A., Davies, M., Peirce, G., Storch, A., Ries-Mueller, K., Gansert, K.P., Pilgram, G., Ortmann, R., Wuerfel, G., and Gerhardt, J., *A Cost Optimised Gasoline Spray Guided Direct Injection System for Improved Fuel Economy.* Prceedings of Fuel

Economy and Engine Downsizing, IMechE, 2004.

Wu, F.J., Wang, J.X., Chen, W.M., and Shuai, S.J., *A Study on Emission Performance of a Diesel Engine Fueled with Five Typical Methyl Ester Biodiesels.* Atmospheric Environment. 43(7): p. 1481-1485, 2009.

Yang, J.L. and Kenney, T., *Some Concepts of DISI Engine for High Fuel Efficiency and Low Emissions.* SAE Technical Paper 2002-01-2747, 2002.

Yoon, S.H., Park, S.H., Suh, H.K., and Lee, C.S., *Effect OF Biodiesel-Ethanol Blended Fuel Spray Characteristics on the Reduction of Exhaust Emissions in a Common-Rail Diesel Engine*, in *Es2008: Proceedings of the 2nd International Conference on Energy Sustainability. Vol 1*. 2009, Amer Soc Mechanical Engineers: New York. p. 463-470, 2009.

Yuecesu, H.S., Sozen, A., Topguel, T., and Arcaklioglue, E., *Comparative Study of Mathematical and Experimental Analysis of Spark Ignition Engine Performance Used Ethanol-Gasoline Blend Fuel.* Applied Thermal Engineering. 27(2-3): p. 358-368, 2007.

Appendix

Issues of MFM measurements for exhaust gas using Honeywell AWM700

Honeywell AWM700 200 LPM mass flow meters are used to measure both diluent air flow rate and diluted gas flow rate. These mass flow meters operate by measuring the rate of relative heat transfer from a heater resistor to a temperature sensing resistor located on either side of the heater. The heat transfer is proportional to the mass flow. Offsets in the sensor sensitivity (thermal efficiency) will occur if the thermal properties of the medium change. The dominant factor is the thermal conductivity of the gas being measured. Additionally, heat capacity and gas viscosity cause lesser effects. (Microbridge Airflow Sensors Gas Correction Factors – Note #3)

Different gas types exhibit different thermal properties, hence the gas correction factors have to be applied when measuring different gases. The gas correction factors are listed as follows:

Table A.1 *Approximate gas correction factors which are referenced to nitrogen as calibration gas type (Microbridge Airflow Sensors Gas Correction Factors – Note #3)*

Gas Type	Approximate Correction Factor
Helium (He)	0.5*
Hydrogen (H_2)	0.7*
Argon (Ar)	0.95
Nitrogen (N_2)	1.0
Oxygen (O_2)	1.0
Air	1.0
Nitric oxide (NO)	1.0
Carbon monoxide (CO)	1.0
Methane (CH_4)	1.1
Ammonia (NH_3)	1.1
Nitrous oxide (N_2O)	1.35
Nitrogen dioxide (NO_2)	1.35
Carbon dioxide (CO_2)	1.35

Fortunately, air, oxygen, and carbon monoxide all have the unity correction factor as listed in the figure due to their nearly identical properties to nitrogen. Engineering support from Honeywell has advised that as long as the relative humidity is below 90% then it should not shift the output. So the only issue with measuring exhaust mass flow rate comes from the CO_2 content in engine-out exhaust because its correction factor is 1.35.

In order to examine the influence of CO_2 on the readings of mass flow sensors, the molar percentage of CO_2 in the diluted gas needs to be calculated.

The stoichiometric combustion for most fuel used in this work can be expressed as follows:

$$CH_2 + \frac{3}{2}\left(O_2 + \frac{79}{21}N_2\right) \rightarrow CO_2 + H_2O + \left(\frac{3}{2} \times \frac{79}{21}\right)N_2 \quad \text{(A.1)}$$

The molar percentage of CO_2 in raw exhaust is 13.1%. The dilution ratio used for much of filter sampling work was chosen to be 5, which is the mass ratio between the diluent air and raw exhaust. For convenience, the molar percentage ratio between these two gases was assumed to be 5 as well due to the similarity in their densities. Therefore, the molar percentage of CO_2 in the diluted gas with a dilution ratio of 5 was one sixth of that in raw exhaust, in this case, 2.18%. The correction factor for the diluted gas is:

$$[Diluted\ gas] = [CO_2] \times 2.18\% + 1.0 \times (1\text{-}2.18\%) = 1.0076 \approx 1.0 \quad \text{(A.2)}$$

in which [*Diluted gas*] and [CO_2] refer to the correction factors for the diluted gas and CO_2 respectively. Therefore, the diluted gas flow rate can be measured by the Honeywell AWM700 mass flow rate using the same calibration data as N_2 or air.

Publications

1. International Journal of Engine Research – 'Effects of Valve Timings and Coolant Temperature on PM Emissions in a GDI Engine Fuelled with a Gasoline and its E10 Blends (In review)
2. Journal Fuel – 'A Study on PM Emissions and Mixture Preparation of a GDI Engine Fuelled with Different Gasoline/Ethanol Blends' (In preparation)
3. Journal Fuel and Energy – 'Enthalpies of Vaporization of Isooctane and Ethanol Blends and their Effects on PM Emissions from a GDI Engine' (In preparation)
4. SAE technical paper – 'The Influence of Ethanol Blends on Particulate Matter Emissions from Gasoline Direct Injection Engines' (2010)